

**STRUCTURAL BASIS OF INTERACTION BETWEEN FLAGELLAR TYPE III ATPASE
FLII AND FLAGELLAR EXPORT CHAPERONE FLIT**

By

NANDISH KUMAR KHANRA

A dissertation submitted to the

Graduate School-New Brunswick

Rutgers, The State University of New Jersey

In partial fulfillment of the requirements for the degree of

Doctor of Philosophy

Graduate Program in Chemistry

Written under the direction of

Professor Charalampos G. Kalodimos

And approved by

New Brunswick, New Jersey

JANUARY, 2015

ABSTRACT OF THE DISSERTATION

Structural Basis of Interaction Between Flagellar Type III ATPase FliI and Flagellar Export Chaperone FliT

By NANDISH KUMAR KHANRA

Dissertation Director:

Professor Charalampos G. Kalodimos

Bacterial flagella are complex macro-molecular machines consisting of more than thirty different proteins. The bulk of the flagellum functions in the cell exterior. Therefore, the flagellar component proteins have to be exported during its biosynthesis. Bacteria develop flagella specific type III export pathways for the delivery of flagellar proteins outside the cytoplasm. The flagellar proteins are synthesized in the cytosol and are translocated through the central flagellar channel via a dedicated export apparatus to the distal growing end for the construction of the flagellum. The inner-membrane associated ATPase of

flagellar export apparatus, FliI, is considered to be one of the central components in the export process. FliI is a Walker-type ATPase and functions as a hexamer. FliT is the flagellar export chaperone for the flagellar cap-forming protein FliD. It prevents premature aggregation of FliD in the cytosol and facilitates the export of FliD through the export channel. The interaction between FliT and FliI is crucial for the transport of FliD.

We have studied the interaction between FliI and FliT using solution NMR combined with other biophysical techniques. Our biophysical data show that FliT interacts with the extreme N-terminal residues of FliI. FliT inhibits the enzymatic activity of FliI by disrupting FliI dimer. FliT is the only flagellar export chaperone known to inhibit the ATPase activity of FliI.

We have determined the solution structure of FliI-FliT complex that provides the first high-resolution structure of any chaperone-ATPase complex of flagellar type III export pathway or type III secretion system in general. We have found that FliI binds to the hydrophobic cleft of FliT and the extreme N-terminal residues of FliI forms a α -helix upon FliT binding. The solution structure of FliI-FliT complex provides structural insight about possible binding interface of FliT with its substrate, FliD. Our NMR data as well as biochemical and bio-informative studies show that FliT might have common binding motif for its cognate substrate, FliD and the ATPase, FliI.

Acknowledgements

First and foremost, I would like to offer my deepest gratitude to Professor Charalampos G. Kalodimos for his guidance, motivation and support throughout my graduate research at Rutgers University. His dedication and scientific rigor has been a source of inspiration. It was indeed a pleasure having you as my advisor.

I would like to thank my committee members, Professor Jean Baum, Professor David Case and Professor Ranajeet Ghose. I am grateful to all of them for their generous support, suggestion and invaluable time.

I would like to thank to all past and present members of the Kalodimos group. I am thankful to Dr. Paolo Rossi for his helpful support and useful advice. I am thankful to my current and former group members: Dr. Anusarka Bhaumik, Dr. Li Chen, Dr. Tamjeed Saleh, Dr. Woichech Jankowski, Dr. Tomohido Saio, Dr. Xiao Guan, Dr. Chengdong Huang, Dr. Yajun Jiang, Dr. Tao Xie, Antonis Coateas, Huang Min, Dr. Ioannis Gelis, Dr. Shiou-Ru Tzeng, Dr. Ming-Tao Pai, Dr. Xuanjun Ai, Dr. Paramita Sarkar, Dr. Nataliya Popovych, Dr. Dimitra Keramisanou, Dr. Yoan Monneau, Dr. Akash Bhattacharya, Dr. Krishna Mohan Poluri, Dr. Lata Chauhan, Soma Mandal, Ankita Basant, Pragati Sharma and Dr. Aishwarya Ravindran.

I am thankful to Dr. Sophia Kenrick, Wyatt Technology Corporation, for performing light scattering experiments and helpful suggestions. I am grateful to Dr. Nagarajan Murali and Dr. Seho Kim their support with NMR spectroscopy and

helpful suggestions. I am thankful to faculty and staff of Department of Chemistry and Chemical Biology, Center for Integrative Proteomics Research and Biomedical Engineering. Thanks are also due to all my amazing friends whose names have not been listed here. Please know that my appreciation is no less.

I am thankful to all of my friends here at Rutgers, from India and USA.

I feel special gratitude toward my parents and brother Saumya for their unending love, constant support and encouragement.

Dedication

Dedicated to my family

Table of Contents

ABSTRACT OF THE DISSERTATION	ii
Acknowledgements	iv
Dedication.....	vi
List of Tables.....	xi
List of Figures	xii
List of Abbreviations	xxiv
Chapter 1 : Introduction	1
1.1 The Bacterial Flagellar Assembly	1
1.1.1 Architecture of bacterial flagella.....	1
1.1.1.1 Basal body and the flagellar motor.....	1
1.1.1.2 Hook	5
1.1.1.3 Filament	5
1.1.2 Type III protein export for flagellar assembly.....	8
1.1.2.1 Components of flagellar export apparatus.....	11
1.1.2.1.1 Integral membrane components of export apparatus.....	13
1.1.2.1.2 Soluble components of export apparatus.....	16
1.1.2.2 Interaction of flagellar export proteins among themselves and with the C-ring complex.....	18
1.1.2.3 Flagellar export chaperones and their substrates.....	19
1.1.2.4 Interaction of flagellar chaperone-substrate complex with export	

component proteins.....	22
1.1.2.5 The order of flagellar assembly.....	25
1.1.2.6 Energy source for flagellar protein export.....	28
1.1.2.7 Mechanism of flagellar protein export.....	30
1.2 Nuclear Magnetic Resonance Spectroscopy	32
1.2.1 NMR as a tool in structural biology	32
1.2.2 Chemical shift assignment of protein	33
1.2.2.1 Backbone assignment.....	33
1.2.2.2 Side-chain assignment.....	35
1.2.2.3 Nuclear Overhauser Effect Spectroscopy.....	37
1.2.2.4 TALOS.....	37
1.2.3 NMR study of large protein complexes.....	38
1.2.3.1 Protein deuteration.....	40
1.2.3.2 Transverse relaxation optimized spectroscopy.....	40
1.2.3.3 Selective labeling of methyl groups.....	42
1.2.3.4 Structure calculation using sparse NMR data.....	43
1.2.4 NMR study of protein interactions.....	44
1.3 Isothermal Titration Calorimetry (ITC)	45
1.4 Multi-Angle Light Scattering (MALS)	46
1.5 ATPase Assay	48
Chapter 2 : Research Outline.....	49
Chapter 3 : Chemical shift assignment of FliI	50
3.1 Introduction.....	50

3.2 Results.....	54
3.2.1 Biophysical characterization of FliI	54
3.2.2 Chemical shift assignment of FliI	57
3.3 Discussion.....	62
Chapter 4 : Chemical shift assignment of FliT	63
4.1 Introduction.....	63
4.2 Results.....	64
4.2.1 Biophysical characterization of FliT	64
4.2.2 Attempts to assign backbone resonances of FliT	66
4.2.3 Partial side-chain assignment of FliT	73
4.3 Discussion.....	74
Chapter 5 : Interaction study between flagellar ATPase FliI and export chaperone FliT	78
5.1 Introduction.....	78
5.2 Results.....	79
5.2.1 The extreme N-terminal residues of FliI interact with FliT.	79
5.2.2 FliT inhibits ATPase activity of FliI.....	85
5.3 Discussion	87
Chapter 6 : Structural characterization of FliI-FliT complex.....	90
6.1 Introduction.....	90
6.2 Results.....	90
6.2.1 Design and optimization of fusion construct	90
6.2.2 Structure determination of fusion construct	95

6.2.3 Extreme N-terminal residues of Flil form α -helix upon FlIT binding	99
6.3 Discussion	101
Chapter 7 : Materials and Methods	105
7.1 Expression and Preparation of Proteins	105
7.2 Polymerase Chain Reaction (PCR)	108
7.3 MALS Experiments	109
7.4 ITC Experiments	110
7.5 ATPase Assays	111
7.6 NMR Spectroscopy	112
7.7 Structure Calculations	113
References	114

List of Tables

Table 4-1 Summary of ^{15}N -HSQC spectra quality of FliT at different conditions.	68
Table 4-2 Summary of ^{15}N -HSQC spectra quality of different FliT constructs.....	68
Table 4-3 Table for intensity ratio of the major and minor conformations of Ile14, Ile44, Ile60 and Ile93 in the ^{13}C -HMQC of FliT.	73
Table 4-4 Table for intensity ratio of the major and minor conformations of in the ^{15}N -HSQC of FliT. Trp11 and Trp30 represent tryptophan side-chains. A, B and C represents three unassigned cross peaks in ^{15}N -HSQC of FliT that show two populations.	75
Table 6-1 Summary of NMR structural statistics of FliT(1-95)-pcold-FliI(1-25)...	97

List of Figures

- Figure 1-1 Schematic representation of bacterial flagellum (left) and the injectisome (right).2
- Figure 1-2 Electron microscopic images of hook-basal bodies. (a) Mirror average of electron microscopic images of frozen hydrated flagellar hook-basal body complexes of *Salmonella*. The electron microscopic image shows the hook, outermembrane L ring, periplasmic P ring, rod, MS ring, and the rotor/switch (FliG plus the C-ring) in an order from top to bottom. (b) The cytoplasmic view of Quick-freeze, deep-etch replica electron micrograph of basal body. The central protrusion is called the C-ring.3
- Figure 1-3 Stereo views of solid shaded representations of the flagellar filament: A. Axial view of a 50 Å thick cross-section showing 11 subunits in two turns of the one-start helix. B. Side-view of a 300 Å of long segment. Arrow in A and B mark subunit contacts between the outermost part and the vertical column. The scale bar represents 100 Å6
- Figure 1-4 Three-dimensional electron microscopic image of the distal end of the flagellar filament cap. A. Lateral view with the front half removed. B. The lateral view corresponding to the direction 1 in panel c. the top view of the pentameric cap. The subunits of the pentameric cap are labeled with Greek letters'.7
- Figure 1-5 Self-assembly process of the bacterial flagellum. Assembly process starts from the top left and proceeds to the bottom right. After the assembly of the flagellar export apparatus, flagella starts to export the flagellar proteins in the central channel. Flagellar protein that reach the distal end of the growing

structure self-assemble into the template structure formed by distal caps that promote efficient self-assembly of flagellar protein.9

Figure 1-6 Hypothetical model of flagellar type III export apparatus. FlhA, FlhB, FliO, FliP, FliQ and FliR are located within the central pore of MS-ring. FliI and FliJ forms (FliI)₆-FliJ ring complex that is similar to the $\alpha_3\beta_3\gamma$ ring complex of the F₀F₁-ATP synthase. FliH is homologous to the peripheral stalk of F₀F₁-ATP synthase formed by b- and δ -subunit. FliH helps to stably anchor the (FliI)₆-FliJ ring complex to the export gate formed by cytoplasmic domains of FlhA and FlhB. 12

Figure 1-7 Structural topology of FlhA (A) and FlhB (B). Both FlhA and FlhB contain a N-terminal trans-membrane domain, FlhA_{TM} and FlhB_{TM}, and a C-terminal domain (FlhA_C and FlhB_C). FlhA_C consists of four domains, D1, D2, D3 and D4. A flexible linker (FlhA_L) connects FlhA_C with FlhA_{TM}. The highly conserved Asp-208 is shown as closed circle (blue). FlhB_C undergoes autocatalytic cleavage at the site Asn269/Pro270 into FlhA_{CN} and FlhA_{CC}. After the autocatalytic cleavage, FlhA_{CN} and FlhA_{CC} become tightly associated with each other..... 14

Figure 1-8 The cryo-electron microscopic image of FliI (from *C. jejuni*) hexameric ring at the cytoplasmic face of export apparatus. A. The spherical density of the FliI hexameric ring is indicated by red arrow. B. Δ FliI variant shows no spherical density. The diameter of the hexameric ring is ~10nm which matches well with the diameters of hexameric model of FliI (built with F₁-ATPase as template). 16

Figure 1-9 Comparison of crystal structures of different classes of type III specific chaperones. A. Monomer of FliT (pdb ID: 3A7M). B. SycP (class I) in complex with SptP (pdb ID: 1JYO), C. SycD (class II) (pdb ID: 2VGX), D. FlIS (class III) in complex with the C-terminal segment of FlIC (pdb ID: 1ORY), E. CesA (CesAB) (class IV) in complex with EspA (pdb ID: 1XOU), and F. PscE (class V)-PscG in complex with PscF (pdb ID: 2UWJ). All the chaperone molecules are shown in cyan and green; The SycP and SycD form homodimer. PscF forms heterodimer with its co-chaperone PscG. All the homo- or hetero-dimer is shown in cyan and green; the secretion or export substrates are shown in orange.21

Figure 1-10 Order of export pathway in the flagellar morphogenesis in *Salmonella*. The flagellar substructures are colored from dark blue (early) to light blue (late) according to the their stage of export. Integral membrane structures are assembled via sec-mediated export followed by assembly of peripheral structure. The type III export is used for rod, hook and filament assembly.26

Figure 1-11 Mechanism of hook-length control and substrate specificity switching. Diagram shows cartoon structure of FlhB containing N-terminal transmembrane domain (magenta cylinders) and a C-terminal cytoplasmic domain (FlhB_C). FlhB_C undergoes autocatalytic cleavage at the site Asn269/Pro270 into two subdomains, FlhB_{CN} and FlhB_{CC}. FlhB_{CN} and FlhB_{CC} remains tightly associated with each other after cleavage. Initially FlhB_C exists in rod/hook-type specificity mode. Autocleavage of FlhB_C slows down the export rate of rod- and hook-type substrates. Then the interaction of FlhK_C with FlhB_C induces a conformational

change in FlhB _C leading to switching of the export specificity to filament-type mode.....	27
Figure 1-12 Spin system of the peptide backbond and size of the 1J and 2J coupling constants that are used for magnetization transfer in ¹³ C-, ¹⁵ N-labelled proteins.....	33
Figure 1-13 The magnetization transfer pathway in A. CBCANH and B. CBCACONH experiment.	34
Figure 1-14 Assignment strategy for 13C/15N-labeled proteins based on CBCANH and CBCA(CO)NH 3D spectra.....	35
Figure 1-15 The magnetization transfer pathway in HCCH-TOCSY experiment.	36
Figure 1-16 Backbone (dihedral) angles in the protein structure.....	38
Figure 1-17 Effect of molecular weight in the linewidth of the NMR spectra. The linewidth is proportional to T ₂ ($\Delta\nu = 1/\pi T_2$).	39
Figure 1-18 NMR spectroscopy with small and large molecules in solution and the effect of TROSY on large molecules.	41
Figure 1-19 Methyl labeling strategy. (a) Precursors used to produce proteins with methyl labeling (¹³ CH ₃) in isoleucine, leucine and valine (b) Ribbon diagram of the α subunit of <i>T. acidophilum</i> proteasome highlighting the labeling scheme used. Isoleucine (δ^1), leucine and valine methyl groups are indicated in red and deuterons in green ¹⁹¹	42
Figure 3-1 The crystal structure of Flil. A. The crystal structure of Flil(18-456), pdb ID: 2DPY. Color code: the N-terminal β -barrel domain, green; ATPase domain, red; C-terminal domain, blue. B. Structural comparison of Flil(18-456)	

with β subunits of F_1 -ATPase (pale blue). The additional α -helix in β subunits of F_1 -ATPase is shown by blue arrow. C. The crystal structure of F_1 -ATPase (pdb ID: 1BMF).50

Figure 3-2 Hexameric model of Flil built using F_1 -ATPase (1BMF) as template. A. Side view. B. Top view. The alternate subunits in A and B are colored as green and purple. C. The hexameric ring structure of Flil by Cryo-EM. The image represents averaged end-on view of frozen-hydrated ring particles formed by Flil with Mg^{2+} -ADP- AlF_4 . The scale bar indicates 10 nm. D. The active site of Flil modeled using F_1 -ATPase as template. Arg374 of neighboring subunit is shown using dotted circle. E. ATPase activity of Flil was measured with different enzyme concentrations in the presence of 5 mM ATP. Flil shows co-operative effect of ATPase activity with concentration.52

Figure 3-3 Concentration dependent oligomerization of Flil as studied by multi-angle light scattering (MALS). A chromatographic trace of the UV detector (blue) is shown with mass measurements of consecutive fractions of the chromatographic peak (black dots) superimposed. A. SEC-MALS profile for Flil with injected protein concentration=15 mg/ml; MALS data shows heterogeneous populations of Flil ranging from ~90 kDa to ~45 kDa with average molecular weight (Mw) of 63 kDa. B. SEC-MALS profile for Flil with injected concentration=1.5mg/ml. At lower concentration Flil appears to be more homogeneous ranging from ~55 kDa to ~45 kDa. Average molecular weight is 50 kDa, which corresponds to Flil monomer.55

Figure 3-4 Self-association study of FliI and FliT by composition-gradient multi-angle laser light scattering (CG-MALS) using Calypso II composition gradient system (Wyatt Technology Corporation). The solid rectangles represent weight-average molar mass of FliI (blue) and FliT (red), respectively, at different concentrations of FliI and FliT. The dotted line represents fit to the CALYPSO software (Wyatt). The dissociation constant of dimer-monomer equilibrium of FliI and FliT are $\sim 17 \mu\text{M}$ and $\sim 300\text{-}600 \mu\text{M}$56

Figure 3-5 A. ^{15}N -TROSY B. ^{13}C -HMQC of U- $[\text{}^2\text{H}, \text{}^{12}\text{C}, \text{}^{15}\text{N}]$ Met(ϵ)-, Val($\gamma 1, \gamma 2$)-, Leu($\delta 1, \delta 2$)-, Ile($\delta 1$)- $[\text{}^{13}\text{CH}_3]$ FliI.....57

Figure 3-6 A. ^{15}N -TROSY of U- $[\text{}^2\text{H}, \text{}^{15}\text{N}]$ FliI(18-456). B ^{15}N -TROSY of U- $[\text{}^2\text{H}, \text{}^{15}\text{N}]$ FliI(104-456) C. ^{15}N -HSQC of U- $[\text{}^{15}\text{N}, \text{}^{13}\text{C}]$ FliI(18-100).58

Figure 3-7 A. ^{15}N -TROSY B. ^{13}C -HMQC of U- $[\text{}^2\text{H}, \text{}^{12}\text{C}, \text{}^{15}\text{N}]$, Ala-, Met-, Val($\gamma 1, \gamma 2$)-, Leu($\delta 1, \delta 2$)-, Ile($\delta 1$)- $[\text{}^{13}\text{CH}_3]$ FliI(105-456) showing backbone and side-chain resonance assignment.59

Figure 3-8 A. ^{15}N -HSQC of FliI(18-100) with backbone resonance assignment. B. ^{13}C -HSQC of FliI(18-100) with side-chain assignment.61

Figure 3-9 Overlay of expanded region of ^{15}N HSQC of FliI with A. FliI(18-100) and B. FliI(104-456).61

Figure 4-1 The crystal structure of FliT. A. Crystal structure of FliT dimer. The molecule A and molecule B of FliT are shown in magenta and cyan respectively. B and C show the molecule A and molecule B of FliT separately. The $\alpha 1$ -, $\alpha 2$ -, $\alpha 3$ - and $\alpha 4$ -helix are labeled in B and C. The flexible $\alpha 4$ -helix in B and is indicated in blue arrow. D. The hydrophobic cleft of FliT.....63

Figure 4-2 Native mass determination of FliT using MALS. A chromatographic trace of the UN detector (grey) is shown with mass measurements of consecutive fractions of the chromatographic peak (blue dots) superimposed. Injected protein concentration of FliT = 10.96 mg/ml; average molecular weight of FliT ~19 kDa.

.....65

Figure 4-3 The hydrodynamic radius of FliT at different molar mass. The solid rectangle shows the hydrodynamic radius of FliT. The dotted red line indicates the predicted hydrodynamic radius of a globular protein with same molar mass as FliT.....65

Figure 4-4 A. ^{15}N -HSQC of $\text{U-}^{15}\text{N}$ FliT B. ^{15}N -HSQC of $\text{U-}[^1\text{H}, ^{15}\text{N}]$ FliT C. ^{15}N -HSQC of $\text{U-}^{15}\text{N}$ FliT(1-97). D. Superposition of ^{15}N -HSQC of $\text{U-}^{15}\text{N}$ FliT (red) with $\text{U-}[^2\text{H}, ^{15}\text{N}]$ FliT (blue).....67

Figure 4-5 Assignment strategy of the resonance assignment of methyl groups of FliT. A. Superimposition of ^{13}C -HMQC of WT FliT (cyan) and FliTM112I (red). C. Crystal structure of FliT (PDB ID: 3A7M) showing close proximity of Ile8, Ile60 and Met63. D. ^{13}C -HMQC-NOESY-HMQC strips of FliTG94PS96P for Met63, Ile8 and Ile60.69

Figure 4-6 ^{13}C -HMQC of FliT showing partial side-chain assignment. The minor conformations are shown in red.70

Figure 4-7 Dilution effects in the ^{15}N -TROSY and ^{13}C -HMQC of FliT. A. Superposition of ^{13}C -HMQC of FliT at 1 mM, 0.6 mM and 0.2 mM. Color code: 1 mM (green), 0.6 mM (magenta) and 0.2 mM (orange). B. Superposition of ^{15}N -

TROSY of FliT at different concentrations, 0.75 mM, 0.6 mM and 0.2 mM. Color code: 0.75 mM (magenta), 0.6 mM (red) and 0.2 mM (cyan).....72

Figure 4-8 Native mass determination of GB1FliT using MALS. A chromatographic trace of the UN detector (grey) is shown with mass measurement of consecutive fractions of the chromatographic peak superimposed. Blue and green illustrates molar mass of two closely populated peaks of GB1FliT.....76

Figure 5-1 Interaction between FliI and FliT using pull down assay. A. Interaction between FliI and FliT. B. Interaction between FliI and FliT94.....78

Figure 5-2 Interaction between FliI and FliT. A. ^{15}N -HSQC titration of U- $[\text{}^2\text{H}, \text{}^{12}\text{C}, \text{}^{15}\text{N}]$ Ala(β)-, Met(ϵ)-, Val(γ 1, γ 2)-, Leu(δ 1, δ 2)-, Ile(δ 1)- $[\text{}^{13}\text{CH}_3]$ FliI with natural abundance FliT. Color code: ^{15}N -TROSY of FliI, green; ^{15}N -TROSY of FliI+FliT=1:5, magenta; B. ^{15}N -HSQC titration between U- $[\text{}^2\text{H}, \text{}^{12}\text{C}, \text{}^{15}\text{N}]$ Ala(β)-, Met(ϵ)-, Val(γ 1, γ 2)-, Leu(δ 1, δ 2)-, Ile(δ 1)- $[\text{}^{13}\text{CH}_3]$ FliT and natural abundance FliI. Color code: ^{15}N -TROSY of FliI, blue; ^{15}N -TROSY of FliI+FliT=1:1, red; C. Overlay of first scan for the ^{15}N -HSQC titration of U- $[\text{}^2\text{H}, \text{}^{12}\text{C}, \text{}^{15}\text{N}]$ Ala(β)-, Met(ϵ)-, Val(γ 1, γ 2)-, Leu(δ 1, δ 2)-, Ile(δ 1)- $[\text{}^{13}\text{CH}_3]$ FliI with natural abundance FliT.80

Figure 5-3 Interaction of N-terminal truncation construct of FliI with FliT. A. Overlay of ^{15}N -TROSY of U- ^{15}N FliI(Δ 104) with FliI(Δ 104) + FliT=1:1. Color code: ^{15}N -TROSY of U- ^{15}N FliI(Δ 104) in blue, ^{15}N -TROSY of U- ^{15}N FliI(Δ 104)+FliT=1:1 in red. B. Overlay of ^{15}N -TROSY of U- ^{15}N FliI(Δ 18) with FliI(Δ 18) + FliT=1:1. Color code: ^{15}N -TROSY of U- ^{15}N FliI(Δ 18) in blue, ^{15}N -TROSY of U- ^{15}N FliI(Δ 18)+FliT=1:1 in red.....81

Figure 5-4 Overlay of ^{15}N -HSQC spectra of FliI (green) with FliI+FliT=1:5 (magenta). The cross-peaks of extreme N-terminal residue of FliI, which undergo line broadening upon FliT binding, are indicated by (x).....82

Figure 5-5 ^{15}N -HSQC titration of U- ^{15}N GB1FliI(1-33) with natural abundance FliT. A. Overlay of ^{15}N -HSQC of GB1FliI(1-33) with GB1. Color code: GB1FliI(1-33), blue ;GB1, red; B. ^{15}N -HSQC titration of U- ^{15}N GB1FliI(1-33) with natural abundance FliT. Color code: GB1FliI(1-33), blue ; GB1FliI(1-33) with FliT at molar ratio of 1:1, green ; GB1FliI(1-33) with FliT at molar ratio of 1:5, magenta.83

Figure 5-6 Interaction study between FliI and FliT using composition gradient multi-angle light scattering (CG-MALS). The left and the right diagrams show the total light scattering signal and the mole-fraction of each species for the FliI-FliT mixture at different concentrations. Majority of the interaction has 1:1 stoichiometry of FliI and FliT with $K_D \sim 1\text{-}3 \mu\text{M}$. Small amount of different higher order oligomer ($\sim 1\%$ mol/mol) are also present. The higher order oligomers are shown in the diagram as $(\text{FliI})_2(\text{FliT})_2$, but it may be combination of $(\text{FliI})(\text{FliT})_2$, $(\text{FliI})_2(\text{FliT})$ and $(\text{FliI})_2(\text{FliT})_2$84

Figure 5-7 A. Inhibition of ATPase activity of FliI by FliT. Measurement was carried out on FliI or mixture of FliI and FliT at molar ratios of 1:10, 1:20, and 1:50.86

Figure 5-8 Schematic model for interaction between FliI and FliT. Model for A. Monomer-dimer equilibrium of FliI. B. Monomer-dimer equilibrium of FliT. C. interaction between FliI and FliT. Color code: FliT dimer or monomer are shown

in cyan; The extreme N-terminal of Flil is shown in black line, N-terminal β -barrel domain of Flil in red and the ATPase domain Flil in blue.88

Figure 6-1 ^{15}N -HSQC of different fusion constructs of Flil and FliT. A. ^{15}N -HSQC of U- ^{15}N Flil(1-30)-(GS)₃-FliT. B. ^{15}N -HSQC of U- ^{15}N GB1-Flil(1-30)-(GS)₃-FliT (blue) overlaid with GB1 (magenta). C. ^{15}N -HSQC of U- ^{15}N Flil(1-25)-(GS)₃-FliT(1-95). D. Overlay of ^{15}N -HSQC of Flil(1-25)-(GS)₃-FliT(1-95) (green) with Flil(1-25)-(GS)₃-FliT (red).91

Figure 6-2 Native mass determination of FliT(1-95)-(pcold)-Flil(1-25). A chromatographic trace of the UN detector (grey) is shown with mass measurements of consecutive fractions of the chromatographic peak (blue dots) superimposed.92

Figure 6-3 ^{15}N -TROSY B. ^{13}C -HMQC of U- ^2H , ^{12}C , ^{15}N], Ala(β)-, Met(ϵ)-, Val(γ 1, γ 2)-, Leu(δ 1, δ 2)-, Ile(δ 1)-, Thr(γ 2)- ^{13}C], Phe-, Tyr- ^1H , ^{13}C], Trp- ^1H] FliT(1-95)-pcold-Flil(1-25) showing backbone and side-chain resonance assignment.93

Figure 6-4 NOE between FliT(1-95) and Flil(1-25) in FliT(1-95)-pcold-Flil(1-25) showing Flil(1-25) binds to FliT(1-95) in FliT(1-95)-pcold-Flil(1-25). NOESY strip of ^{13}C NOESY HMQC of A. aromatic and B. and C. aliphatic side-chains. FliT(1-95)-pcold-Flil(1-25) showing NOE between Phe15 of Flil(1-25) and Ile14 and Ile44 of FliT(1-95).94

Figure 6-5 Solution structure of FliT(1-95)-pcold-Flil(1-25). A. Side-on view of FliT(1-95)-pcold-Flil(1-25). The α 1, α 2 and α 3 helices of FliT(1-95) are shown in blue. The α 1' helix of Flil1-25) is shown in red. The linker region is colored in

yellow. B. The end-on view of fusion structure. C. The topology of four helical bundle of FliT(1-95)-pcold-FliI(1-25). The α_1 , α_2 and α_3 helices of FliT(1-95) are shown in blue, green and cyan, respectively. The $\alpha_{1'}$ helix of FliI(1-25) is shown in red. The linker connecting α -helices of FliT(1-95) are shown in black. The linker connecting FliT(1-95) and FliI(1-25) are shown in orange. D. Ligplot image of interface of FliT(1-95) and FliI(1-25) in FliT(1-95)-pcold-FliI(1-25)95

Figure 6-6 Solution NMR structure of fusion construct. Bundle backbone RMSD 0.5Å from Table 6-1.96

Figure 6-7 Structural comparison of fusion structure with crystal structure of FliT.

A. Structural comparison of fusion structure with crystal structure of FliT from *S. enterica* (pdb code 3A7M). The α_1 , α_2 and α_3 of FliT(1-95) in the fusion structure is shown in blue. The α -helix corresponding to FliI(1-25) in red. Each monomer of FliT dimer is shown in magenta and cyan. FliT(1-95) is structurally aligned with the core structure of molecule A, composed of α_1 , α_2 and α_3 helix. The α -helix of FliI(1-25), $\alpha_{1'}$ is aligned with α_4 of molecule. B. Structural model for FliI-FliT complex structure. Color code: FliT in red; FliI in green; The extreme N-terminal α -helix of FliI is shown by blue arrow; All the structural alignments are performed in pymol.98

Figure 6-8 ^{15}N -HSQC titration of U- $[\text{}^2\text{H}, \text{}^{15}\text{N}]$ FliT with natural abundance FliI mutants. ^{15}N -HSQC of FliT is shown in blue in all superposition spectra. A. The position of Trp8 and Phe15 sidechain in FliT(1-95)-pcold-FliI(1-25) are shown in green stick. The $\alpha_{1'}$ helix of FliI(1-25) are shown in transparent red cartoon. The FliT(1-95) is shown blue surface. B. The ^{15}N -HSQC of titration FliT with natural

abundance FliI. FliT spectrum with FliI is shown in red. C. The ^{15}N -HSQC of titration FliT with natural abundance FliIW8AF15A. A FliT spectrum with FliI is shown in green. D. The ^{15}N -HSQC of titration FliT with natural abundance FliIW8E. A fliT spectrum with FliI is shown in magenta. In all titrations, FliI or FliI mutants are added in 1:1 ratio. 100

Figure 6-9 A. Sequence alignment extreme N-terminal residues of FliI from *S. enterica*, FliI from *H. pylori*, InvC from *S. enterica*, EscN from *EPEC*, F_1 -ATPase α -subunit from bovine mitochondria and F_1 -ATPase α -subunit from *B. subtilis*. B. Helical wheel plot of extreme N-terminal residues of FliI from *S. enterica*, *H. pylori*, EscN from *EPEC* and InvC from *S. enterica*. Esprint was used to make sequence alignment diagram. 102

Figure 6-10 A. Sequence alignment of FliT-binding domain of FliI, FliD, FliJ and FliT(95-111). B. Helical wheel plot of FliI(5-22), FliD(432-449), FliJ(66-83) and FliT(95-111). Esprint was used to make sequence alignment diagram. 103

List of Abbreviations

ADP: Adenosine Diphosphate

AMP-PNP: Adenosine 5'-(β,γ -imido)triphosphate

ATP: Adenosine Triphosphate

CCCP: Carbonyl Cyanide m-Chlorophenylhydrazone

Cryo-EM: cryo-Electron Microscopy

CG-MALS: Composition-Gradient Multi-Angle Light Scattering

CSA: Chemical Shift Anisotropy

CSP: Chemical Shift Perturbation

DD: Dipole-Dipole

E. coli: Escherichia Coli

$\Delta G:$ Change in Gibb's Free Energy

GB1: B1 domain protein G (Immunoglobulin-binding protein)

GST: Glutathione S-transferases

$\Delta H:$ Change in Enthalpy

HSQC: Heteronuclear Single Quantum Coherence

HMQC: Heteronuclear Multiple Quantum Coherence

IPTG: Isopropyl β -D-1-thiogalactopyranoside

ITC: Isothermal Titration Calorimetry

K_A: Association constant

K_D: Dissociation constant

LB: Luria Broth

LZ: Leucine Zipper

MALS: Multi-angle Light Scattering

MBP: Maltose-binding protein

M9: Minimal Media

NMR: Nuclear Magnetic Resonance

NOESY: Nuclear Overhauser Effect Spectroscopy

NS: Number of Scans

OD: Optical Density

PCR: Polymerase Chain Reaction

PDB: Protein Data Bank

P_i: Inorganic Phosphate

PMF: Proton-motive Force

ΔS: Change in Entropy

SDS-PAGE: Sodium Dodecyl Sulphate Polyacrylamide Gel Electrophoresis

T: Absolute Temperature

T₂: Transverse Relaxation

T3SS: Type III Secretion System

TROSY: Transverse Relaxation Optimized Spectroscopy

WT: Wild Type

Chapter 1 : Introduction

1.1 The Bacterial Flagellar Assembly

Bacteria motility is controlled by clock-wise and anti-clockwise rotation of the bacterial flagellum. The flagellum is an extremely sophisticated and complex nano-machinery composed of more than thirty different proteins^{1,2}. Extending from cytoplasm to cell exterior, bacterial flagellum consists of both motor apparatus and protein export apparatus. All the proteins needed to construct the flagellum in the cell exterior are exported from the cytoplasm in a timely and well-regulated manner. While Sec-dependent pathway contributes to the export of initial membrane components of the export apparatus, all the other subunits are exported by flagellar specific type III secretion (TTS) export pathway³.

1.1.1 Architecture of bacterial flagella

Extensive studies have been conducted using cryo-electron microscopy (cryo-EM), X-ray crystallography, solid-state NMR in conjunction with molecular modeling to understand the morphology of bacterial flagella. The architecture of bacterial flagellum can be divided into several parts from base to tip^{1,4} as shown in Figure 1-1.

1.1.1.1 Basal body and the flagellar motor

The basal body of the individual flagellum consists of the MS ring, the C-ring, a periplasmic P ring, an outer membrane L ring and a rod that traverses to the periplasmic space (Figure 1-2). The MS ring is composed of FliF (Figure 1-1)^{5,6}. The 3D cryo-EM image of the isolated MS-ring, obtained from over-expressed

FliF, shows complex architecture made up of five domains and has a 26-fold rotational symmetry⁵. The diameter of the S-ring is 24 nm in both the FliF ring and the basal body. The diameter of the M-ring is 24 nm

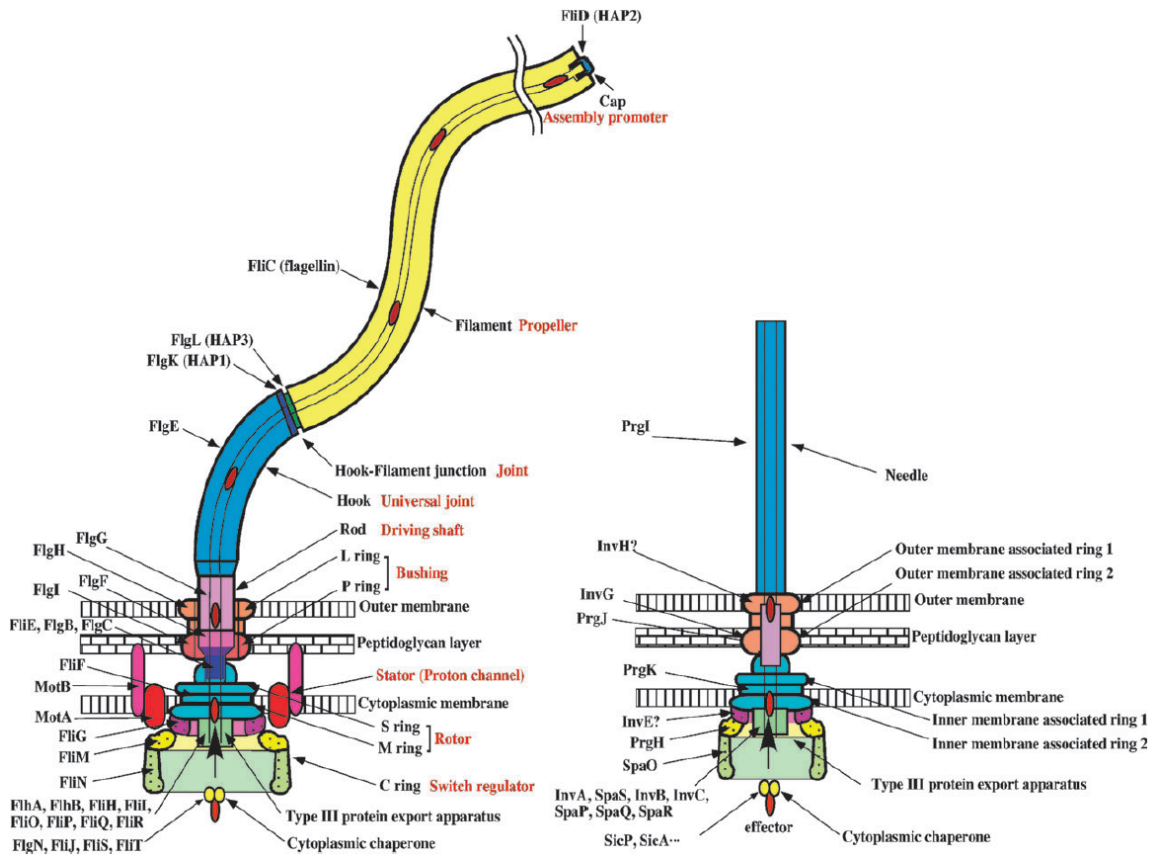


Figure 1-1 Schematic representation of bacterial flagellum (left) and the injectisome (right)²⁰.

in the FliF ring as opposed to 30 nm in the basal body^{5,7}. The larger diameter of the M-ring in the basal body has been attributed to the association of the FliG with FliF. The C-ring is composed of three flagellar proteins, FliG, FliM and FliN (Figure 1-1)^{8,9}. The FliG is located on the upper part of the C-ring and the C-ring

is mounted into the MS ring via direct interaction between FliF and FliG^{10,8}. The C-terminus of FliF interacts with N-terminus of FliG in a 1:1 stoichiometry¹¹. One

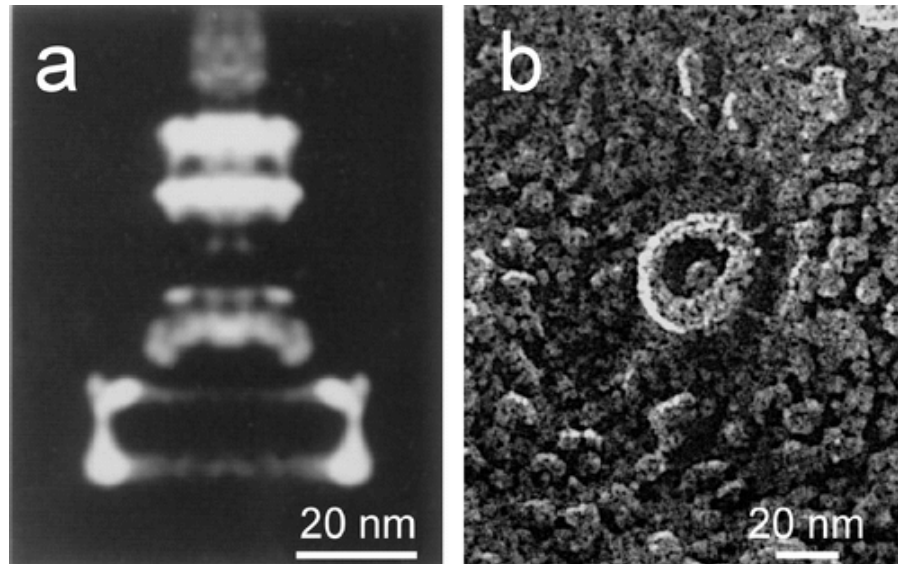


Figure 1-2 Electron microscopic images of hook-basal bodies. (a) Mirror average of electron microscopic images of frozen hydrated flagellar hook-basal body complexes of *Salmonella*. The electron microscopic image shows the hook, outer membrane L ring, periplasmic P ring, rod, MS ring, and the rotor/switch (FliG plus the C-ring) in an order from top to bottom. (b) The cytoplasmic view of Quick-freeze, deep-etch replica electron micrograph of basal body. The central protrusion is called the C-ring¹.

subunit of FliM interacts with four subunits of FliN to form a stable cup-like FliM-FliN complex^{12,13,14}. FliM is located between the C-terminal domain of FliG and the FliN tetramer connecting both FliG and FliN¹⁵. The rotational symmetry of the C-ring varies from 32-fold to 36-fold as evidenced from EM studies¹⁶. The height

of the C-ring is 16.5 nm and the ring diameter varies between 45-49 nm¹⁶. The P- and L-ring are situated in the periplasmic peptidoglycan layer and the outer membrane, respectively⁴. The P-ring is made up of multiple copies of the periplasmic protein, FlgI, whereas L-ring is composed of FlgH^{17,18,19}. The rod structure of basal body can be divided into three sub-structures (Figure 1-1), i. MS ring/rod junction, ii. proximal rod and iii. distal rod²⁰. The putative MS ring/rod junction is made of FliE²¹ and the proximal and distal rods are made of FlgB, FlgC, FlgF and FlgG respectively^{20,22,23}.

The flagellar motor can be divided into two major parts: stator and rotor. The stator is composed of two trans-membrane proteins, MotA and MotB. On the other hand, the multiple copies of FliG in the upper part of the C-ring constitute the rotor structure. The stator and rotor are attached non-covalently to the peptidoglycan layer of the cell membrane and also to the MS-ring, respectively. The FliG along with the MotA and MotB are responsible for generation of necessary torque for flagellar rotation²⁴. MotA has a large cytoplasmic domain that interacts with the rotor protein FliG, via conserved charged residues^{25,26} and MotB has large periplasmic domains that are attached to the peptidoglycan layer²⁷. Four MotA subunits interact with two MotB subunits to form a MotA₄MotB₂ complex²⁸. The MotA₄MotB₂ complex constructs two channel ion-conducting complex which constitutes a two channel ion-conducting complex that couples the proton flow across the cell membrane to the generation of torque necessary for flagellar rotation²⁹. A conserved aspartic acid residue (Asp32) in the trans-membrane segment of MotB is essential for torque generation³⁰. The

acidic Asp32 residue acts as a proton-binding site. The proton binding and dissociation at Asp32 induce conformational changes in the cytoplasmic domain of MotA, which drive flagellar rotation through the interaction between cytoplasmic domains of MotA with FliG³¹.

1.1.1.2 Hook

The flagellar hook is a short, highly curved tubular structure that connects the flagellar motor to filament (Figure 1-1). It is made up of 120 copies of the flagellar hook proteins, FlgE^{32,33}. It functions as universal joint and transmits the torque of the flagellar motor to the flagellar filament necessary for swimming and tumbling of flagella^{34,35}. Since an appropriate length and bending flexibility of the hook is important for its function, the hook length is regulated during hook formation³⁶. A partial atomic model of the flagellar hook was obtained by combination of X-ray crystallography and cryo-EM³⁷.

Between the hook and filament there are two short junction proteins, FlgK, the hook-associated proteins 1 (HAP1) and FlgL, the hook-associated proteins 3 (HAP3)^{38,39}. The hook-associated proteins act as structural adaptor between the hook and the filament, which possess distinct mechanical properties. The hook, being the universal joint, is more flexible whereas the filament, which acts as propeller, is relatively more rigid.

1.1.1.3 Filament

The bacterial filament is a long, hollow cylindrical structure that functions as propeller during flagellar movement⁴⁰. It is a helical assembly of a single protein,

flagellin, consisting of eleven protofilaments. The protofilaments are longitudinal helical arrays of subunits (Figure 1-3). Depending on supercoiling, several kinds of helical forms of filaments are possible. For example, left- and right-handed

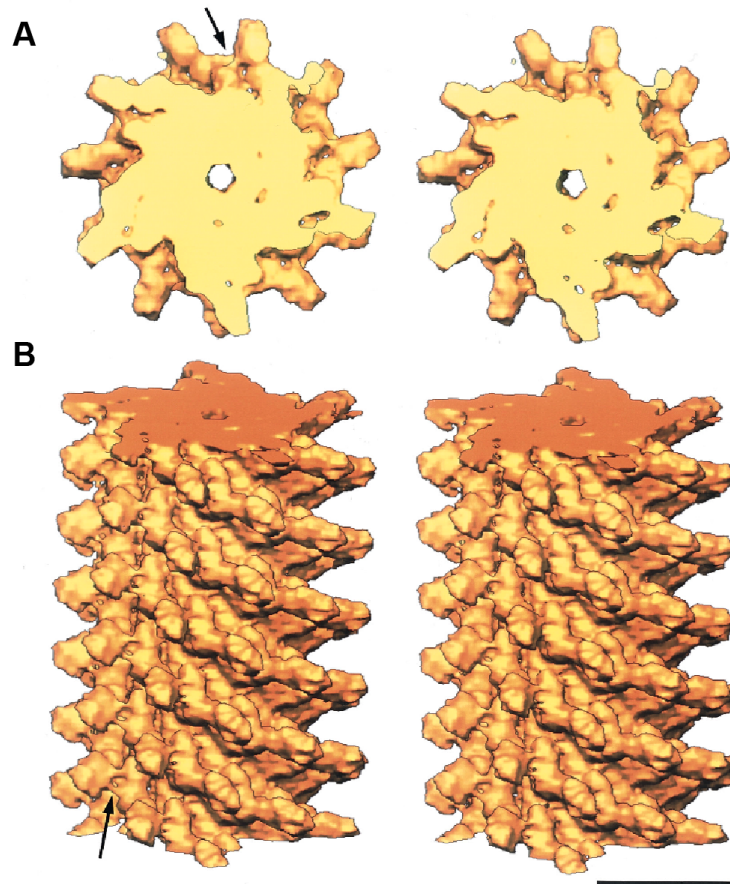


Figure 1-3 Stereo views of solid shaded representations of the flagellar filament: A. Axial view of a 50 Å thick cross-section showing 11 subunits in two turns of the one-start helix. B. Side-view of a 300 Å of long segment. Arrow in A and B mark subunit contacts between the outermost part and the vertical column. The scale bar represents 100 Å ⁴¹.

helical forms are constructed by a mixture of L- and R-type of protofilament conformations^{42, 43}. However, in case of straight filaments, all the eleven protofilaments are of the same type. Two distinct types of helical symmetries are present in straight filaments. Depending on the left- or right-handedness of the longitudinal 11-start helix, L- or R-type straight filaments are formed, respectively. A complete atomic model of R-type filament was constructed by using a combination of cryo-EM and X-ray crystallography^{44,45}.

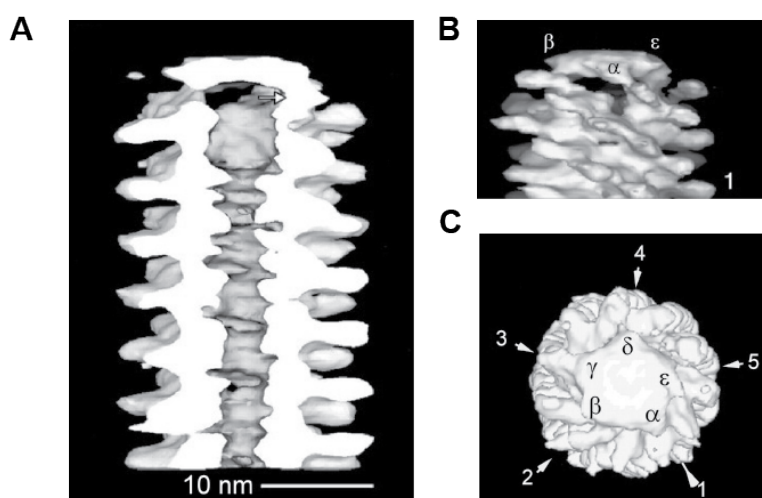


Figure 1-4 Three-dimensional electron microscopic image of the distal end of the flagellar filament cap. A. Lateral view with the front half removed. B. The lateral view corresponding to the direction 1 in panel c. the top view of the pentameric cap. The subunits of the pentameric cap are labeled with Greek letters^{1,51}.

The swimming pattern of bacteria consists of 'run' and 'tumble'. During 'run', the flagellar motor rotates anti-clockwise and the flagellar filaments with left-handed

helical symmetry, form bundle and propel the bacterium. During 'tumble', the motor suddenly rotates clockwise. The resultant twisting force turns the left-handed helical form of filaments into right-handed one, causing the bacterium to tumble^{46,47,48}. Thus the structural arrangements and the dynamic properties of the flagellar filaments are essential for its function. At the growing tip of the filament, there is a filament cap made of the hook-associated protein 2 (HAP2), FliD^{49,50}. FliD forms the annular pentameric structure at the top of growing flagellin with the flat-top domain and flexible leg domains (Figure 1-4). The outer and inner diameters of the pentameric ring structure are 10 nm and 3 nm respectively⁵¹. The pentameric cap of FliD promotes the flagellin polymerization during filament synthesis⁵¹. The *fliD*-deficient mutant of *Salmonella* lacks flagellar filament and secretes FliC into the medium⁴⁹.

1.1.2 Type III protein export for flagellar assembly

The most of the flagellar structure lies outside of the cytoplasm. Therefore all the protein subunits needed to build flagellum have to be secreted. The order of addition of flagellar substructure proceeds from most proximal to most distal structure (Figure 1-5). The integral and peripheral membrane components are exported and assembled first, followed by export and assembly of periplasmic and outer membrane components. The components that lie outside the cell are exported last. Bacteria utilize Sec-pathway⁵² for the export of integral membrane components and the components of the P- and L-ring. The majority of the proteins needed to build bacterial flagellum are exported via type III flagellar export pathway.

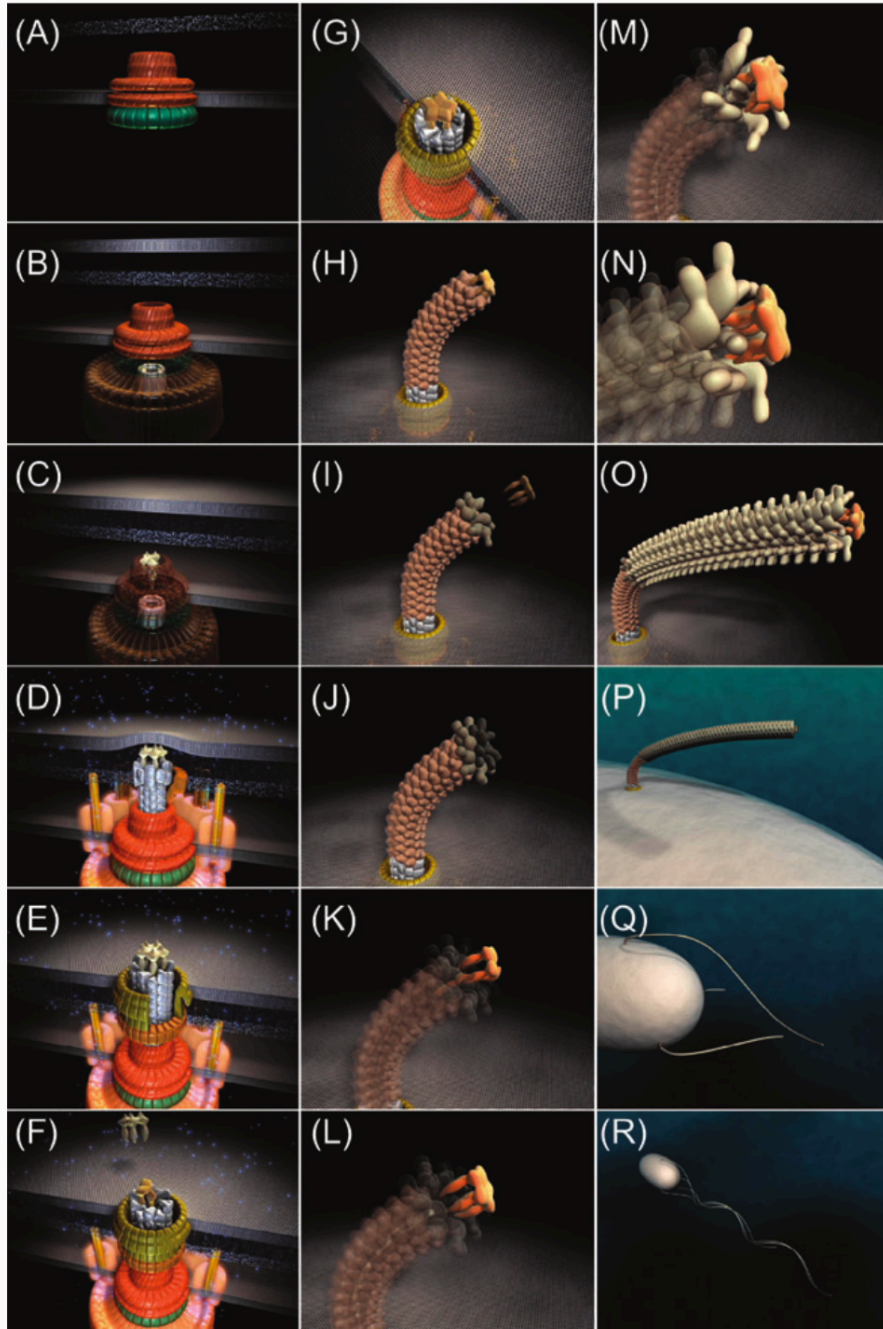


Figure 1-5 Self-assembly process of the bacterial flagellum. Assembly process starts from the top left and proceeds to the bottom right. After the assembly of the flagellar export apparatus, flagella starts to export the flagellar proteins in the central channel. Flagellar protein that reach the distal end of the growing

structure self-assemble into the template structure formed by distal caps that promote efficient self-assembly of flagellar protein²⁰.

The Sec-secretion system provides a major pathway of translocation of proteins from the cytosol across the plasma membrane in bacteria^{52,53}. The earliest event in the flagellar protein secretion is the export of integral membrane proteins^{1,54}. The protein component for the MS-ring, FliF, is exported first and assembled to form the MS-ring. Then all the intergral membrane components of the flagellar export apparatus, FlhA, FlhB, FliO, FliP, FliQ and FliR, are exported to form the export gate. The FliG and the C-ring are then assembled onto the MS-ring. The FliG is assembled first to MS-ring followed by assembly of FliM and FliN to form the C-ring¹. Then Mot proteins are secreted via Sec-pathway and assembled to form the stator complex¹. Other than integral membrane components, FlgI and FlgH, the components of P- and L-ring are also secreted via Sec-pathway.

The protein subunits needed to make flagellar substructures other than integral membrane proteins are secreted by flagellar type III export pathway^{1,4,60}. Several gram-negative bacteria utilize specialized secretion system called type III secretion system (T3SS) to deliver bacterial effector proteins into the host cells^{55,56}. Bacteria utilize similar secretion pathways to export subunits needed to build the flagellum. There are several distinct features of T3SS of pathogenic gram-negative bacteria or flagellar type III export pathway^{1,56}: A) The secreted proteins lack a cleavable signal peptide that is essential for sec-mediated

secretion pathways. B) The secreted proteins require specialized small, acidic proteins, called chaperones, for their secretion. C) There is well-defined structure of secretion apparatus, which constitutes significant part of the flagellum and plays crucial role in export as well as motility¹. In case of flagellar export, most of the exported proteins are incorporated into flagellar structure, while in case of T3SS of pathogenic bacteria, early substrates are assembled into the needle complex and the rest of the substrates are either secreted into the host cells or in the extracellular milieu or into some host cell compartments (Figure 1-1). D) There is a continuous central channel in the nascent structure and all the subunits are added distally by single subunit diffusion through the central channel (Figure 1-5). There are total fourteen substrates that are transported through the export apparatus via flagellar type III export pathway⁵⁷. Depending on the mode of their export, the flagellar export substrates can be classified into two groups: i, rod-hook type substrates or early export substrates and ii, filament type substrates or late export substrates⁵⁷. The rod-hook type substrates include FliE (basal body protein); FlgB, FlgC and FlgF (proximal basal body rod proteins); FlgG (distal rod protein); FlgE (hook protein); FlgD (hook capping or scaffolding protein); FlgJ (rod cap); FliK (protein involved in hook-length control); FlgM (anti- σ factor). The rod-hook type early export substrates are exported first. When hook reaches certain length, FliK sends signal to FlhB, which then switches the substrate specificity from early export substrates to late export substrates^{58,59,60}.

1.1.2.1 Components of flagellar export apparatus

The flagellar type III export apparatus consists of both integral membrane components and soluble components (Figure 1-6). Integral membrane components are composed of six integral membrane proteins, FlhA, FlhB, FliO, FliP, FliQ and FliR^{61,62,63}. The soluble components of export apparatus constitute of FliI, FliH, FliJ, FliT, FlgN and FliS^{61,62,63}. Among the soluble components, FliT, FlgN and FliS are specific chaperones for filament type substrates. FliI, FliH and FliJ act as general export components, which are required for export of all substrates. All the components of the export apparatus are highly conserved among homologous species.

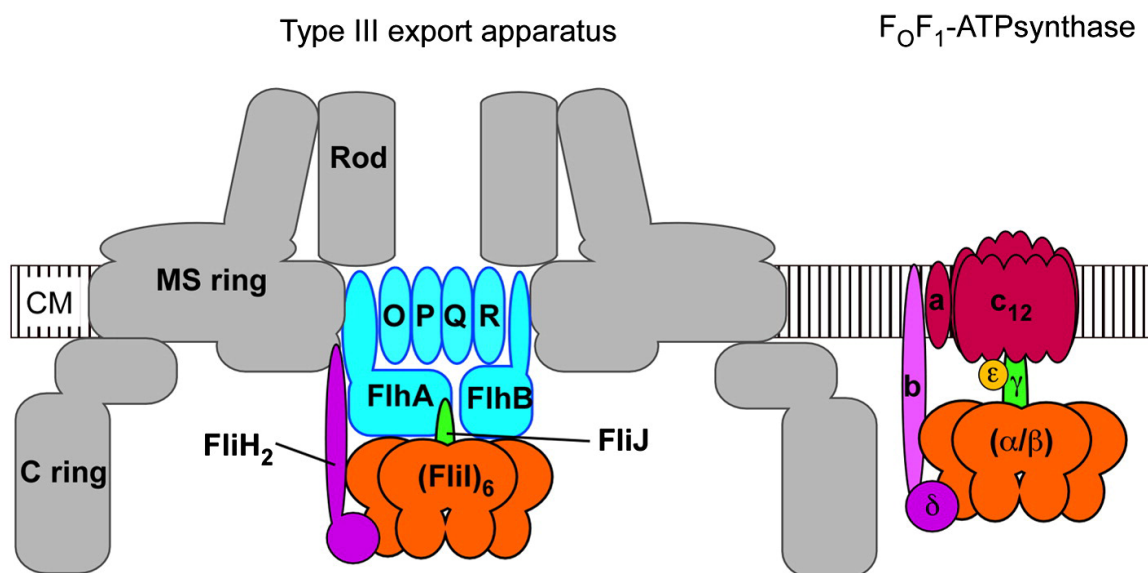


Figure 1-6 Hypothetical model of flagellar type III export apparatus. FlhA, FlhB, FliO, FliP, FliQ and FliR are located within the central pore of MS-ring. FliI and FliJ forms (FliI)₆-FliJ ring complex that is similar to the α₃β₃γ ring complex of the F₀F₁-ATP synthase. FliH is homologous to the peripheral stalk of F₀F₁-

ATP synthase formed by β - and δ -subunit. FliH helps to stably anchor the (FliI)₆-FliJ ring complex to the export gate formed by cytoplasmic domains of FlhA and FlhB⁴.

1.1.2.1.1 Integral membrane components of export apparatus

Each of the integral membrane components of export apparatus is an integral membrane protein with varying degree of trans-membrane domains. FlhA, FlhB, FliO, FliP, FliQ and FliR consist of eight, four, one, four, two and six trans-membrane helices, respectively^{4,64,65}. All the integral membrane components of the export apparatus are located within the cytoplasmic face of the MS-C ring complex (Figure 1-6)^{66,67}. The N-terminal trans-membrane regions of FlhA was reported to interact with FliF, FliR and FlhB^{68,69,70,63}. Affinity blotting studies indicate FlhA also interacts with FliO, FliP and FliQ⁷¹. In addition, a *fliR-flhB* fusion gene can complement *fliR-flhB* null strains suggesting close proximity of FlhB and FliR in the cytoplasmic membrane⁷². FliO maintains the stability of FliP through trans-membrane domain interaction⁷³. Thus the integral membrane components, FlhA, FlhB, FliO, FliP, FliQ and FliR interact with each other to form multi-subunit complex which forms the export gate for the flagellar type III export apparatus (Figure 1-6). The probable stoichiometry of the export gate complex has been suggested to be (FlhA)₂(FlhB)₂(FliO)(FliP)₄(FliQ)(FliR) with a total mass of ~380kDa¹.

Among the integral membrane components, FlhA, FlhB and FliO have C-terminal cytoplasmic domains^{4,65} which play critical roles in substrate recognition and the coordinated delivery of flagellar export substrate. The crystal structures of the cytoplasmic domain of both FlhA and FlhB, designated as FlhA_C and FlhB_C respectively, were reported^{74,75,76}. For FlhA_C, crystal structure was reported from both *Salmonella enterica* and *Bacillus subtilis*^{74,75}. The crystal structure of FlhA_C from *Salmonella enterica* consists of four sub-domains, D1, D2, D3 and D4,⁷⁴ whereas the crystal structure of FlhA_C from *Bacillus subtilis* is constituted of three sub-domains, D1, D2 and D3⁷⁵ (Figure 1-7). However, for *Bacillus subtilis*, the D1 domain can be divided into two parts, a well-folded D1a part and a disordered D1b part⁷⁵. In all crystal structures, there is a N-terminal flexible region of FlhA_C, which connects FlhA_C to the N-terminal transmembrane domain.

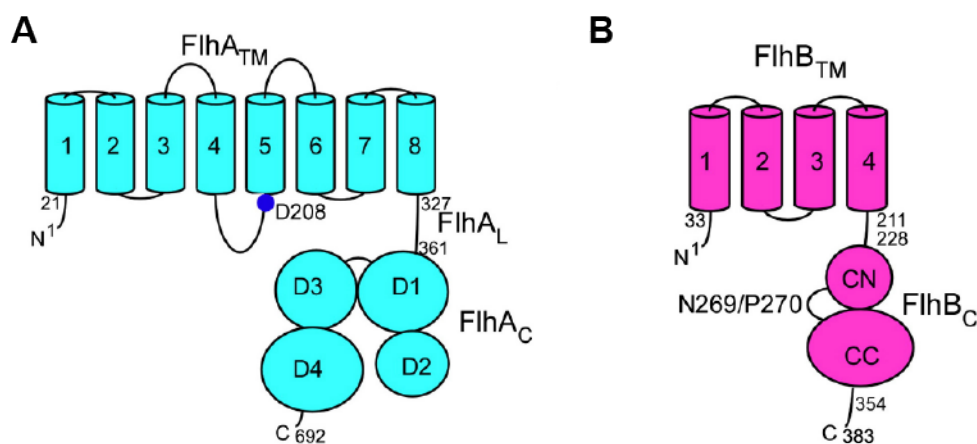


Figure 1-7 Structural topology of FlhA (A) and FlhB (B). Both FlhA and FlhB contain a N-terminal trans-membrane domain, FlhA_{TM} and FlhB_{TM}, and a C-terminal domain (FlhA_C and FlhB_C). FlhA_C consists of four domains, D1, D2, D3 and D4. A flexible linker (FlhA_L) connects FlhA_C with FlhA_{TM}. The highly

conserved Asp-208 is shown as closed circle (blue). FlhB_C undergoes autocatalytic cleavage at the site Asn269/Pro270 into FlhA_{CN} and FlhA_{CC}. After the autocatalytic cleavage, FlhA_{CN} and FlhA_{CC} become tightly associated with each other⁴.

MD simulations revealed that FlhA_C from *Salmonella enterica* fluctuates between open and close conformations⁷⁴. Mutational analysis of temperature sensitive mutants and suppressor mutations of G368C temperature sensitive mutants showed that FlhA_C from *Salmonella enterica* functions through multiple conformational states⁷⁴. Thus mutagenesis studies along with MD simulations indicate that FlhA_C is dynamic in nature and the dynamic motion of FlhA_C is crucial for its function. The crystal structure of FlhB_C is reported from two organisms, *Salmonella enterica* and *Aquifex aeolicus*⁷⁶. The crystal structure of FlhB_C consists of one globular domain composed of four β -sheets surrounded by four α -helices (Figure 1-7). A long N-terminal α -helix connects the globular domain of FlhB_C to the N-terminal trans-membrane domain of FlhB. The crystal structures from both *Salmonella enterica* and *Aquifex aeolicus*, show similar folds for the global domain but the conformation is different for the N-terminal α -helix⁷⁶. The globular domain of FlhB_C appears to be rigid as proposed from MD simulations whereas the N-terminal α -helix is very dynamic. The different conformations of N-terminal of FlhB_C from *Salmonella enterica* and *Aquifex aeolicus* might be due to its dynamic nature⁷⁶.

1.1.2.1.2 Soluble components of export apparatus

FliI is the peripheral membrane ATPase that plays central role in the flagellar assembly process^{77,78}. FliI belongs to the Walker-type ATPase family and shows

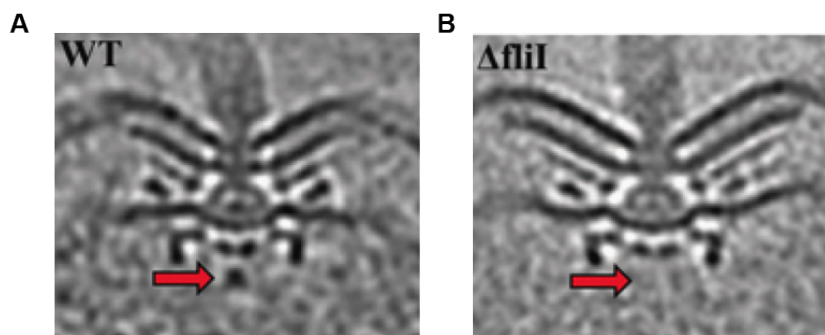


Figure 1-8 The cryo-electron microscopic image of FliI (from *C. jejuni*) hexameric ring at the cytoplasmic face of export apparatus. A. The spherical density of the FliI hexameric ring is indicated by red arrow. B. Δ FliI variant shows no spherical density. The diameter of the hexameric ring is ~10nm which matches well with the diameters of hexameric model of FliI (built with F₁-ATPase as template)⁶⁷.

significant sequence similarity to F₁-ATPase^{79,80,77,78}. The crystal structure of N-truncated fragment of FliI was reported and it shows significant structural similarity with the structure of α/β -subunits of F₁-ATPase^{81,82}. The amino acid residues of α/β -subunits of F₁-ATPase, involved in ATP hydrolysis, are highly conserved in FliI, indicating that both F₁-ATPase and FliI share similar catalytic mechanisms of ATP hydrolysis^{80,81}. In contrast to F₁-ATPase, which requires both α - and β -subunits to form $\alpha_3\beta_3$ hetero-hexameric ring for its enzymatic

activity⁸³, FliI forms homo-hexamer in solution⁸⁴. The homo-hexameric ring of FliI is visualized below the MS-ring complex by cryo-EM (Figure 1-8)^{84,85}. The external diameter of the FliI hexameric ring is \approx 10 nm with a 2.5-3.0 nm central cavity⁸⁴. FliI shows co-operative increase in ATPase activity in the presence of ATP or acidic phospholipids⁸⁴. Consistently, probability of FliI ring formation increases in presence of ATP, ATP analogs or acidic phospholipids^{84,86}. The extreme N-terminal residues of FliI control its oligomerization and marginally functional variants of FliI with deletion of first seven residues have been shown to be unable of forming ring structure⁸⁷. When hexamerization of FliI is suppressed by deletion of N-terminal seven residues, flagellar export diminished considerably, indicating that FliI hexamerization is crucial for efficient export process⁸⁷.

FliH is a negative regulator of the flagellar ATPase FliI and inhibits the ATPase activity of FliI⁸⁸. FliH can be divided into three regions, N-terminal (FliH_N), middle region (FliH_M) and C-terminal (FliH_C)⁸⁹. FliH shows significant sequence similarity to the b- and δ -subunits of F₀F₁-ATPsynthase^{90,91}. The b- and δ -subunit of F₀F₁-ATPsynthase connects the $\alpha_3\beta_3\gamma$ ring complex to the membrane embedded F₀ unit. FliH_M is responsible for its homodimer formation in solution⁸⁸. FliH_C interacts with the extreme N-terminal region of FliI to form (FliH)₂-FliI heterotrimer⁸⁸. FliH is responsible for the localization of (FliH)₂-FliI complex to the export gate. Other than FliI, FliH also interacts with general chaperone, FliJ⁶².

FliJ is another soluble component of the flagellar export apparatus.⁹² Similar to FliI and FliH, FliJ has intrinsic membrane affinity. FliJ plays crucial role in flagellar protein export since it interacts with all the other soluble components, FliH, FliI

and the cytoplasmic domain of FlhA.⁹³ The crystal structure of FliJ shows significant similarity to the crystal structure γ -subunit of F₁-ATPase⁹⁴. FliJ promotes FliI hexamerization at FliI:FliJ = 6:1 molar ratio but inhibits FliI ring formation at FliI:FliJ = 1:1⁹⁴. Although it inhibits the ring formation at FliI: FliJ = 1:1, it does not inhibit ATPase activity of FliI at the same molar ratio. Therefore FliJ might keep FliI in dimeric form at higher FliJ concentration.⁹⁴ FliJ shares similar bio-chemical properties like other flagellar export chaperones although it doesn't bind to any particular hook or filament type export substrates⁹². FliJ maintains secretion hierarchy for late export substrate complexes⁹⁵ and plays crucial role in the energy transduction mechanism of flagellar export process⁹⁶.

1.1.2.2 Interaction of flagellar export proteins among themselves and with the C-ring complex

The interactions among the flagellar export components have been studied extensively using genetic, biochemical and biophysical techniques^{61,62}. FliH forms heterotrimeric complex with FliI in the cytoplasm and regulates ATPase activity of FliI⁸⁸. The export defects of *fliH* null mutant of *Salmonella* are bypassed by either overproduction of FliI or by extragenic suppressor mutations of FlhA or FlhB⁹⁷. Therefore FliH is responsible for docking of FliI onto export gate formed by cytoplasmic domains of FlhA or FlhB. The extreme N-terminal of FliH is proposed to interact with FlhA or FlhB⁹⁸. Two conserved tryptophan residues at the extreme N-terminal region of FliH, Trp7 and Trp10, are essential for docking of FliI-FliH complex to the export gate^{99,100}.

The C-ring complex is also essential for flagellar assembly other than its role in torque generation and motor rotation¹⁰¹. FliN of the C-ring is involved in the export of filament specific substrates but export of rod-hook type proteins does not occur in *fliG*, *fliM* and *fliN* mutants of *Salmonella*^{63,77}. Both FliH and (FliH)₂-FliI complexes were reported to interact with FliN^{102,103,104}. The C-terminal part of FliN interacts with extreme N-terminal part of FliH. The (FliH)₂-FliI complex associates with FliM-(FliN)₄ to form stable (FliH)₂FliI-FliM-(FliN)₄ complex via interaction between FliH and FliN¹⁰². The reduced secretion activity of *fliN* mutant is considerably improved by overexpression of FliI¹⁰⁴. Thus C-ring provides initial docking site of (FliH)₂-FliI complex before their assembly in the export gate. The interaction between FliJ and FliM interferes with the interaction between FliH and FliN¹⁰². Also the extreme N-terminal residues of FliH are responsible for interaction with both FliN and the C-terminal of FliJ^{105,89,93}. Therefore interaction between FliJ and FliH releases the (FliH)₂-FliI from the C-ring for their assembly into the FlhA-FlhB platform of the export gate. After dissociation from the C-ring, the (FliI)₆-FliJ complex is formed at the FlhA_C and FlhB_C platform of the export gate and stably anchored to the export gate via interaction between FlhA_{TM} and FliH_{EN} (Figure 1-6).

1.1.2.3 Flagellar export chaperones and their substrates

Similar to cytosolic substrate-specific chaperones of T3SS of virulence bacteria, there are low molecular mass, acidic proteins, known as flagellar export chaperones, that provide stability to the late export substrates of flagellar assembly^{106,107,108}. These flagellar export chaperones neither have any ATP-

binding domain nor they have any resemblance to Hsp-related proteins^{106,107,108}. FlgN, FliS and FliT are the cytosolic chaperones for flagellar export apparatus^{109, 110, 111}. The crystal structures of all the three flagellar export chaperones, FliS, FliT and FlgN, were reported^{112,113}. Despite the functional similarities between flagellar type III export pathway and virulence type III protein secretion system, crystal structures of flagellar export chaperones are significantly different from the chaperones of type III secretion system (Figure 1-9).^{114, 115, 116, 117, 118, 119}. All the flagellar export chaperones share common structural motifs although they don't share common sequence similarity. The core structure of all flagellar export chaperones is comprised of anti-parallel amphipathic α -helical structure whereas the structure of T3SS chaperones is comprised of mixtures of α -helices and β -strands (Figure 1-9)^{130,131,132,133,134,135}.

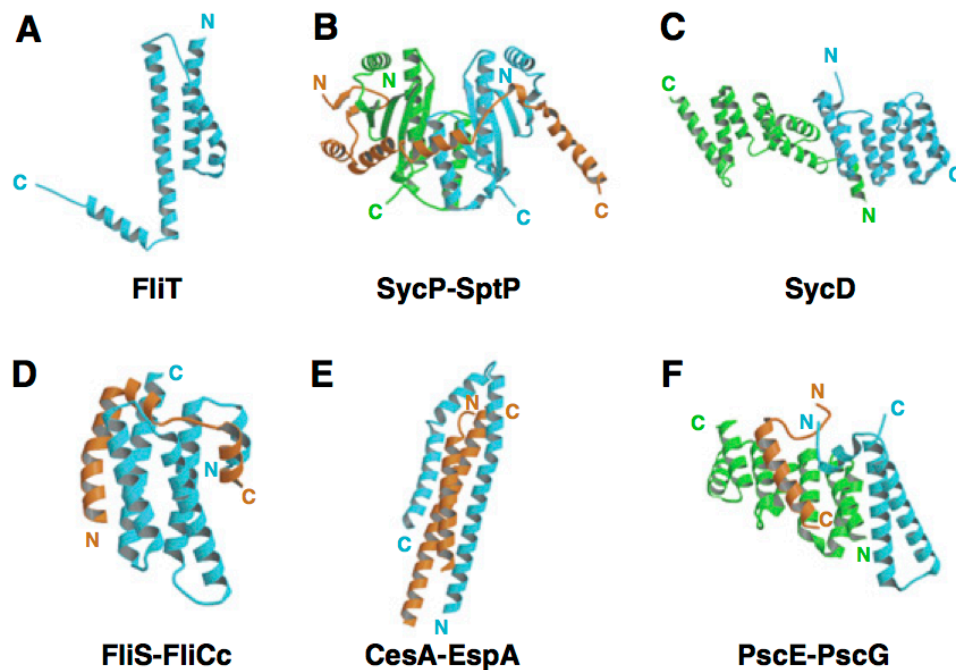


Figure 1-9 Comparison of crystal structures of different classes of type III specific chaperones. A. Monomer of FliT (pdb ID: 3A7M). B. SycP (class I) in complex with SptP (pdb ID: 1JYO), C. SycD (class II) (pdb ID: 2VGX), D. FliS (class III) in complex with the C-terminal segment of FliC (pdb ID: 1ORY), E. CesA (CesAB) (class IV) in complex with EspA (pdb ID: 1XOU), and F. PscE (class V)-PscG in complex with PscF (pdb ID: 2UWJ). All the chaperone molecules are shown in cyan and green; The SycP and SycD form homodimer. PscF forms heterodimer with its co-chaperone PscG. All the homo- or heterodimer is shown in cyan and green; the secretion or export substrates are shown in orange¹¹².

FlgN is the export chaperone for hook-associated proteins, FlgK and FlgL^{109,111}. FlgN provides stability to FlgK and FlgL in the cytoplasm and facilitates their export. FlgN is also required for the translation of FlgM¹²⁰. FlgM is an inhibitor of the flagellar specific transcription factor σ^{28} ¹²¹. The σ^{28} is required for transcription initiation of class 3 promoters that control expression of late flagellar export substrates¹²². FliT is a chaperone for the cap-forming protein FliD¹⁰⁹. FliT forms hetero-dimer in solution with FliD and stabilizes FliD in the cytoplasm from premature aggregation and is essential for its secretion^{111,112}. FliT also binds to FlhD₂C₂ tetrameric complex, preventing it from binding class 2 promoters. Thus FliT inhibits FlhD₂C₂ dependent transcription of class 2 genes¹²³ and negatively regulates class 2 gene expression maintaining optimal orders during flagellar assembly. The crystal structure of FliT consists of four anti-parallel amphipathic

α -helices. The anti-parallel α -helices, α_1 , α_2 and α_3 , form the core of FliT while α_4 helix is flexible. FliS is a chaperone for flagellin protein, FliC¹¹⁰. The crystal structure of FliS has anti-parallel four-helix bundle with a quasi-helical cap at one end formed by the 16 N-terminal residues of FliS (FliS_{EN})¹²⁴. The quasi-helical cap acts as plugs covering the hydrophobic pocket formed by an anti-parallel α -helical bundle. The crystal structure of FlgN was also reported (pdb ID 3OPC and 2FUP). The structural features of FlgN show similar folds to FliT and FliS crystal structures. These structural similarities of all flagellar export chaperones indicate their functional similarity as well.

In case of the flagellar type III export pathway, the extreme amphipathic C-terminal α -helical regions of flagellar export substrates bind to their cognate chaperones, unlike T3SS substrates for virulence bacteria, where the N-terminal of the substrate binds to the chaperone^{109,110,125}. Among the several flagellar chaperone-substrate complexes, the crystal structure of FliS-FliC complex was reported¹¹³ (Figure 1-9). FliC wraps around the anti-parallel bundle of FliS in an extended conformation covering the hydrophobic bundle. As a result, the hydrophobic plug formed by FliS_{EN} dissociates from FliS and forms a short helix. This mode of substrate binding via an extended non-globular conformation is similar to chaperone-substrate binding of T3SS of virulence bacteria^{126,113}. Therefore, although the flagellar export chaperones are structurally different from virulence type III secretion chaperones, their mode of substrate binding is similar.

1.1.2.4 Interaction of flagellar chaperone-substrate complex with export component proteins

The interactions between chaperones and chaperone-substrate complexes with export apparatus are crucial for highly efficient and ordered flagellar export. Both FliT and FliT-FliD complex interact with FliI¹¹². The C-terminal $\alpha 4$ helix of FliT controls its interaction with FliI and the truncation of C-terminal $\alpha 4$ helix considerably increases affinity of FliT to FliI¹¹². The FliT(1-94), a C-terminal $\alpha 4$ helix truncation construct of FliT, has two binding site on FliI. It interacts with the extreme N-terminal of FliI (FliI_{EN}) with high affinity and the C-terminal ATPase domain of FliI (FliI_{CAT}) with low affinity¹²⁷. FliH and FliT(1-94) are proposed to share common binding site on FliI_{EN}. FliH can displace FliT(1-94) from FliT94-FliI complex even in the absence of Mg²⁺ and ATP^{90,127}. Thus FliI_{EN} is transferred from FliT(1-94) to FliH by displacement at the common binding site of the FliI_{EN}. FliD binds to the hydrophobic cleft of FliT. Truncation of $\alpha 4$ helix does not affect the interaction of FliT(1-94) with FliD¹¹². FliD inhibits the strong interaction between FliI_{EN} and FliT(1-94)¹²⁷. FliD enhances the interaction between FliI_{CAT} and FliT(1-94)¹²⁷. Among the flagellar export substrates, both FliD and FliS are reported to interact with FliI¹²⁸. The ATPase activity of FliI is increased in the presence of hook protein, FlgE and flagellin, FliC in a reversible manner¹²⁸. Therefore FlgE and FliC might stimulate dimer or higher order oligomer formation of FliI. The FlgN-FlgK complex is also reported to bind to the (FliH)₂-FliI complex through the interaction between FliI and FlgN¹²⁹. As FliH binds to FliI_{EN} in the (FliH)₂-FliI complex, FlgN-FlgK complex is likely to bind to FliI_{CAT}. Therefore FliI_{CAT} are proposed to play an important role in substrate recognition. Considering 2.5-3.0 nm diameter of the central cavity of the modeled FliI

hexameric ring as well as other T3SS ATPases, it was hypothesized that secretory substrates have to be unfolded prior to their secretion to accommodate in the central cavity of the hexameric secretion pore of the ATPases. Consistently, InvC, a FliI homologue from *Salmonella* SP-1 T3SS, induces chaperone release from chaperone-substrate complexes and unfolds substrates in an ATP-dependent manner¹³⁰. However, FliI does not release FliT from FliT-FliD complex in the presence of ATP¹²⁷. Thus the ATPase FliI of flagellar type III export pathway might function in a distinct way compared to other T3SS ATPases of pathogenic bacteria.

A highly conservative hydrophobic dimple, located at the interface between the D1 and D2 domains of FlhA_C, is responsible for the interaction with late export substrates¹³¹. Among the export chaperones, FliS and FliT interact with FlhA_C only when they are complexed with their substrates, FliC and FliD¹³². Both FlgN and the FlgN-FlgK/L complex can interact with FlhA_C although binding affinity of the FlgN-FlgK/L complex is much higher than FlgN alone¹³¹. The extreme C-terminal residues of FlgN and FliT are critical for interaction with FlhA_C. In contrast, the extreme N-terminal residues of FliS are important for interaction with FlhA_C^{131,133}. In each case of late export substrate complex, one conserved tyrosine residue is involved in the interaction with FlhA_C. Tyr122 and Tyr106 of FlgN and FliT, respectively, are critical for interaction with FlhA_C whereas Tyr10 in the N-terminal of FliS abolishes interaction of the FliS-FliC complex with FlhA_C^{131,133}. Therefore, the mode of interaction of FliS-FliC complex is different

from that in FlgN-FlgK/L or FliT-FliD complex. This different mode of interaction is suggestive of different export mechanisms of FliC compared to FlgK/L or FliD.

The general chaperone, FliJ interacts with FlgN and FliT but not with FliS⁹⁵. FliJ shares common binding site on the FlgN and FliT with their respective substrates. The binding affinity of FlgN and FliT for FliJ are weaker compared to binding affinity of their respective substrates, FlgK/L and FliD⁹⁵. FliJ assists in recycling of free chaperones, FlgN and FliT, after release of subunits by an escort mechanism⁹⁵. Thus FliJ promotes initial, stoichiometric assembly of FlgK/L and FliD for formation of junction and cap proteins prior to high-throughput secretion of FliC.

1.1.2.5 The order of flagellar assembly

The order of flagellar export exactly parallels the order of flagellar assembly²⁰ (Figure 1-10). The flagellar assembly is regulated by a combination of transcriptional, translational and post-translational regulatory mechanisms¹³⁴. First of all, the hierarchical gene transcription of flagellar proteins regulates the flagellar assembly¹³⁵. Other than regulation of gene expression, the translational and post-translational regulations play significant roles in flagellar assembly. The completion of the hook formation is a major checkpoint for flagellar assembly²⁰. The rod-type (FliE, FlgB, FlgC, FlgF, FlgG) and hook-type (FlgD, FlgE, FliK) substrates are exported prior to the completion of hook structure⁶³. During their export process, the gene expressions of filament type proteins are inhibited in the cytoplasm by the flagellum-specific negative transcriptional regulator FlgM¹³⁶.

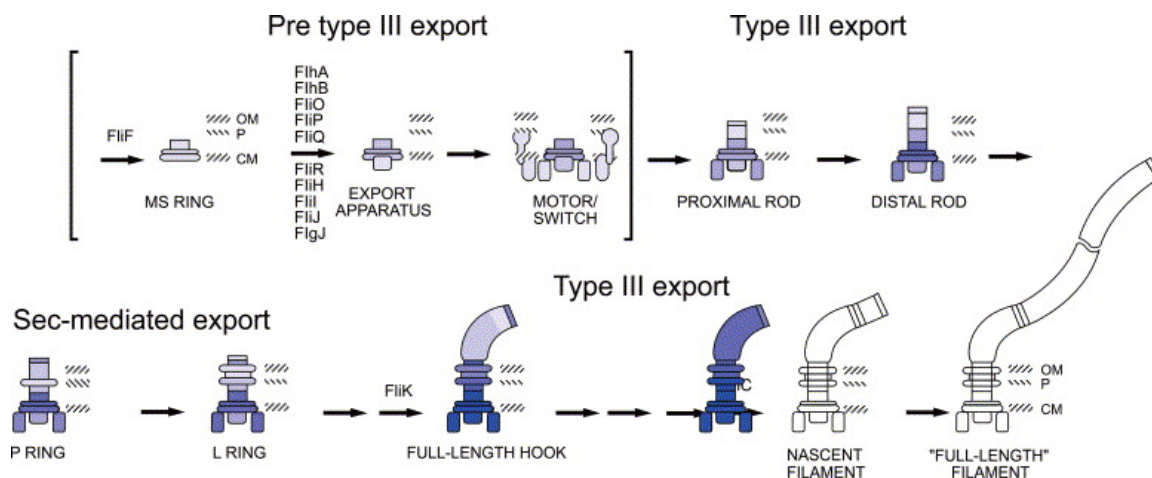


Figure 1-10 Order of export pathway in the flagellar morphogenesis in *Salmonella*. The flagellar substructures are colored from dark blue (early) to light blue (late) according to their stage of export. Integral membrane structures are assembled via sec-mediated export followed by assembly of peripheral structure. The type III export is used for rod, hook and filament assembly¹³⁷.

When the length of hook becomes 55 nm, the specificity of the flagellar export apparatus switches from rod/hook-type to filament type export⁵⁸. Then FlgM is secreted out of the cells triggering expression of filament specific export substrates^{138,139} and the assembly of filament begins. Two flagellar proteins, FliK and FliH, are involved in regulating the hook length and substrate specificity switching^{140,141,142}. The conformational change in FliH_C, followed by autocatalytic cleavage is essential for export switching process (Figure 1-11) FliK acts as molecular ruler and controls the length of the hook^{143,144}. The N-terminal region of FliK binds to hook cap and hook region, and the C-terminal domain is responsible for substrate specificity switching^{145,146,147}. During assembly of hook,

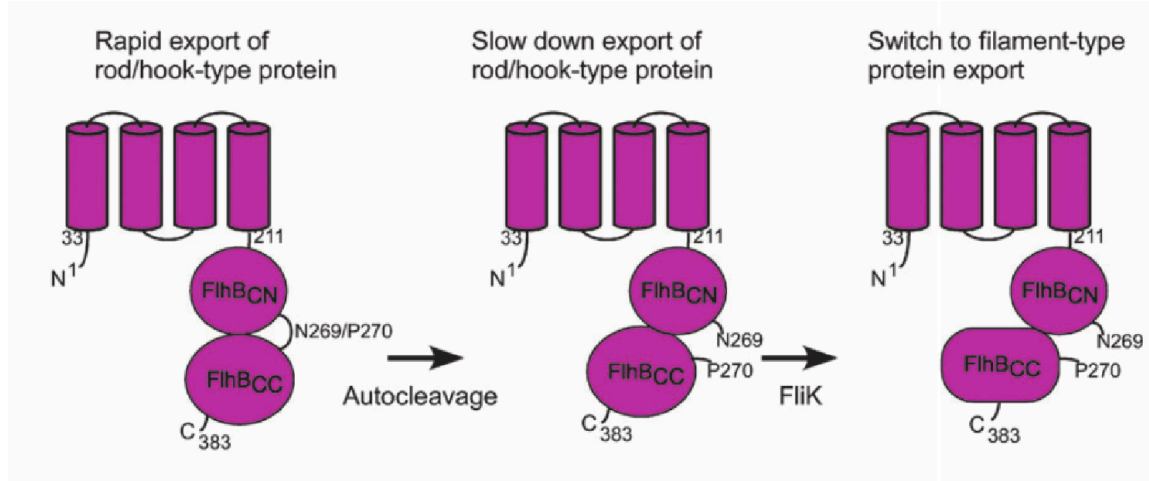


Figure 1-11 Mechanism of hook-length control and substrate specificity switching. Diagram shows cartoon structure of FlhB containing N-terminal transmembrane domain (magenta cylinders) and a C-terminal cytoplasmic domain (FlhB_C). FlhB_C undergoes autocatalytic cleavage at the site Asn269/Pro270 into two subdomains, FlhB_{CN} and FlhB_{CC}. FlhB_{CN} and FlhB_{CC} remains tightly associated with each other after cleavage. Initially FlhB_C exists in rod/hook-type specificity mode. Autocleavage of FlhB_C slows down the export rate of rod- and hook-type substrates. Then the interaction of FliK_C with FlhB_C induces a conformational change in FlhB_C leading to switching of the export specificity to filament-type mode²⁰.

FliK remains bound to hook cap. When the length of hook has reached to a certain position where the C-terminal of FliK can interact with FlhB_C, FliK-driven conformational rearrangement switches substrate specificity from early export substrates to late export substrates^{143,145,147}. Thus FliK and FlhB_C maintain the

hook length and switch substrate specificity from early export substrates to late export substrates. Interaction of late export chaperone-substrate complex with FlhA_C is critical for their export. Deletion of the D4 domain of FlhA_C results in leaky export of late exports substrates before the hook completion. Therefore FlhA_C plays significant role in maintaining the export order of rod-hook-filament substrates¹⁴⁸. The late export chaperone-substrate complex interacts with the hydrophobic dimple formed by D1 and D2 domain of FlhA_C¹³². The relative affinity of late chaperone-export substrates, FlgN-FlgK/L, FliT-FliD and FliS-FliC to FlhA_C determines the order of late substrate export^{131,133}.

1.1.2.6 Energy source for flagellar protein export

Many of the protein transport process across cell membranes occur in an ATPase-dependent way. FliI is the conserved ATPase for the flagellar export apparatus. As *FliI* null mutants as well as mutations in the catalytic domain of FliI result in total inhibition of export of flagellar proteins⁸⁰, FliI was also hypothesized to energize the export process. However, *fliH-fliI* double mutant of *Salmonella* is reported to form flagella with low efficiency, indicating that FliI is not essential for flagellar export^{149,150}. Certain mutations in FlhA and FlhB enhance the flagellar protein export and the motility of *fliH-fliI* double mutant. As FlhA and FlhB, act as the docking platform for (FliH)₂-FliI-chaperone-substrate complex, these gain-of-function mutants might enhance the probability of entry of flagellar proteins into the export gate¹⁵⁰. The (FliH)₂-FliI complex interacts with FliJ, FlgN as well as chaperone-substrate complexes, suggesting that (FliH)₂-FliI complex might guide the chaperone-substrate complex to the export gate and facilitate the initial entry

of export substrate to export gate¹⁵⁰. The mutations in catalytic domain of FliI inhibit the export process. Thus, ATP hydrolysis by FliI might be used for entry of export substrates into the export gate and release of (FliH)₂-FliI complex from the export gate^{150,88}.

Many biological protein transport processes use proton motive force (PMF) as major energy source for protein translocation¹⁵¹. In *Yersinia enterocolitica*, secretion of Yop proteins are inhibited in the presence of protonophore carbonyl cyanide m-chlorophenylhydrazone (CCCP), indicating that *Yersinia* type III secretion is dependent on PMF across the cell membrane¹⁵². The flagellar export was reported to depend on PMF¹⁵³. Flagellar export process was inhibited by protonophore CCCP in the presence or absence of FliH and FliI^{149,150}. PMF has two components, electric potential difference ($\Delta\Psi$) and proton concentration difference (ΔpH). For flagellar export process, two components of PMF play distinct roles^{150,154}. For wild type bacteria, $\Delta\Psi$ component alone is sufficient for efficient transport of proteins, but it requires both $\Delta\Psi$ and ΔpH , in the absence of FliI and FliH¹⁵⁴. The export of *fliH-fliI* double mutant of *Salmonella* shows solvent isotope effect while the wild type *Salmonella* does not exhibit any such effects. This indicates that proton translocation is the rate-limiting step for *fliH-fliI* double mutant¹⁵⁴. Therefore rate of proton transfer through the export gate determines the overall rate of flagellar protein export through the export gate alone. Thus the flagellar export gate, which is composed of six membrane proteins, was proposed to act as proton-protein antiporter for flagellar protein export¹⁵⁴. Apart from FliI and FliH, the general chaperone FliJ and the cytoplasmic domain of

FliA, play essential roles in flagellar energy transduction mechanism¹⁵⁴. Deletion of FliJ in the *fliH-fliI* double mutant further reduces the protein export activity of *Salmonella*. Similar to *fliH-fliI* double mutant, *fliH-fliI-fliJ* triple mutant export flagellar proteins in ΔpH -dependent way and P28T FliB mutation significantly enhances the export activity of *fliH-fliI-fliJ* triple mutant. *Salmonella* can export in ΔpH -dependent way in *fliJ* mutant in the presence of FliI and FliH. Therefore, other than FliI and FliH, FliJ is required for efficient, $\Delta\Psi$ -driven protein export¹⁵⁴. The interaction between 328-351 linker residues of FliA_C and 13-24 residues of FliJ is crucial for efficient flagellar protein export. Although *fliB* (P28T) mutant restore the motility of the Δ *fliH-fliI fliJ* mutant, it can't restore motility of Δ *fliH-fliI-fliA* (Δ 328-351), indicating that this linker region of FliA is essential for flagellar export¹⁵⁴. Therefore binding of FliJ induces specific conformations of linker region of FliA, which switches the export gate from low efficient proton-protein antiporter into highly efficient, $\Delta\Psi$ -driven export¹⁵⁴.

1.1.2.7 Mechanism of flagellar protein export

Although complete understanding of flagellar protein export is not available, a number of experimental data have been accumulated to provide a picture of the export process^{4,20}. Flagellar chaperones bind to their cognate substrate in the cytoplasm^{109,110}. FliH binds to FliI to form the (FliH)₂-FliI complex⁸⁸. Then (FliH)₂-FliI complex localizes to the C-ring complex via the interaction between FliH and FliN^{102,104}. The chaperone-substrate complex binds to the (FliH)₂-FliI complex through an interaction between FliI_{CAT} and the chaperone-substrate complex^{127,129}. FliJ binds to FliM of the C-ring¹⁰². Binding between FliJ and FliH

induces the release of (FliH)₂-FliI-chaperone-substrate complex from the C-ring¹⁰². Then the (FliH)₂-FliI-FliJ-chaperone-substrate docks to FlhA_C-FlhB_C platform of the export gate¹⁰⁵. FliJ facilitates the hexamerization of FliI at the export gate⁹⁴. FliH stably anchors the FliI₆-FliJ ring complex to the export platform by an interaction between FliH_{EN} and FlhA_{TM}⁹⁸. The chaperone-substrate complex binds to the hydrophobic dimple formed by D1 and D2 domain of FlhA_C^{131,133}. An interaction between FliJ and FlhA_C transforms the flagellar export process into highly efficient, $\Delta\Psi$ -driven export¹⁵⁴. The ATP hydrolysis by FliI promotes initial entry of N-terminal segment of the export substrate into the export gate followed by destabilization of the FliH_x-FliI₆-FliJ ring structure^{149,150}. After the release of the substrate into the export gate, FliH, FliI, FliJ and chaperone release from the export gate^{86,149,150}.

1.2 Nuclear Magnetic Resonance Spectroscopy

1.2.1 NMR as a tool in structural biology

NMR spectroscopy is a widely used biophysical technique in the field of structural biology to study bio-molecular structure, dynamics and functions^{155,156}. Other than X-ray crystallography, it is the only biophysical technique that can provide the three-dimensional structure of biomolecules at atomic resolution^{157,158}. The major advantage of solution NMR spectroscopy over X-ray crystallography is that one can study biomolecules in solution, which is closer to the physiological conditions. Moreover NMR can provide valuable information about protein dynamics over a broad range of time-scales from pico-seconds to hours at the residue level. Thus bio-molecular NMR can provide insight into conformational dynamics and exchange processes of bio-molecules and their complexes with ligands. NMR spectroscopy techniques can also be used to characterize denatured states of proteins, folding intermediates and sparsely populated, transiently formed bio-molecular conformations^{159,160}. Besides it provides critical insight into the kinetic study of folding and unfolding of biomolecules as well as detailed structural, dynamic and kinetic information of enzymatic reactions^{161,162}. NMR is useful to study broad range of bio-molecular interactions including protein-protein interaction, protein-ligand interactions, protein-nucleic acid interactions etc^{163,164}. Chemical shift mapping has been used to characterize protein-protein interactions and to localize ligand-binding site of the target protein¹⁶⁵. Thus solution NMR techniques are one of the most important techniques in the field of drug design and high-throughput drug screening.

Despite major advantages in solution NMR over other spectroscopic and biophysical techniques, one of its bottlenecks is the size-limit of bio-molecular complexes due to poor sensitivity and resolution of NMR spectra of large slowly tumbling bio-molecular complexes. Recent advances in the NMR hardware and methodology development significantly overcome the molecular size barrier by improving signal-to-noise (S/N) ratio (sensitivity) and spectral overlap (resolution). The development of multi-dimensional NMR, advanced isotope-labeling scheme and the introduction of TROSY-type pulse sequences, enabled the NMR study of large protein complexes upto 1 MDa^{166,167,168,169,170,171}.

1.2.2 Chemical shift assignment of protein

1.2.2.1 Backbone assignment

The first step in the NMR characterization of any protein starts with acquisition of

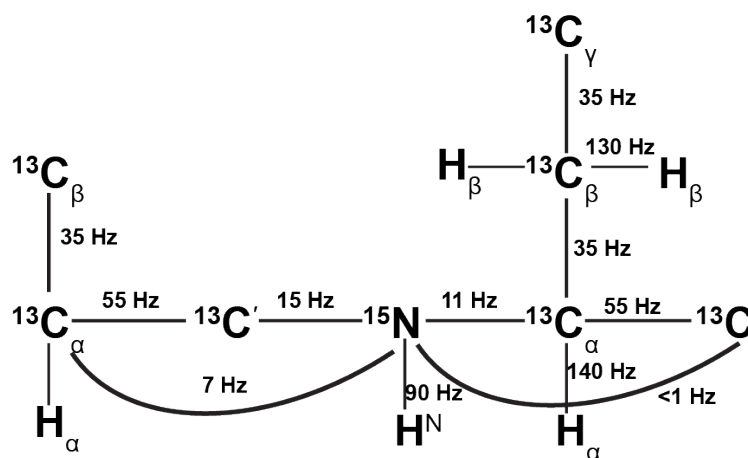


Figure 1-12 Spin system of the peptide backbone and size of the 1J and 2J coupling constants that are used for magnetization transfer in ^{13}C -, ^{15}N -labelled proteins.

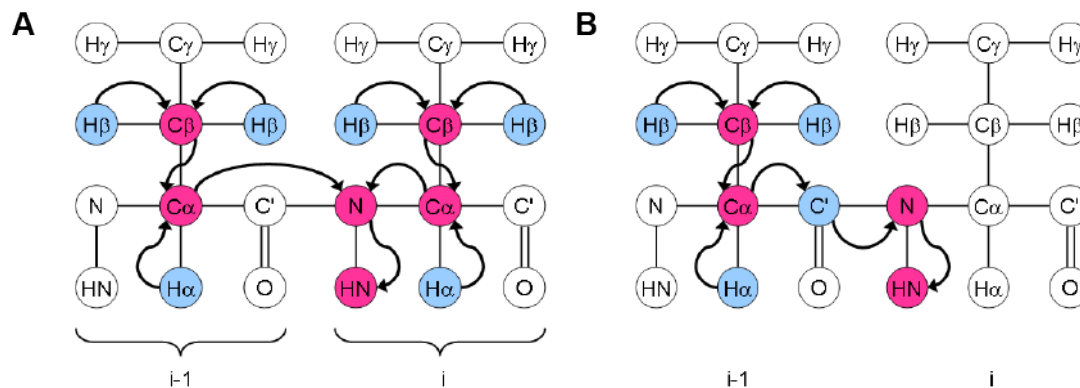


Figure 1-13 The magnetization transfer pathway in A. CBCANH and B. CBCACONH experiment.

heteronuclear single quantum coherence (HSQC) spectrum known as fingerprint of proteins¹⁷². In a typical ^{15}N -HSQC experiment, the magnetization is transferred from ^1H nucleus to the attached ^{15}N nucleus via J-coupling and then transferred back to ^1H nucleus for detection. Each protein has its own unique ^{15}N -HSQC spectrum. To investigate the structure and dynamics of a protein using NMR, it is necessary to assign the resonance peaks in a NMR spectrum to the corresponding amino acid residue. The sequential assignment of a protein can be obtained by correlating the chemical shifts of the amide group (NH) of a spin system with both inter- and intra-residues chemical shift of main chain (CO, $C\alpha$, N) or side-chain atom ($C\beta$ in case of HNCACB and HN(CO)CACB). The Figure 1-13 shows the through bond magnetization transfer in CBCANH and CBCA(CO)NH triple resonance experiments. A set of triple resonances, HNCA, HN(CA)CO, HNCACB, provides both the intra- and inter-residue correlations,

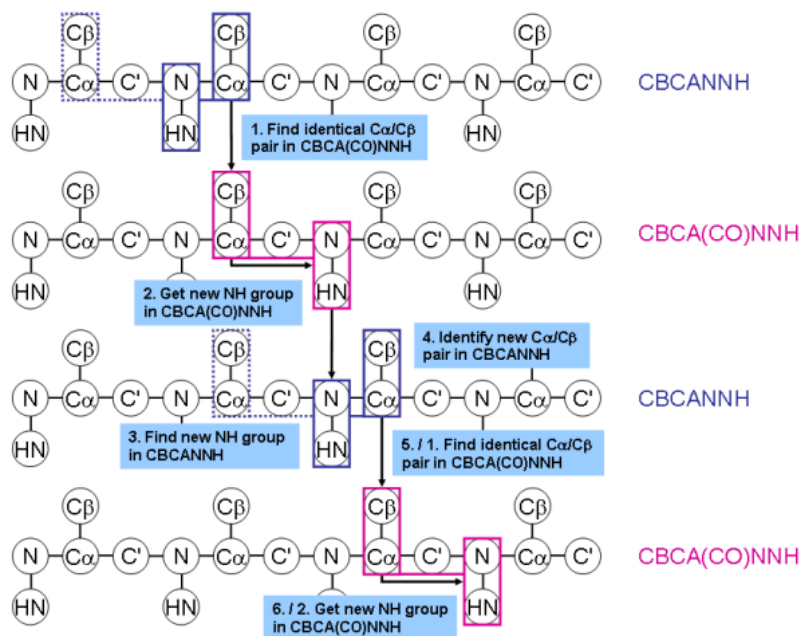


Figure 1-14 Assignment strategy for $^{13}\text{C}/^{15}\text{N}$ -labeled proteins based on CBCANH and CBCA(CO)NH 3D spectra.

while there are second set of experiments, HN(CO)CA, HNCO, HN(CO)CACB provides only inter-residue correlations. The second set of experiments is helpful to resolve ambiguity in case of overlapping peaks, especially for large proteins. For larger proteins, NOESY-based experiments like, ^{15}N -NOESY-TROSY, is also useful to assign and validate the assignment if crystal structure is available. Figure 1-14 illustrates the backbone assignment strategy based on CBCANH and CBCA(CO)NH spectra.

1.2.2.2 Side-chain assignment

After completion of the backbone assignment, the next step is the resonance assignment of side-chains. The side-chain can be assigned by a combination of three-dimensional H(C)(CO)NH, (H)(CCO)NH, ^{15}N - and ^{13}C -NOESY-HSQC, ^{15}N - and ^{13}C -NOESY-HMQC, HCCH-TOCSY and HCCH-COSY experiments¹⁷³. All these experiments correlate the ^1H - and ^{13}C -nuclei of the side-chain atoms of

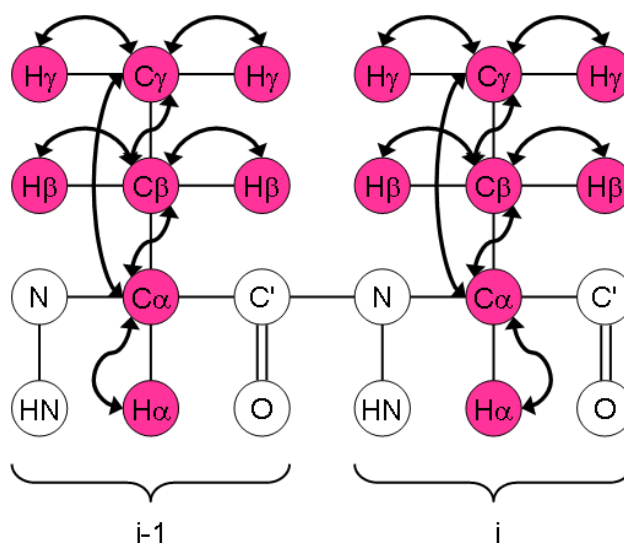


Figure 1-15 The magnetization transfer pathway in HCCH-TOCSY experiment.

the residue $i-1$ with the ^1H - and ^{15}N -nuclei of the amide of the residue i . HCCH-TOCSY and HCCH-COSY are the most useful spectra for side-chain assignment (Figure 1-15). HCCH-TOCSY and HCCH-COSY are specifically designed to correlate the side-chain aliphatic ^1H and ^{13}C resonances via C-H and C-C coupling constants. Combination of HCCH-TOCSY and HCCH-COSY provide nearly complete assignment of all aliphatic ^1H and ^{13}C resonances with the exceptions of Lys and Arg, which have long side-chains.

1.2.2.3 Nuclear Overhauser Effect Spectroscopy

The Nuclear Overhauser Effect (NOE) spectroscopy gives the correlation between spatially proximate nuclei (usually within 5-6 Å) and provides the distance restraints for structure calculations. The nuclear overhauser effect (NOE) originates from the dipolar interactions between different nuclei. The magnitude of NOE is inversely proportional to the sixth power of the inter-nuclear distance¹⁷⁴. In any NOE-based experiment, as in the case of 3D-NOESY-HSQC, the magnetization is exchanged between all the protons along the longitudinal Z-axis during a mixing period. Afterwards, the magnetization is first transferred to the neighboring ¹⁵N or ¹³C nuclei to achieve further resolution by separating overlapping ¹H resonances along the heavy atom chemical shift dimension and then transferred back to the ¹H nuclei for detection. For each NH group, all ¹H nuclei within 5-6 Å will provide NOE correlations. Similarly, NOE's between side-chain ¹H nuclei can be obtained from ¹³C-NOESY-HSQC or ¹³C-NOESY-HMQC spectra. For larger proteins or protein complexes, the NOESY spectra are usually over-crowded. In that case 4D ¹³C-HMQC-NOESY-HMQC or ¹³C-HSQC-NOESY-HSQC can be used for spectral assignment or distance restraints for structure calculations^{175,176,177}.

1.2.2.4 TALOS

TALOS (Torsion Angle Obtained Likelihood from Shift and sequence similarity) is a database system that empirically predicts *phi* and *psi* backbone torsion angles for a given protein sequence (Figure 1-16) using backbone of chemical shifts (HA,

CA, CB, CO, N)¹⁷⁸. TALOS searches the database for triplets of adjacent residues with secondary chemical shifts and sequence similarity in order to provide the best match to the query of triplet of interest. The current database of TALOS contains ^1HN , ^{15}N , $^{13}\text{C}'$, $^{13}\text{C}_\alpha$ and $^{13}\text{C}_\beta$ chemical shifts for around 200 proteins with available high-resolution crystal structure. The goal of the TALOS is

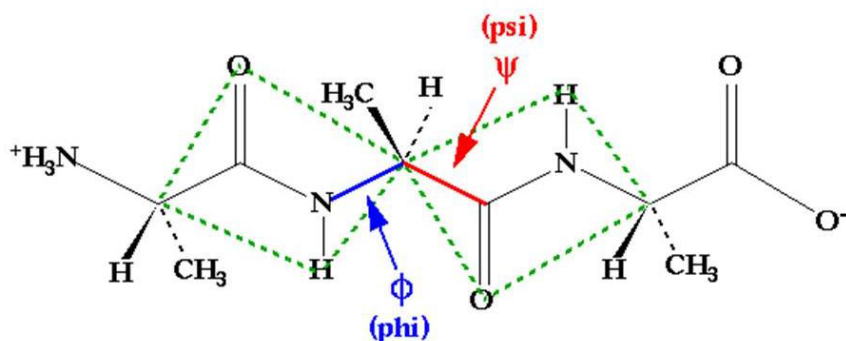


Figure 1-16 Backbone (dihedral) angles in the protein structure.

to make quantitative predictions for the protein backbone angles. The output of TALOS consists of ten triplets that have closest similarity in the secondary chemical shift. If the central residues in these 10 triplets show similar backbone angles, their averages can be reliably used as angular restraints for the protein under study. An improved version of the TALOS system, TALOS+, has been developed and used for predicting the backbone torsion angle more accurately¹⁷⁹.

1.2.3 NMR study of large protein complexes

The NMR study in the large protein systems has been challenging because of poor spectral quality due to severe line broadening effect and spectral overlap

(Figure 1-17)^{180,181}. The line broadening is the result of fast transverse relaxation rate (R_2) due to slow tumbling of large molecular weight proteins. The development of methodologies such as deuteration of proteins, TROSY-based pulse sequences, selective isotope labeling has significantly overcome the limitations of the molecular weight barrier. However, although deuteration of proteins dramatically improves spectral quality, numbers of observable NOEs are also decreases considerably. Therefore several isotope-labeling schemes have been developed to overcome this issue: a. site-directed protonation of uniformly deuterated

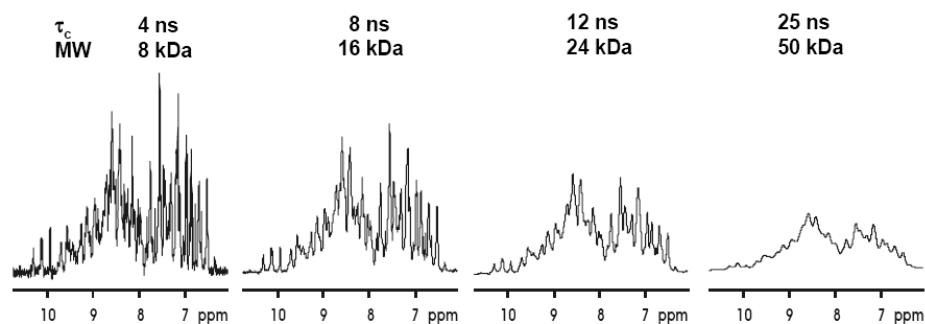


Figure 1-17 Effect of molecular weight in the linewidth of the NMR spectra. The linewidth is proportional to T_2 ($\Delta\nu = 1/\pi T_2$)¹⁵⁹.

protein at crucial positions, either by introducing protonated amino acids e.g., Phe, Tyr, Ala, Lys or selectively protonating methyl groups of hydrophobic amino acids, such as Ile, Met, Ala, Leu, Val, by the use of selectively labeled precursors; b. use of random fractional deuteration¹⁸².

1.2.3.1 Protein deuteration

One of the major sources of relaxation in the large protein complexes is spin-spin relaxation from the high proton density. The strategy to overcome the spin-spin relaxation is the uniform deuteration of the proteins^{183,167}. There are several advantages of ²H labeling¹⁸². The substitution of the ²H spin for ¹H ($\gamma_D/\gamma_H \sim 1/6.5$) causes the significant reduction of the heteronuclear dipolar relaxation of the ¹³C spin so that ¹³C T_2 will be improved by a factor of 16. This effect significantly improves the triple resonance experiments involving ¹³C _{α} spins as ¹³C spin usually the fastest relaxing spin in the peptide fragment via the bound H _{α} moiety. Secondly the spin diffusion through the homo-nuclear proton/proton relaxation pathways is reduced due to smaller populations of ¹H spins. This effect is more pronounced in case of higher molecular weight proteins. In overall, the spin diffusion results in the line-width narrowing of the observed protons. To achieve the uniform deuteration, the protein of interest was over-expressed in a completely deuterated medium followed by transfer into protonated buffer for the exchange of backbone N-²H into N-H groups. The deuteration of proteins dramatically improves the sensitivity and the resolution of the spectra.

1.2.3.2 Transverse relaxation optimized spectroscopy

The spin relaxation signal in NMR experiments decay exponentially with the transverse relaxation time, T_2 and the line width ($\Delta\nu$) is inversely proportional to T_2 . Compared to small molecules, the decay of NMR signal for slowly tumbling large macromolecules is faster, due to smaller T_2 , resulting both weaker signal

and broad line width (Figure 1-18 a and b). In conventional heteronuclear correlation experiments, the correlations between different spins (e.g., ^{15}N and its attached ^1H) are obtained through one-bond J-coupling. The result of the J-coupling is the splitting of the observed signal from each nucleus into a set of quartets. The cross-correlated relaxation caused by dipole-dipole relaxation and

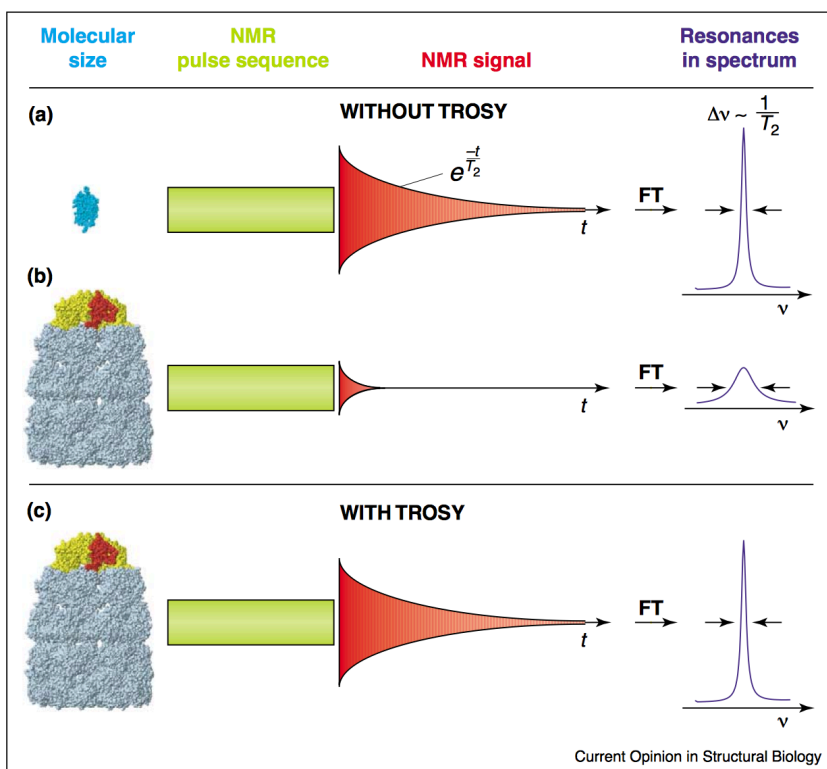


Figure 1-18 NMR spectroscopy with small and large molecules in solution and the effect of TROSY on large molecules¹⁸⁰.

chemical shift anisotropy gives rise to different relaxation rates of the individual components of quartets. In a typical HSQC experiments, the splitting is refocused to obtain a single signal. In TROSY-based pulse sequences, the slowly relaxing

components are selected via spin manipulation^{184,168}. Therefore, narrower line width and higher resolution can be obtained with the higher magnetic field (Figure 1-18). Nowadays, the TROSY principle has been incorporated into a number of NMR pulse sequences commonly used for protein NMR study¹⁸⁰. TROSY works best for deuterated protein sample and it has significantly extended the size limit of biomolecules upto 1 MDa^{170,185}.

1.2.3.3 Selective labeling of methyl groups

Perdeuteration of a protein sample results in a complete elimination of protons. Therefore selective protonation is required to obtain NOE necessary for distant restraints. Methyl groups are important probes in the protein NMR studies because they are very frequently present in the hydrophobic core of proteins or

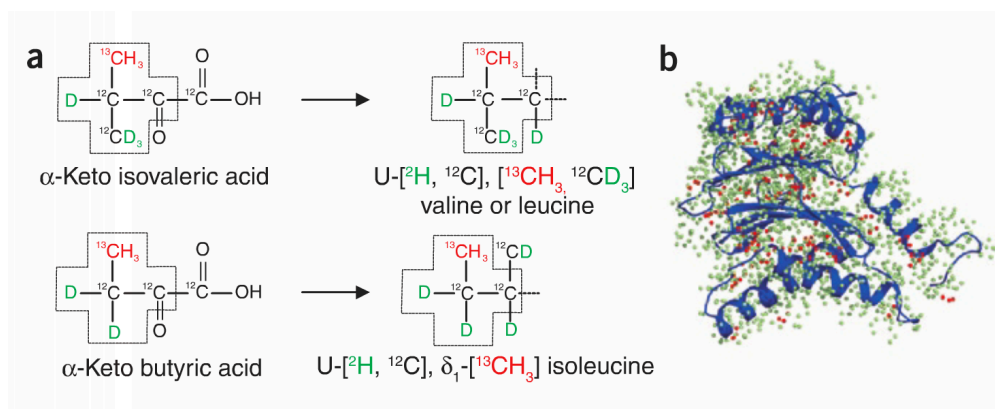


Figure 1-19 Methyl labeling strategy. (a) Precursors used to produce proteins with methyl labeling (¹³CH₃) in isoleucine, leucine and valine (b) Ribbon diagram of the α subunit of *T. acidophilum* proteasome highlighting the labeling scheme used. Isoleucine (δ_1), leucine and valine methyl groups are indicated in red and deuterons in green¹⁹¹.

the interface of protein complexes¹⁸⁶. These factors facilitate the measurement and assignment of long-distance amide-methyl and methyl-methyl NOEs that will allow global folds of large proteins to be determined^{187,188}. All three protons of the methyl group contribute to the intensity of the same signal. Therefore the methyl group as a probe produces more sensitive signal than other NMR probes. The methyl groups rotate very rapidly about its three-fold symmetry axis and give rise to favorable relaxation properties¹⁸⁹. Moreover, the methyl regions of ¹H-¹³C correlation spectra are usually well resolved¹⁶⁷. The NOE-derived distances between spatially proximal methyl groups gives the distance restraints for protein structure determination¹⁹⁰. Several methodologies have been developed for selective protonation of specific methyl groups allowing these to be monitored with backbone amides. Use of metabolic precursors enables the selective protonation of specific methyl groups of Ile, Leu and Val in an otherwise completely deuterated background¹⁹¹ (Figure 1-19). Recently, the selective methyl labeling strategy has been developed for Ala^{192, 193, 194}, Met¹⁹⁵, and Thr^{196, 197} residues also. The selective labeling of threonine is particularly important because they usually localize to the surface of the proteins. They have unique hydrogen bonding capabilities and have a higher propensity to be found at the protein-nucleic acid interfaces. Threonine also plays important role in signaling pathways through phosphorylation¹⁹⁵. Thus methyl groups are excellent reporter of bio-molecular structure and dynamics.

1.2.3.4 Structure calculation using sparse NMR data

Once all the experimental data (distance restraints from NOE, PRE, dihedral angle restraints, RDC) have been collected, it is used as an input for the protein structure calculation. The idea behind computer-aided structure calculation is to convert all the experimental constraints into a three-dimensional (3D) structure. A polypeptide chain with random initial configuration is folded into the 3D structure using experimental restraints and a suitable force field that accounts for the energy terms that govern proteins in solution and contain terms for the experimental restraints used. The energy optimization process continues until an energy minimum is reached. The structure calculation software produces an ensemble of structures consistent with experimental NMR data. Several well-established software packages like, ARIA¹⁹⁸, CYANA¹⁹⁹, XPLOR-NIH²⁰⁰, HADDOCK²⁰¹, are available for computer-aided structure calculation. There are softwares available such as CING, Molprobit, Procheck, PROSESS, PSVS that can be used to validate the protein structures based on a variety of biophysical and statistical parameters, and agreement with experimental data^{202,203,204,205,206}.

1.2.4 NMR study of protein interactions

Bio-molecular interactions play important role in all biological process. NMR is a powerful tool to characterize various ranges of biological interactions e.g. protein/protein interactions, protein-nucleic acid interaction, protein-ligand interactions etc^{163,207}. NMR can study biological interactions in solution, which is closer to physiological conditions. There are biological interactions, which are weak and transient, and the protein complex of interest cannot be crystallized easily. NMR spectroscopy has unique ability to characterize such weak and

transient interaction. Variety of experiments have been developed to study bio-molecular interactions such as chemical shift perturbation (CSP) mapping, saturation transfer difference spectroscopy (STD), differential line broadening, transferred cross-saturation experiments (TCS), isotope labeling methods, residual dipolar coupling, paramagnetic relaxation enhancement (PRE), pseudo-contact shift (PCS), residual chemical shift anisotropy (RCSA) etc^{163,208,209,210,211,212}. Chemical shift perturbation is the most widely used NMR method to characterize protein-protein interaction^{213, 214}. Chemical shift perturbation works best for weak interactions in the fast exchange regime.

1.3 Isothermal Titration Calorimetry (ITC)

The isothermal titration calorimetry (ITC) is one of the most versatile and powerful calorimetric techniques that can measure all the thermodynamic parameters of bio-molecular interaction in a single experiment²¹⁵. ITC covers broad range of bio-molecular interactions including protein-protein interactions, protein-nucleic acid interactions, protein-small molecule interactions, protein-lipid interactions, protein-carbohydrate interactions, enzyme kinetics etc²¹⁵. ITC can be used to study bio-molecular interactions with broad range of dissociation constants between 100 μM to 10 nM^{215,216}. Modification of the experimental design using competition methods has been utilized to extend the range of dissociation constants for weaker and stronger binding²¹⁶. No chemical tagging or immobilization is required for ITC. There is no molecular weight limitation of bio-molecules or bio-molecular complex for ITC measurement. ITC directly measures the heat evolution or absorption during the course of bio-molecular

interaction. It is capable of measuring the heat changes over a wide variety of solution conditions and temperatures. The thermodynamic parameters that can be obtained by ITC include Gibb's free energy change (ΔG), the enthalpy change (ΔH), the entropy change (ΔS) and the stoichiometry (n) of the bio-molecular interaction. Besides, ITC provides the heat capacity change (ΔC_p) of a binding reaction by performing ITC experiments at variable temperatures²¹⁷. Multiple binding sites of biomolecules or ligands can be identified and independently studied by ITC. ITC provides powerful insight into the binding mechanism of bio-molecular interaction. The change in Gibb's free energy (ΔG) is the measure of overall thermodynamic stability and binding affinity of any bio-molecular complex. The enthalpy change (ΔH) is a measure of protein-solvent hydrogen bonds, vander Waal's interactions, protein-ligand bonds, salt bridges and solvent reorganization near protein surfaces²¹⁸. The entropy change (ΔS) gives information about hydrophobic interactions, conformational changes, and water and ion release from the interaction surface²¹⁹. Besides ITC is the only technique that can provide insight into the differential contribution of the enthalpy change (ΔH) and the entropy change (ΔS) bio-molecular interaction of binding energy (ΔG).

1.4 Multi-Angle Light Scattering (MALS)

Multi-Angle Light Scattering (MALS) is an analytical technique for determining absolute molar mass of macromolecules in solution such as proteins, polymers, liposomes, micelles, colloids etc. The molar mass measurement using MALS can be performed either in continuous flow mode or in stand-alone batch mode.

MALS is most commonly used in-line with size-exclusion chromatography²²⁰ although it can be used with any other non-size separation method like HPLC or IC. MALS measures molar mass by calculating the amount of scattered light at each angle detected. The amount of light scattered is then related to molar mass of the macromolecule. Light scattering provides absolute measurements because the determination of molar mass is made without reference to any molar mass standard, column calibration or molecular conformations. Other than molar mass, light scattering give measurement of the root mean square radius of the molecule and the hydrodynamic radius. SEC-MALS is particularly useful to determine accurate molecular weight of non-globular protein, with elongated shape, which elutes in anomalous position in gel-filtration. Besides molar mass measurements, the light scattering is used for studying bio-molecular interactions. Composition-Gradient Multi-Angle Light Scattering (CG-MALS) is a label-free and immobilization-free versatile technique that can characterize self- and hetero-association, binding affinity from pM to mM, absolute molecular stoichiometry, multi-valent or co-operative interactions, kinetics of binding, aggregation or dissociation over time scales of seconds to hours^{221,222}. CG-MALS utilizes the Calypso multi-syringe pump system (Wyatt Technology Corporation), which is programmed to provide stop-flow injections at a series of well-defined concentrations or compositions. Then the data, acquired at each step, is analyzed using Calypso software, to provide the dynamic equilibrium properties of bio-molecular interaction^{221,222}. CG-MALS is unique to all other biophysical

techniques as it can characterize bio-molecular interactions by measuring their absolute molar mass.

1.5 ATPase Assay

ATPases are enzymes that catalyze the hydrolysis of ATP to ADP and inorganic phosphate. This dephosphorylation releases energy, which is used in different important biological process like transport, signal transduction, protein biosynthesis, cell differentiation etc. The hydrolysis rates of the ATPases are correlated with the enzyme activity, which is an important functional parameter. ATPase assay is a biochemical assay to measure ATPase activity by either quantitating liberated inorganic phosphate (Pi) or adenosine di-phosphate (ADP) during enzymatic reaction. There are several methods available for characterization of ATPase activity^{223,224,225}. One of the highly sensitive methods of measuring ATPase activity is ADP-glo Kinase Assay measurement²²⁶. The ADP-glo Kinase Assay measures generation of ADP during any ADP generating bio-chemical reactions. The assay is performed into two steps. Firstly, ADP-glo reagent is added to stop the ATPase reaction at different time points and deplete the remaining ATP. Then kinase detection reagent is added to convert ADP to ATP and to quantitate the newly synthesized ATP using luciferase/luciferin reaction. The light emitted is measured using a luminometer. The recorded luminescence is then correlated with ADP conversions by using an ADP-to-ATP conversion curve. The amount of ADP conversion with is correlated with enzyme activity.

Chapter 2 : Research Outline.

The interaction between flagellar export chaperones with the flagellar ATPase is required for efficient delivery of the flagellar export substrate. It is important to understand the detailed biophysical and structural information about the chaperone-ATPase interaction to elucidate their role in the flagellar export process.

(1) Biophysical characterization of the interaction between FliI and FliT.

FliT is the export chaperone for the flagellar cap-forming protein, FliD. Interaction between flagellar ATPase, FliI and FliT, was reported in literature¹²⁷. Biochemical assays showed that FliI has two distinct FliT-binding sites. We have used solution NMR along with other biophysical techniques to characterize the interaction between FliI and FliT. Detailed insight into the interaction between FliI and FliT will provide mechanistic insight of the role of chaperone-ATPase interaction in flagellar type III export pathway.

(2) Solution structure determination of FliI-FliT complex.

No structure of a chaperone-ATPase complex has been reported to date. We have used solution NMR techniques to determine the solution structure of FliI-FliT complex. The solution structure of FliI-FliT complex will provide the first high-resolution structure of a chaperone, FliT with T3SS type III ATPase, FliI.

Chapter 3 : Chemical shift assignment of FliI

3.1 Introduction

FliI is a 50 kDa ATPase that belongs to Walker type of ATPase family⁸⁰. It is hypothesized to form homohexamer during flagellar protein export^{84,86,87}. It shares sequential and structural similarity to α - and β -subunits of F₁-ATPase

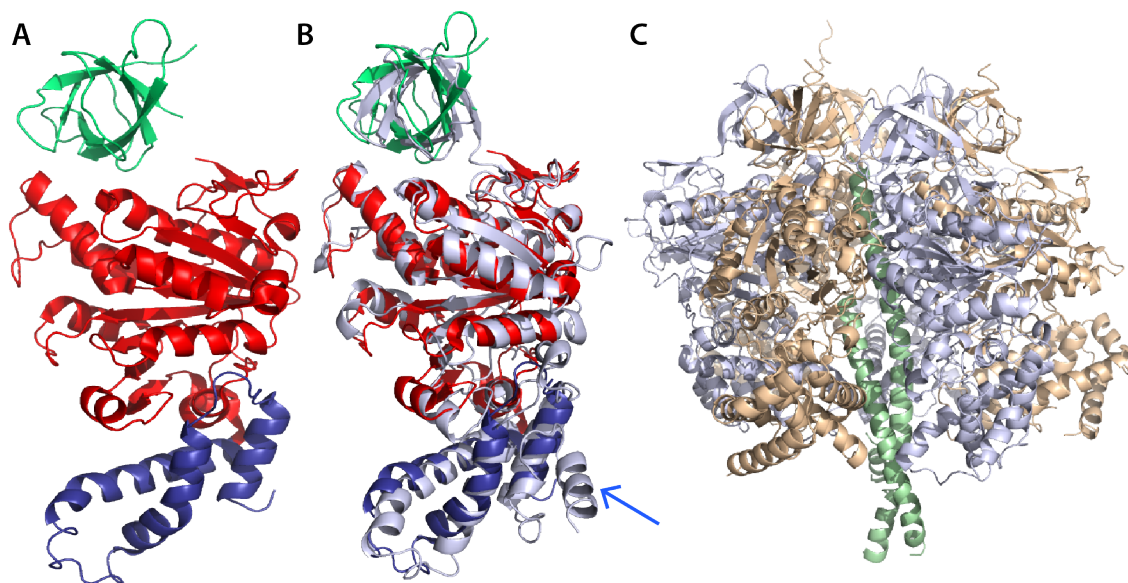


Figure 3-1 The crystal structure of FliI. A. The crystal structure of FliI(18-456), pdb ID: 2DPY. Color code: the N-terminal β -barrel domain, green; ATPase domain, red; C-terminal domain, blue. B. Structural comparison of FliI(18-456) with β subunits of F₁-ATPase (pale blue). The additional α -helix in β subunits of F₁-ATPase is shown by blue arrow. C. The crystal structure of F₁-ATPase (pdb ID: 1BMF).

as well as other homologous T3SS ATPases^{77, 78}. The crystal structure of Flil (Δ 1-18) was reported⁸¹. The overall structure of Flil can be divided into three domains, N-terminal domain (Pro-23 to Arg-97), the ATPase domain (Gln-109 to Ile-380), and the C-terminal domain (Thr-381 to Val-456) (Figure 3-1). The N-terminal domain has a β -barrel structure composed of six β -strands. The ATPase domain consists of both α/β domains containing a Rossmann fold²²⁷. The P-loop inside the ATPase binding domain contains the Walker A and Walker B motif⁷⁹. The C-terminal domain of Flil consists of three α -helices connected by two loops. There is a long loop between the N-terminal barrel domain and the ATPase domain. The extreme N-terminal residues of Flil are proposed to be flexible since they are not visible in the crystal structure⁸⁷ and susceptible to proteolysis⁹⁰. The ATPase domain of the Flil has higher sequence similarity (29 %) with the α/β subunits of F_1 -ATPase compared to the N-terminal barrel domain and the C-terminal domain (17 % and 13 %, respectively)^{77,81}. Despite the different sequence similarity between different domains of Flil, the structure of all the three domains of Flil is remarkably similar to the α/β subunits of F_1 -ATPase⁸¹. As the functional form of Flil is homo-hexameric and Flil is structurally very similar to α - and β -subunits of F_1 -ATPase, the hexameric model for Flil hexamer was built using F_1 -ATPase (pdb code 1BMF) structure as a template⁸¹ (Figure 3-1). The main chain structures constructing the subunit interface and surrounding the central channel are well conserved for both Flil and F_1 -ATPase. All the structural difference lies outside the hexameric ring. The residues of Flil that are conserved in the α -subunits of the F_1 -ATPase interact with the residues of Flil, which are

conserved in the β -subunits of FliI, in the hexameric model of FliI⁸¹. These structural features of FliI are essential for its homohexamericization. The extreme N-terminal residues of FliI are responsible for its oligomerization⁸⁷. An N-terminal

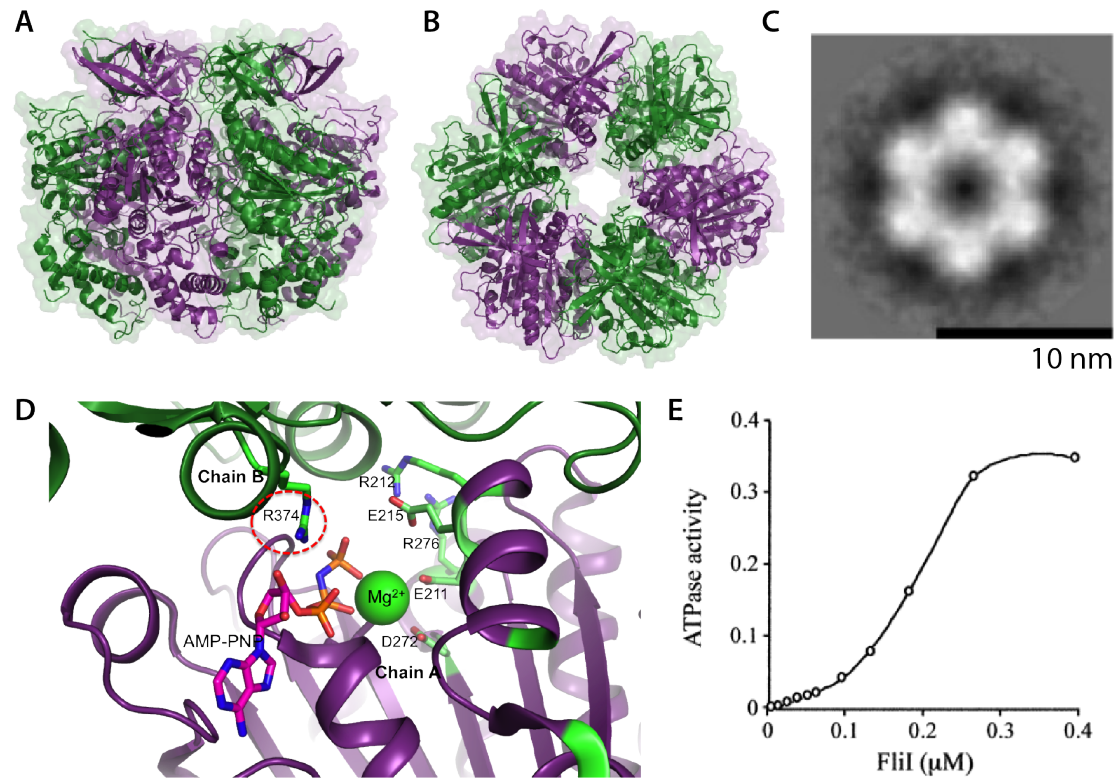


Figure 3-2 Hexameric model of FliI built using F₁-ATPase (1BMF) as template. A. Side view. B. Top view. The alternate subunits in A and B are colored as green and purple. C. The hexameric ring structure of FliI by Cryo-EM. The image represents averaged end-on view of frozen-hydrated ring particles formed by FliI with Mg²⁺-ADP-AlF₄. The scale bar indicates 10 nm⁸⁶. D. The active site of FliI modeled using F₁-ATPase as template. Arg374 of neighboring subunit is shown using dotted circle. E. ATPase activity of FliI was measured with different enzyme

concentrations in the presence of 5 mM ATP. FliI shows co-operative effect of ATPase activity with concentration⁸⁴.

seven-residue deletion construct of FliI is unable to form ring structure⁸⁷. Unlike F₁-ATPase, which forms stable $\alpha_3\beta_3$ heterohexamer, the homohexamer of FliI is unstable in solution. Therefore external factors are required for ring formation of FliI. FliI is proposed to form hexamer at the export gate platform made up of FlhA_C and FlhB_C^{57,64}. The hexameric ring formation of FliI is stimulated in the presence of ATP analog or acidic phospholipids^{84,86,87}. Although the hexameric form of other T3SS ATPases have been reported in solution^{228,229,230}, FliI hexameric ring structure is only reported by cryo-EM^{84,86} (Figure 3-2) and fluorescence microscopy study²³¹. FliI efficiently forms ring structure in the presence of Mg²⁺-ADP-AIF₄ but not in the presence of Mg²⁺-ATP. The FliI-E221Q mutant binds to ATP with same affinity as WT FliI but is unable to hydrolyze ATP. This FliI-E221Q forms ring structure in the presence of Mg²⁺-ATP. Therefore hexamerization of FliI is stimulated by ATP binding and the ATP hydrolysis destabilize the ring structure⁸⁶. This assembly and disassembly of FliI during ATP hydrolysis is supportive of the hypothesis that FliI interacts with the export apparatus in a dynamic fashion and ATP hydrolysis of FliI is coupled to the initial entry of export substrate into the export gate^{78,86,149,150}.

All the residues involved in the ATP hydrolysis of F₁-ATPase are conserved in FliI⁸¹. Thus the mode of nucleotide binding and catalytic pathway of ATP

hydrolysis of FliI should be similar to that in F₁-ATPase⁸¹. All the point mutations in the catalytic core of FliI result in significantly diminished or no ATPase activity⁸⁰. The $\alpha_3\beta_3$ heterohexamer formation is necessary for ATPase activity of F₁-ATPase. The conserved Arg-373 residue in the α -subunit of F₁-ATPase stabilizes the negative charge of the γ -phosphate in the transition state for catalysis^{82,232,233}. Site-directed mutagenesis of the corresponding arginine in FliI, Arg374, to alanine results in loss of ATPase activity⁸⁶. Therefore ATP might bind to the dimeric interface of FliI similarly to F₁-ATPase (Figure 3-2, D) and oligomerization of FliI should be coupled to its ATP hydrolysis. Indeed, FliI shows positive co-operativity of ATP hydrolysis (Figure 3-2, E)⁸⁴. Accordingly, acidic phospholipid, which promotes oligomerization of FliI, also stimulates its ATPase activity⁸⁴. FliH inhibits the ATPase activity of FliI by keeping it in the monomeric form^{88,90}. As the extreme N-terminal region (residues 1-7) of FliI controls its ring formation, deletion of N-terminal residues of FliI results in loss of catalytic activity⁸⁷.

3.2 Results

3.2.1 Biophysical characterization of FliI

Although full length FliI is reported to have intrinsic membrane affinity²³⁴, it is a soluble protein. Overexpression of FliI fused to the Maltose binding protein (MBP) tag in *E. coli* yields significant amounts of soluble proteins both in LB media, and protonated and deuterated minimal media necessary for solution

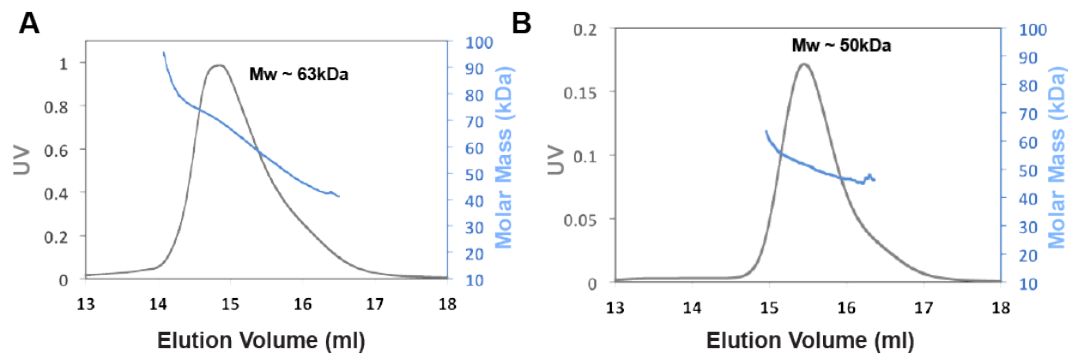


Figure 3-3 Concentration dependent oligomerization of Flil as studied by multi-angle light scattering (MALS). A chromatographic trace of the UV detector (blue) is shown with mass measurements of consecutive fractions of the chromatographic peak (black dots) superimposed. A. SEC-MALS profile for Flil with injected protein concentration=15 mg/ml; MALS data shows heterogeneous populations of Flil ranging from ~90 kDa to ~45 kDa with average molecular weight (Mw) of 63 kDa. B. SEC-MALS profile for Flil with injected concentration=1.5mg/ml. At lower concentration Flil appears to be more homogeneous ranging from ~55 kDa to ~45 kDa. Average molecular weight is 50 kDa, which corresponds to Flil monomer.

NMR studies. Consistent with literature studies⁸⁴, our light scattering (MALS) data shows that Flil exhibits concentration dependent oligomerization in solution (Figure 3-3). When Flil was injected in size-exclusion chromatography in-line with MALS at higher concentrations of Flil (15 mg/ml), the inhomogeneous MALS profile (Figure 3-3, A) indicates the presence of mixture of monomers and dimers in solution. When Flil was injected at low concentration (Figure 3-3, B), it

appeared to be monomer. The dimer to monomer dissociation constants of FliI had been determined using composition gradient multi-angle light scattering (CG-MALS) and is equal to 17 μM (Figure 3-4). Therefore FliI will stay as dimer in the concentration range used in all solution NMR studies.

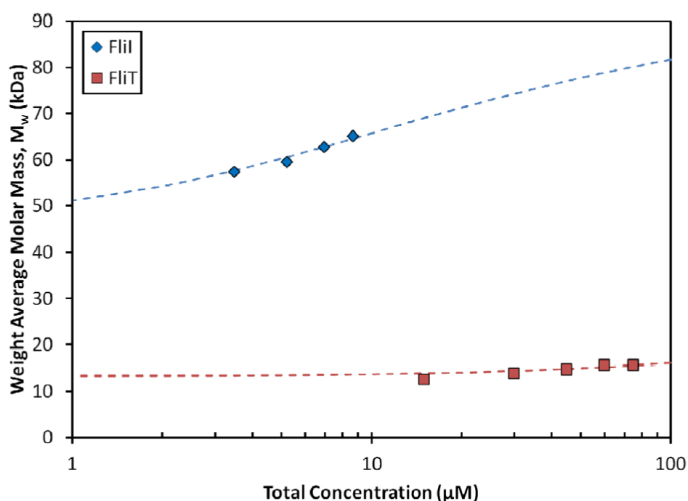


Figure 3-4 Self-association study of FliI and FliT by composition-gradient multi-angle laser light scattering (CG-MALS) using Calypso II composition gradient system (Wyatt Technology Corporation). The solid rectangles represent weight-average molar mass of FliI (blue) and FliT (red), respectively, at different concentrations of FliI and FliT. The dotted line represents fit to the CALYPSO software (Wyatt). The dissociation constant of dimer-monomer equilibrium of FliI and FliT are $\sim 17 \mu\text{M}$ and $\sim 300\text{-}600 \mu\text{M}$.

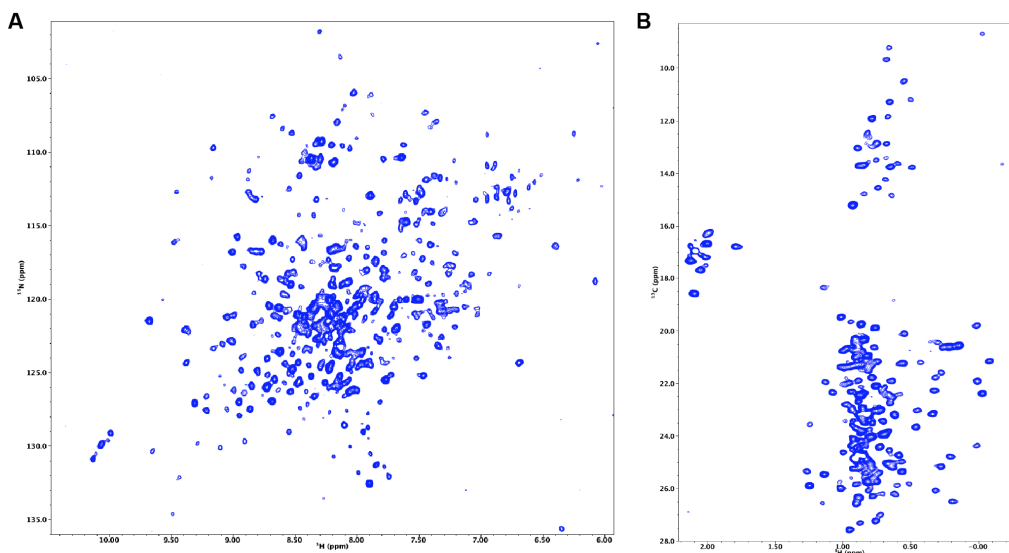


Figure 3-5 A. ^{15}N -TROSY B. ^{13}C -HMQC of U- $[^2\text{H}, ^{12}\text{C}, ^{15}\text{N}]$ Met(ϵ)-, Val(γ 1, γ 2)-, Leu(δ 1, δ 2)-, Ile(δ 1)- $[^{13}\text{CH}_3]$ FliI.

3.2.2 Chemical shift assignment of FliI

Owing to the fact that full length FliI forms a dimer (~100 kDa) in the concentration range used for solution NMR studies, full length FliI gave decent quality of ^{15}N -TROSY spectra (with significantly large number of transients) to carry out necessary protein interaction studies (Figure 3-5, A). Due to more favorable relaxation properties of methyl groups, ^{13}C -HMQC of U- $[^2\text{H}, ^{12}\text{C}, ^{15}\text{N}]$, Ala(β)-, Met(ϵ)-, Val(γ 1, γ 2)-, Leu(δ 1, δ 2)-, Ile(δ 1)- $[^{13}\text{CH}_3]$ of FliI yielded higher quality spectrum compared to the ^{15}N -TROSY (Figure 3-5, B). The ^{13}C -HMQC spectra of FliI was significantly improved when alanine labeling was not included in the NMR sample. Deletion of the N-terminal eighteen residues in FliI(Δ 18) drastically improved the ^{15}N -TROSY quality (Figure 3-6, A). The crystal structure

of FliI consists of three well-folded domains⁸¹. For NMR resonance assignment of FliI, two separate constructs of FliI were made, i) FliI(18-100), consists of N-terminal β -barrel and ii) FliI(105-456), consisting of FliI ATPase and C-terminal

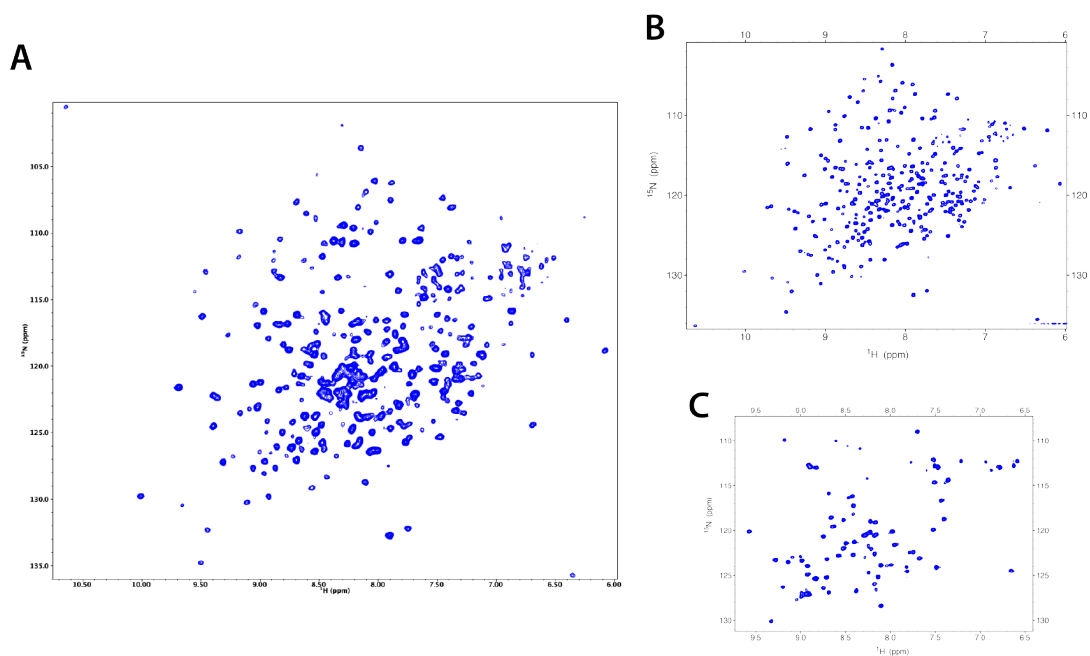


Figure 3-6 A. ¹⁵N-TROSY of U-[²H, ¹⁵N] FliI(18-456). B ¹⁵N-TROSY of U-[²H, ¹⁵N] FliI(104-456) C. ¹⁵N-HSQC of U-[¹⁵N, ¹³C] FliI(18-100).

domain. Both the constructs gave well-dispersed ¹⁵N-HSQC spectra characteristic of well-folded proteins (Figure 3-6, B and C). Most of the cross-peaks in the ¹⁵N-HSQC of both FliI(18-100) and FliI(105-456) correlates well with the ¹⁵N-HSQC of full length FliI. Thus, most of the resonance assignment of both the FliI constructs can be combined and transferred onto the ¹⁵N-HSQC of full-length FliI spectrum. Nevertheless, the resonance assignment of full length FliI

will not be possible because of poor spectral quality due to its larger size (dimer or higher oligomers at NMR concentration range). Therefore the NMR resonance assignment of FliI was carried out separately using FliI(18-100) and FliI(105-456).

3.2.2.1 Chemical shift assignment of FliI(105-456)

Although FliI(105-456) gave well-dispersed ^{15}N -TROSY for uniformly ^{15}N labeled protonated and deuterated sample, $\text{U}-[{}^2\text{H}, {}^{13}\text{C}, {}^{15}\text{N}]$ sample was used for sequential resonance assignment of FliI(105-456) owing to its large size (~37 kDa). The sequential assignment of ${}^1\text{HN}$, ${}^{15}\text{N}$, ${}^{13}\text{C}$, ${}^{13}\text{C}_\alpha$ and ${}^{13}\text{C}_\beta$ nuclei was performed with 3D TROSY-based deuterium decoupled triple-resonance 3D versions of HNCO, HN(CA)CO, HNCA, HN(CO)CA, HNCACB and HN(CO)CACB.

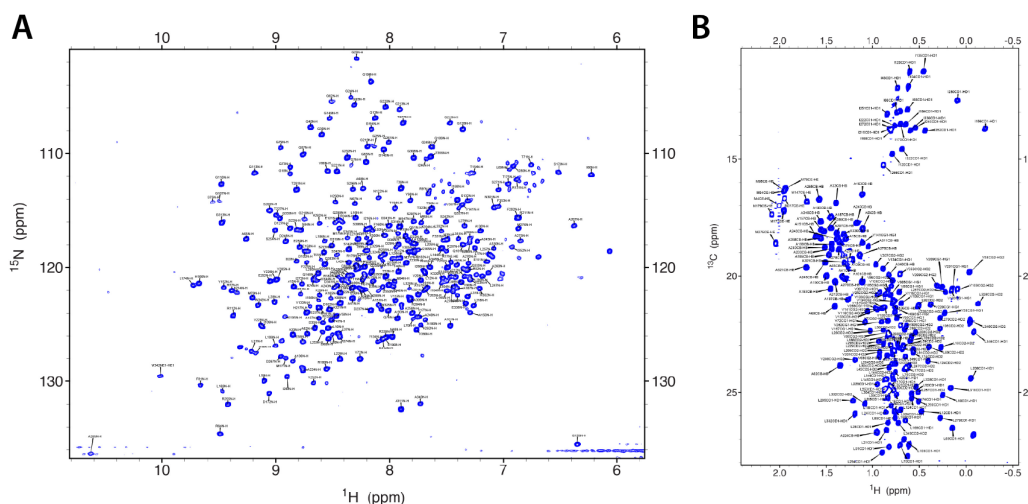


Figure 3-7 A. ^{15}N -TROSY B. ^{13}C -HMQC of $\text{U}-[{}^2\text{H}, {}^{12}\text{C}, {}^{15}\text{N}]$, Ala-, Met-, Val(γ_1, γ_2)-, Leu(δ_1, δ_2)-, Ile(δ_1)- $[{}^{13}\text{CH}_3]$ FliI(105-456) showing backbone and side-chain resonance assignment.

^{15}N -NOESY-TROSY, were recorded to verify the backbone resonance assignments using connectivities information available from the crystal structure of Flii(18-456). Sufficiently long, 300-500 ms, mixing time was typically used for all the NOESY experiments. This is typical when working with perdeuterated proteins. For U- $[\text{}^2\text{H}, \text{}^{15}\text{N}]$ labeled sample, a shorter (80-120 ms) was used to prevent the formation of spin diffusion of crosspeaks. Flii(105-456) gave excellent quality of triple resonances experiments and that allowed to carry out sequential backbone assignment. More than 95% resonance assignment was achieved for Flii(105-456). For side-chain assignment, U- $[\text{}^2\text{H}, \text{}^{12}\text{C}, \text{}^{15}\text{N}]$, Ala(β)-, Met(ϵ)-, Val(γ_1, γ_2)-, Leu(δ_1, δ_2)-, Ile(δ_1)- $[\text{}^{13}\text{CH}_3]$ labeled sample of Flii(105-456) was used to record a series of 3D NOESY experiments, ^{13}C -NOESY-HMQC, ^{13}C -HMQC-NOESY-HMQC, ^{15}N -NOESY-TROSY etc. 300 ms mixing time was used for all the NOESY experiments. All the resonance assignments of the methyl groups were performed using methyl-methyl, methyl-NH, methyl-aromatic, aromatic-aromatic NOEs combined with the distances from crystal structure of Flii. More than 90% of the labeled methyls in Flii(105-456) were assigned. Figure 3-7 (A and B) illustrates ^{15}N -TROSY and ^{13}C -HMQC of Flii(105-456) with backbone and side-chain resonance assignment of methyl residues.

3.2.2.2 Chemical shift assignment of Flii(18-100)

Due to smaller size of Flii(18-100), (~8.9 kDa), U- $[\text{}^{13}\text{C}, \text{}^{15}\text{N}]$ sample was used for the backbone and side-chain assignment of Flii(18-100). Similar to assignment strategy of Flii(105-456), standard 3D spectra of HNCO, HN(CA)CO, HNCA, HN(CO)CA, HNCACB, HN(CO)CACB were recorded and analyzed for the

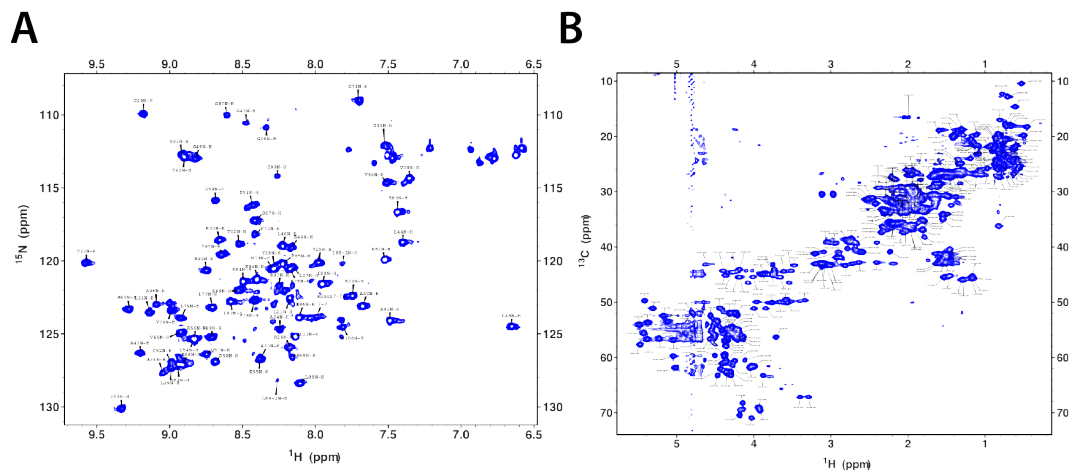


Figure 3-8 A. ^{15}N -HSQC of FliI(18-100) with backbone resonance assignment. B. ^{13}C -HSQC of FliI(18-100) with side-chain assignment.

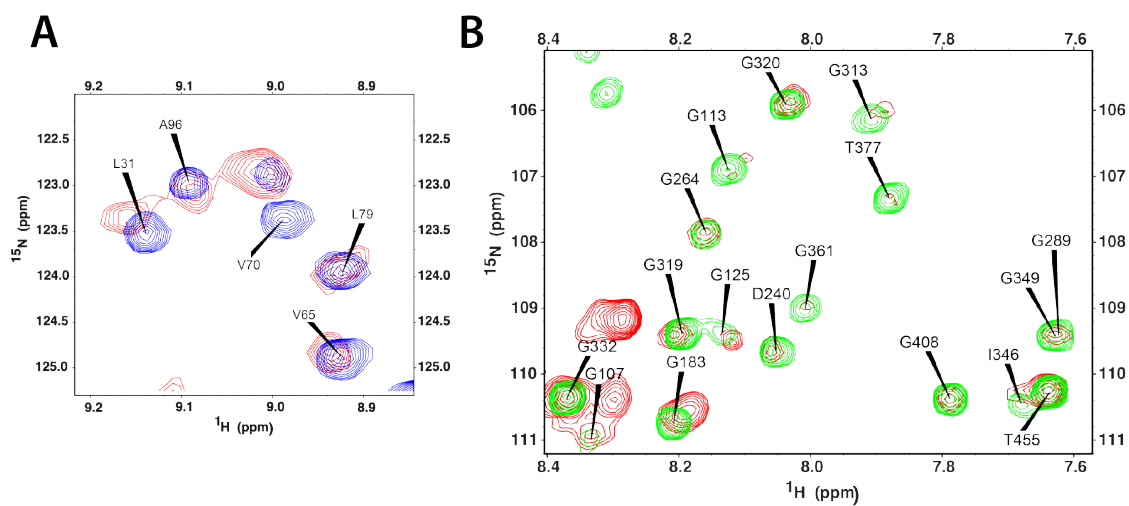


Figure 3-9 Overlay of expanded region of ^{15}N HSQC of FliI with A. FliI(18-100) and B. FliI(104-456).

sequential assignment of ^1HN , ^{15}N , $^{13}\text{C}'$, $^{13}\text{C}_\alpha$ and $^{13}\text{C}_\beta$. 3D spectra of HN(CCO)NH, C(CO)NH, HCCH-TOCSY and NOESY-HSQC spectra were used to assign side-chain chemical shift of Flil(18-100). More than 95% of backbone and side-chain resonance assignment of Flil(18-100) was achieved.

3.3 Discussion.

Flil is the central molecule in the flagellar export process⁴. Interactions of Flil with export gate proteins as well as export chaperones and chaperone-substrate complexes are crucial for export process^{4,84}. The resonance assignment of Flil is essential to study the mechanisms of the flagellar export process using solution NMR. More than 95% of the backbone and side-chain cross-peaks of Flil(105-456) and Flil(18-100) were assigned. In case of Flil(105-456), the N-²Hs in the core of the rossmand fold were very slow to exchange back into N-H's. A month old sample of Flil(105-456) showed many extra peaks in the ^{15}N -TROSY. Most of the assignment can be mapped into the Flil spectra (Figure 3-9). The extent of transferred assignment to full length Flil is sufficient to carry out solution NMR studies with other components of flagellar export process.

Chapter 4 : Chemical shift assignment of FliT

4.1 Introduction

FliT is the flagellar export chaperone for cap-forming protein FliD^{109,111}. Other than preventing premature aggregation of FliD in the cytoplasm, FliT also interacts with the soluble components of export apparatus, FliI and FliJ^{95,129}. FliT binds to FliD₂C₂ complex preventing it from the activation of the class 2

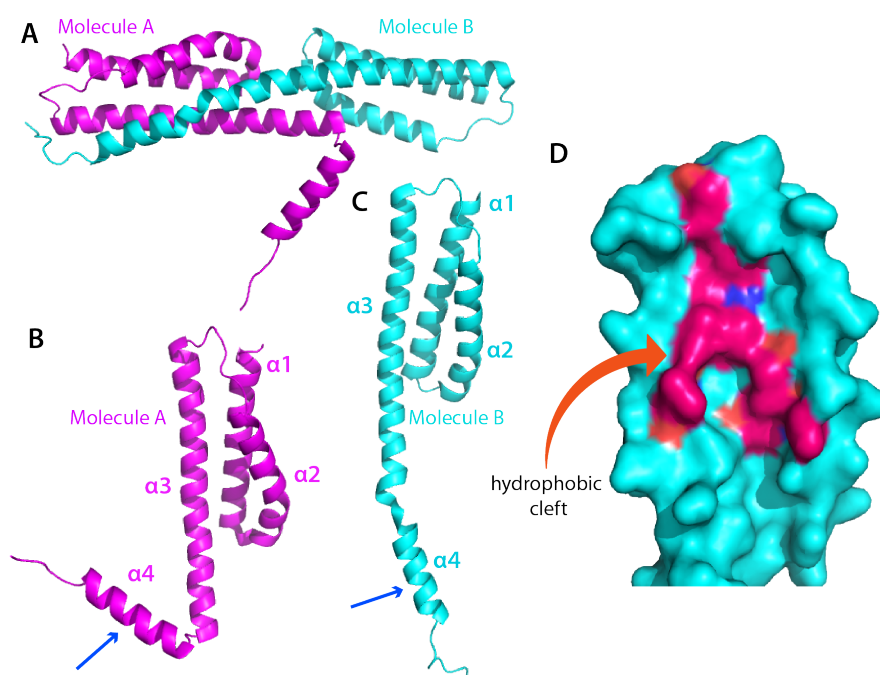


Figure 4-1 The crystal structure of FliT. A. Crystal structure of FliT dimer. The molecule A and molecule B of FliT are shown in magenta and cyan respectively. B and C show the molecule A and molecule B of FliT separately. The $\alpha 1$ -, $\alpha 2$ -, $\alpha 3$ - and $\alpha 4$ -helix are labeled in B and C. The flexible $\alpha 4$ -helix in B is indicated in blue arrow. D. The hydrophobic cleft of FliT¹¹².

promoters¹²³. Thus, in addition to acting as export chaperone for FliD, FliT plays critical role in fine-tuning the flagellar assembly process. FliT is a 13.7 kDa soluble proteins composed of 122 residues. It forms weak dimer in solution¹¹². Oligomerization of FliT has been tested at different pH and ionic strengths. Neither of them was found to influence the monomer-dimer equilibrium of FliT¹¹². The crystal structure of FliT consists of four α -helices (Figure 4-1) ¹¹². The asymmetric unit of the crystal contains two FliT molecules related by pseudo two-fold local symmetry. The anti-parallel bundle of α 1, α 2, α 3 helices form the core of the molecule. Helices α 2 and α 3 along with Phe-7 and Trp-11 of α 1 helix form a hydrophobic cleft (Figure 4-1, D). The conformation of the amphipathic α 4 helix is different in the two FliT molecules indicating that it has a flexible conformation in solution (Figure 4-1, B and C). The α 4 helix of one molecule of FliT binds to the hydrophobic cleft of another molecule to form FliT dimer (Figure 4-1, A). The anti-parallel four helical bundle of FliT is similar to other reported crystal structure of flagellar export chaperone like FliJ and FlgN¹¹³.

4.2 Results

4.2.1 Biophysical characterization of FliT

FliT was reported to form a weak dimer in solution in contrast to other flagellar and T3SS chaperones that formed stable dimers in solution¹¹². Light scattering in line with size-exclusion chromatography (SEC-MALS) at injected concentration of 10.96 mg/ml (0.8 mM) of FliT gave a molecular mass of 19 kDa (**Figure 4-2**). Thus, consistent with the literature¹¹², FliT formed a mixture of monomers and dimers in solution. The dimer to monomer dissociation constant of FliT from

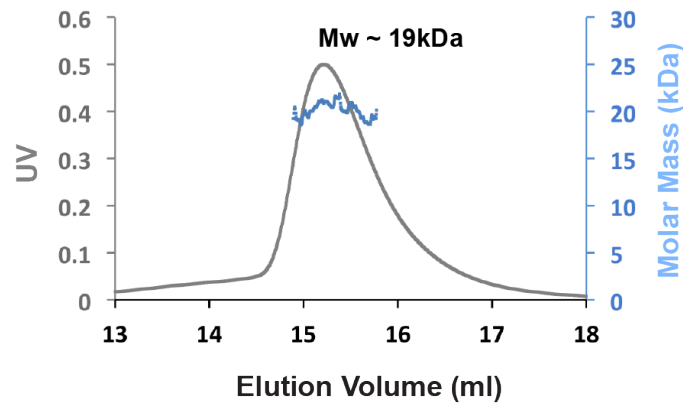


Figure 4-2 Native mass determination of FliT using MALS. A chromatographic trace of the UN detector (grey) is shown with mass measurements of consecutive fractions of the chromatographic peak (blue dots) superimposed. Injected protein concentration of FliT = 10.96 mg/ml; average molecular weight of FliT ~ 19 kDa.

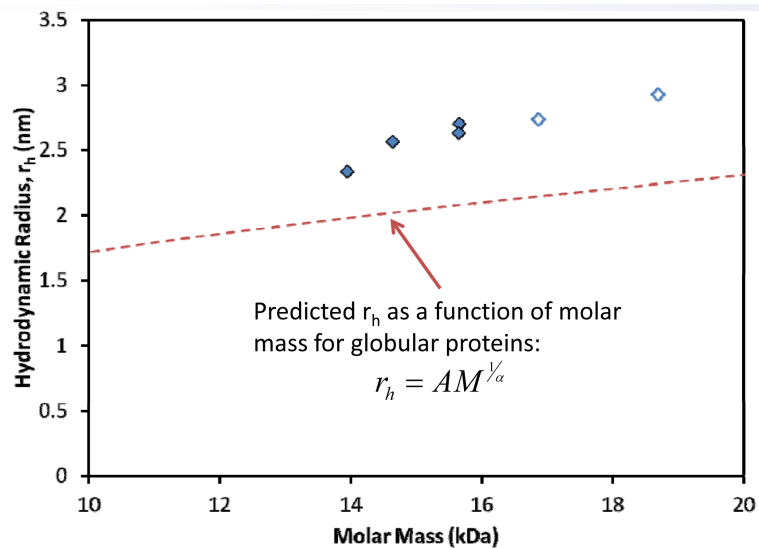


Figure 4-3 The hydrodynamic radius of FliT at different molar mass. The solid rectangle shows the hydrodynamic radius of FliT. The dotted red line indicates

the predicted hydrodynamic radius of a globular protein with same molar mass as FliT.

CG-MALS (Figure 3-4) was 300-600 μM , which was in accordance with the monomer to dimer self-association of 3,100 L/mol, from sedimentation equilibrium analysis¹¹². The hydrodynamic radius of FliT, measured using MALS, was larger than the expected molecular weight of FliT indicating that FliT adopts an elongated conformation in solution (Figure 4-3). The measured hydrodynamic radius of FliT is consistent with a globular protein of molecular weight \sim 20-34 kDa. Therefore although FliT appears as dimer in SEC, which separates protein molecules on the basis of hydrodynamic radius, FliT actually forms a mixture of monomer and dimer in solution. In addition to being difficult to measure precisely, the 300-600 μM K_D range for FliT falls within the concentration range typically used for NMR experiments. This causes exchange dynamic process that negatively impact data quality and present important challenges.

4.2.2 Attempts to assign backbone resonances of FliT

The U-¹⁵N FliT gave poor quality ¹⁵N-HSQC spectra (Figure 4-4, A). Several conditions were tried to improve ¹⁵N-HSQC quality of FliT. The ¹⁵N-HSQC of FliT were recorded at different pHs (pH=7.0, pH=7.5 and pH=8.0), at lower and higher salt concentrations as well as at three different temperatures (25 °C, 32 °C and 37 °C) (Table 4-1). None of these conditions improved the quality of ¹⁵N-

HSQC spectra. Therefore, conformational heterogeneity might be the reason for poor quality spectra. The crystal structure of FliT indicates that the C-terminal $\alpha 4$

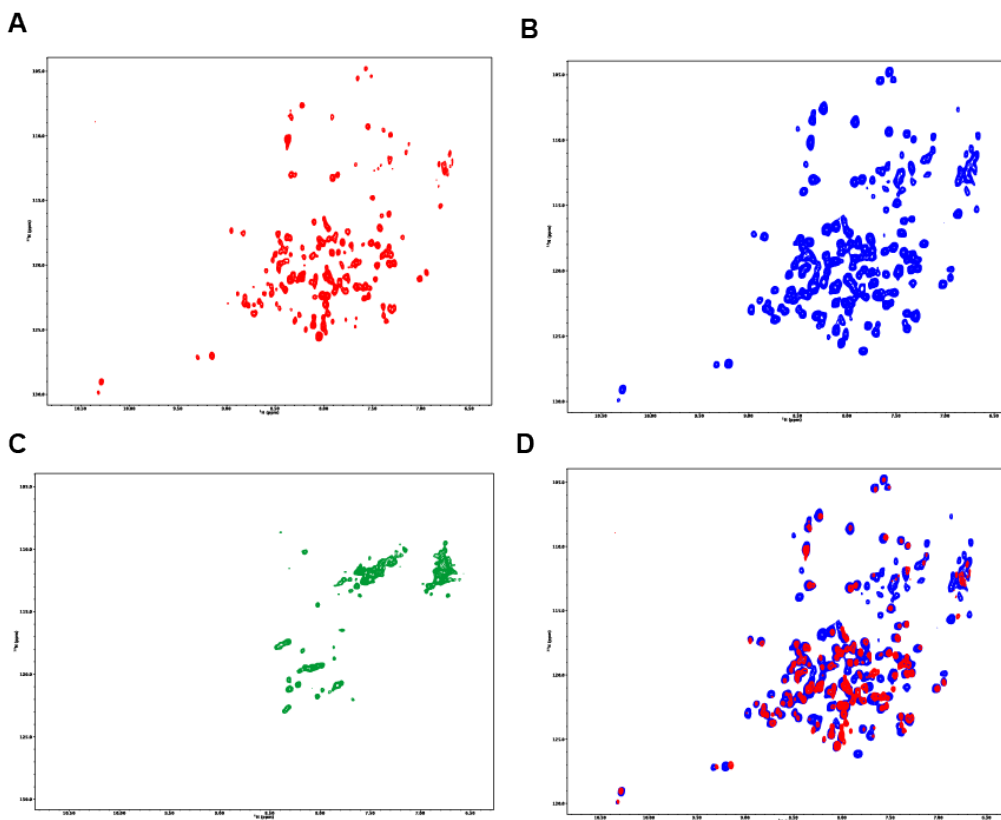


Figure 4-4 A. ^{15}N -HSQC of U- ^{15}N FliT B. ^{15}N -HSQC of U- $[^1\text{H}, ^{15}\text{N}]$ FliT C. ^{15}N -HSQC of U- ^{15}N FliT(1-97). D. Superposition of ^{15}N -HSQC of U- ^{15}N FliT (red) with U- $[^2\text{H}, ^{15}\text{N}]$ FliT (blue).

helix is dynamic in solution and the last ten residues at the C-terminal are unstructured. Therefore, in order to improve the ^{15}N -HSQC-spectrum quality, two deletion constructs were made: i. one with FliT(1-95) gave very poor ^{15}N -HSQC typical of aggregation in solution(Figure 4-4, C). deletion of unstructured last ten

residues, FliT(1-112) ii. deletion of C-terminal α 4 helix, FliT(1-95). The ^{15}N -HSQC quality didn't not improve for FliT(1-112).

Table 4-1 Summary of ^{15}N -HSQC spectra quality of FliT at different conditions.

Conditions	Results
Temperature : 25C, 32C, 37C	^{15}N HSQC improves at 32C but protein precipitates at 32C, 37C.
pH : 6.0 , 7.0, 8.0	No significant improvement over WT FliT.
Salt : 100mM KCl, 400mM KCl	No improvement WT FliT.
TFE : 5 % TFE ; protein precipitates with high % of TFE	No improvement WT FliT.

Table 4-2 Summary of ^{15}N -HSQC spectra quality of different FliT constructs.

FliT Construct	Quality of NMR spectra
FliT(1-97)	^{15}N HSQC spectrum looks like of aggregate.
FliT(1-112)	No improvement in ^{15}N HSQC spectrum.
FliTG94P	No significant improvement. But less heterogeneity in ^{15}N HSQC spectrum.
FliTS96P	No significant improvement. But less heterogeneity in ^{15}N HSQC spectrum.
FliTG94PS96P	Improved ^{15}N HSQC spectrum. Less heterogeneity in ^{15}N HSQC spectrum compared to G94P or S96P.
FliTG55P	Unstable protein.
FliTT52P	No improvement in ^{15}N HSQC spectrum.
FliTG94A	No improvement in ^{15}N HSQC spectrum. But less heterogeneity in in ^{15}N HSQC spectrum.
FliTG94AQ95K	Improved ^{15}N HSQC spectrum. Less heterogeneity in ^{15}N HSQC spectrum compared to G94A.
FliTG94AQ95R	Improved ^{15}N HSQC spectrum. Less heterogeneity in ^{15}N HSQC spectrum compared to G94A.

The exposed hydrophobic cleft, which is otherwise covered by the C-terminal $\alpha 4$ helix, could be the reason for aggregation. Deuteration of FliT significantly improved the ^{15}N -HSQC of FliT (Figure 4-4, B). The U- $[\text{}^2\text{H}, \text{}^{13}\text{C}, \text{}^{15}\text{N}]$ sample of FliT gave poor quality of triple resonance experiments. Several attempts were made to improve the triple resonance experiments of FliT. As FliT has a tendency to aggregate at higher concentration, 2D HNC0 planes of U- $[\text{}^{13}\text{C}, \text{}^{15}\text{N}]$ of FliT were

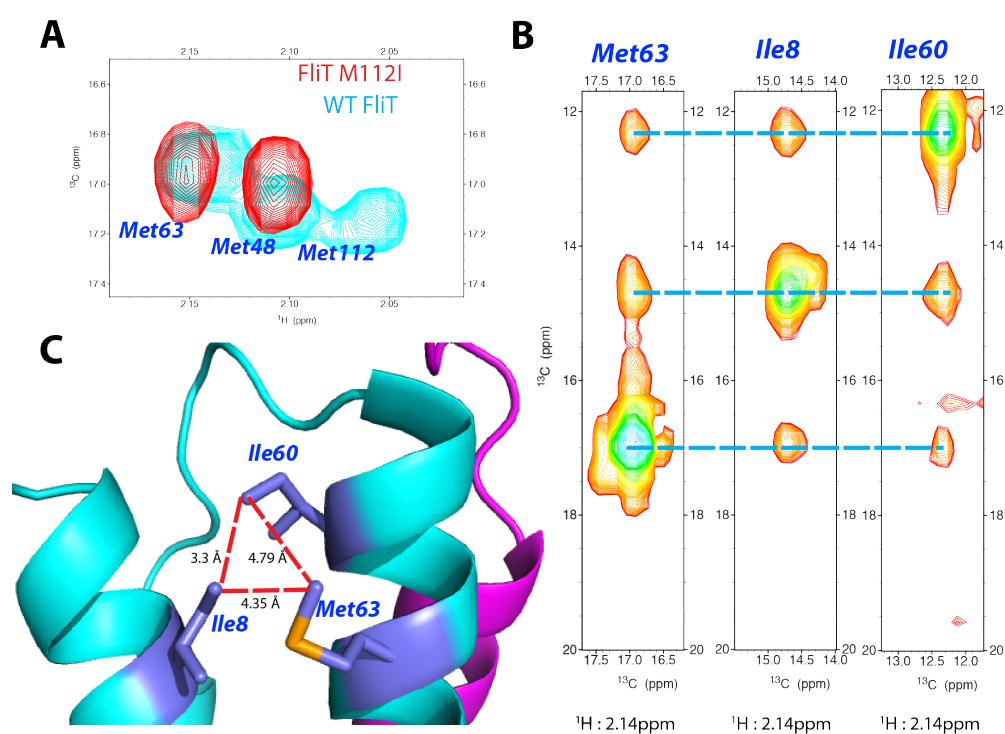


Figure 4-5 Assignment strategy of the resonance assignment of methyl groups of FliT. A. Superimposition of ^{13}C -HMQC of WT FliT (cyan) and FliTM112I (red). C. Crystal structure of FliT (PDB ID: 3A7M) showing close proximity of Ile8, Ile60 and Met63. D. ^{13}C -HMQC-NOESY-HMQC strips of FliTG94PS96P for Met63, Ile8 and Ile60.

recorded at different concentrations. Similar 2D HNCQ spectra were obtained at all concentration indicating that poor triple resonance spectra are not due to aggregation formation at higher concentration. Conformational heterogeneity of FliT caused by dynamic $\alpha 4$ helix might be the reason for poor triple resonance experiments. In an attempt to suppress the motion of $\alpha 4$ helix, Gly-94 and Ser-96 residues in the short loop connecting $\alpha 3$ and $\alpha 4$ helix, were mutated to proline. A marginal improvement in the ^{15}N -HSQC qualities of FliTG94P and FliTS96P mutants was noted. However, mutating both Gly94 and Ser96 to proline, results in less heterogeneity in the ^{15}N -HSQC spectra. The double mutant,

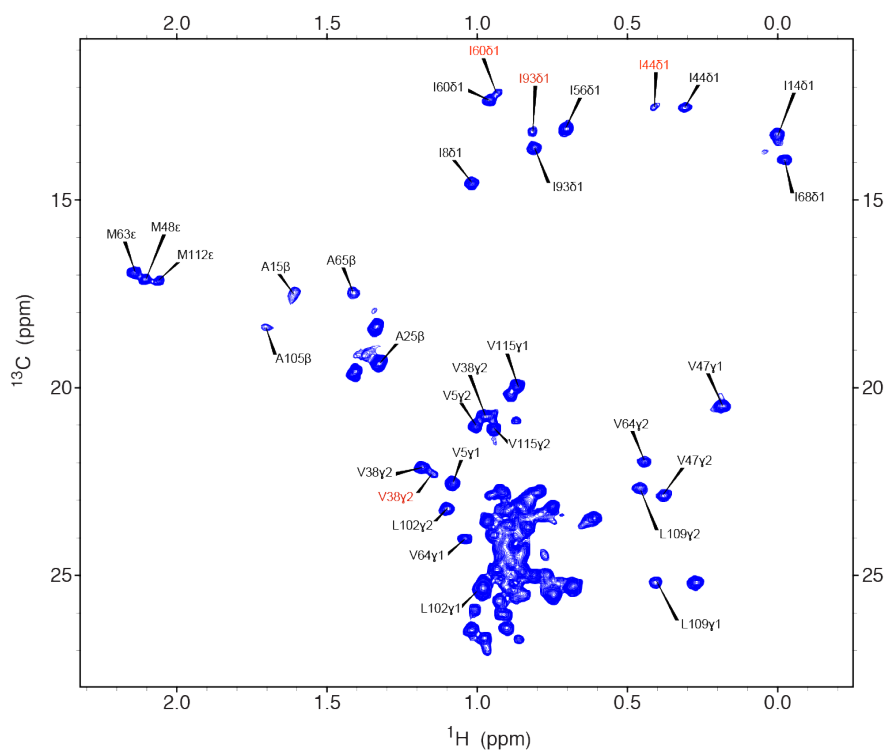


Figure 4-6 ^{13}C -HMQC of FliT showing partial side-chain assignment. The minor conformations are shown in red.

FliTG94PS96P didn't give decent quality of triple resonance spectra necessary for backbone assignment. Thr-55 and Gly-56 in the loop connecting $\alpha 2$ and $\alpha 3$ were also mutated to proline. FliTG55P was unstable at 25 °C. There was no improvement in the ^{15}N -HSQC of FliTT52P. In the crystal structure of FliT, in one molecule of the asymmetric FliT dimer, the $\alpha 4$ helix extends straight from the $\alpha 3$ helix and covers the hydrophobic cleft of the FliT molecule. In the second molecule of FliT, the $\alpha 4$ helix makes a sharp turn from the $\alpha 3$ helix (Figure 4-1, A). The short linker between $\alpha 3$ - and $\alpha 4$ -helix contains glycine and serine, which have low alpha helical propensities²³⁵. Therefore attempts were made to increase the α -helical propensity of the short linker so that the $\alpha 3$ helix continues to $\alpha 4$ helix, which will induce the formation of symmetric FliT dimer, by binding of $\alpha 4$ helix to the hydrophobic cleft of the other molecule. Alanine and glycine have the highest and lowest helical propensity, respectively, among all amino acids²³⁹. Gly94 was mutated to Ala to induce alpha helicity in the short linker between $\alpha 3$ and $\alpha 4$ helix. The ^{15}N -HSQC of FliTG94A showed less heterogeneity compared to WT FliT. The double mutants of FliT, FliTG94AQ95K and FliTG94AQ95R, gave further improvements over the WT FliT. The cross-peaks in the ^{15}N -HSQC spectra of both the double mutants correspond well to the WT FliT spectra. Due to high stability of FliTG94AQ95R at higher temperature, FliTG94AQ95R was chosen for triple resonance experiments. However, FliTG4AQ95R did not give good triple resonance experiments necessary for obtaining backbone resonance assignments. Therefore, backbone resonance assignment of FliT was not successful.

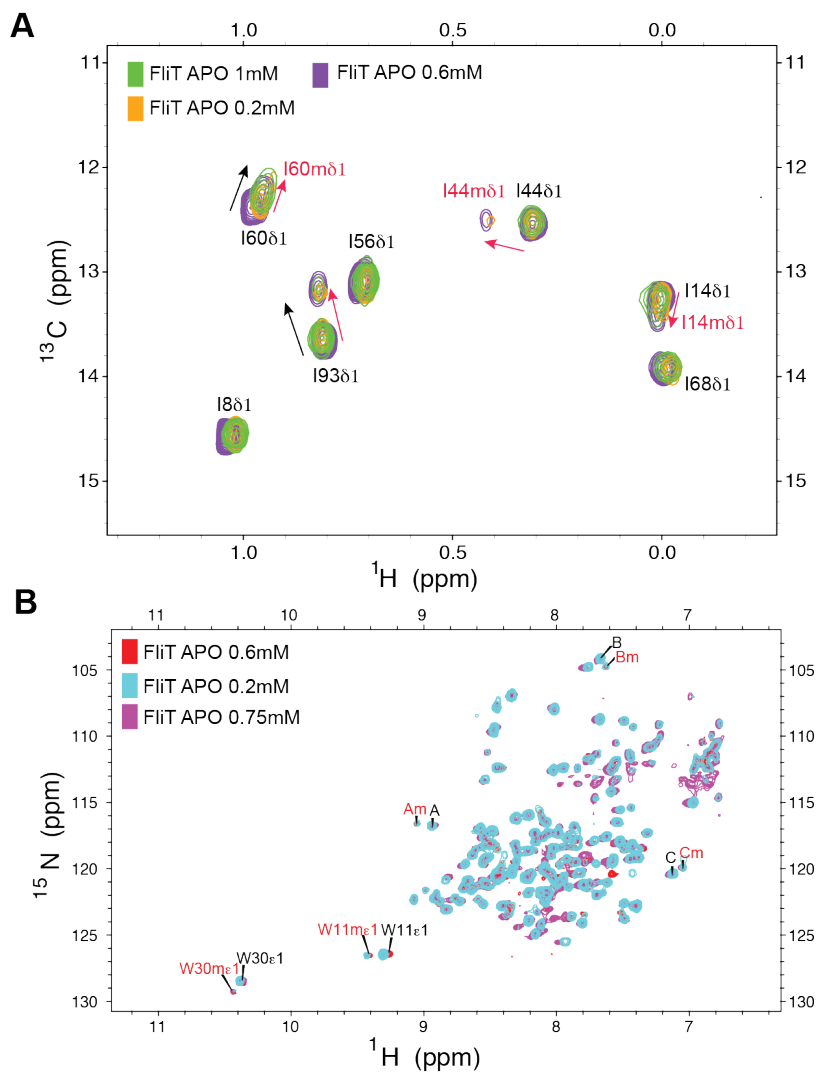


Figure 4-7 Dilution effects in the ^{15}N -TROSY and ^{13}C -HMQC of FliT. A. Superposition of ^{13}C -HMQC of FliT at 1 mM, 0.6 mM and 0.2 mM. Color code: 1 mM (green), 0.6 mM (magenta) and 0.2 mM (orange). B. Superposition of ^{15}N -TROSY of FliT at different concentrations, 0.75 mM, 0.6 mM and 0.2 mM. Color code: 0.75 mM (magenta), 0.6 mM (red) and 0.2 mM (cyan).

4.2.3 Partial side-chain assignment of FliT

The ^{13}C -HMQC of U- $[\text{}^2\text{H}, \text{}^{12}\text{C}, \text{}^{15}\text{N}]$, Ala(β)-, Met(ϵ)-, Val(γ 1, γ 2)-, Leu(δ 1, δ 2)-, Ile(δ 1)- $[\text{}^{13}\text{CH}_3]$ FliT showed well dispersed cross-peaks for Ile, Met, Ala and Val residues but the region for leu region was severely overlapped because of large numbers of leucine residues (Figure 4-6). Combination of site-directed mutagenesis along with a series of NOESY spectra has been utilized in the side-chain assignments of the methyl groups of large protein complexes using distance information from the crystal structure¹⁹⁵. A similar approach was used for side-chain assignment of FliT (Figure 4-5). WT FliT does not give good quality

Table 4-3 Table for intensity ratio of the major and minor conformations of Ile14, Ile44, Ile60 and Ile93 in the ^{13}C -HMQC of FliT.

Residue	Concentrations	Intensity of major conformer	Intensity of minor conformer	Intensity ratio of minor/major
Ile14	1mM	231066	86489	0.37430431
	0.6mM	4229432	1256840	0.2971652
	0.2mM	23492798	18640114	0.7934395 *
Ile44	1mM	231634	86489	0.37338646
	0.6mM	3409945	773446	0.22682067
	0.2mM	21198576	7776750	0.36685247
Ile60	1mM	238059	76606	0.32179418
	0.6mM	6280688	1254314	0.19970965
	0.2mM	30855838	7971648	0.25835137
Ile93	1mM	412754	72634	0.17597407
	0.6mM	7575960	1476828	0.19493609
	0.2mM	40345200	14517698	0.35983706

* No reliable peak heights can be measured for the minor conformations.

3D ^{13}C -HMQC-NOESY-HMQC and 3D NOESY-HMQC necessary to obtain full side-chain assignment. The double mutant of FliT, FliTG94PS96P gave improved quality of ^{13}C -HMQC-NOESY-HMQC spectra with good correlation with the Ile, Met, Ala and Val-regions of WT FliT. The ^{13}C -HMQC spectra of eight point mutations of FliT (M63I, I8L, I60L, A65V, V64I, L89I, L102I and L109I) were used for side-chain resonance assignment. By combined analysis of eight point mutations and the NOESY spectra of FliT and FliTG94PS96P, along with distance information from the FliT crystal structure, it was possible to assign almost all the Ile, Met, Val and Ala residues of FliT (Figure 4-6). However, except a few leucine residues, most of the leucine residues remained unassigned.

4.3 Discussion.

FliT gave poor quality ^{15}N -HSQC spectra, which did not improve under various pH, salt concentration and temperature. Deuteration of FliT improved the quality of ^{15}N -HSQC spectra but it did not give good quality triple resonance experiments. All the mutants and constructs of FliT, designed to improve triple resonance experiments, were unsuccessful. Thus, we were not successful to obtain backbone resonance assignment of FliT. The combined analysis of ^{13}C -HMQC-NOESY-HMQC spectra of WT FliT and FliTG94PS96P, site-directed mutagenesis and distance information from the crystal structure of FliT, allowed for a partial side-chain assignment of FliT. The ^{15}N -HSQC and ^{13}C -HMQC spectra of FliT show the presence of minor conformations. The conformational exchange between the major and minor conformations might be the reason for

Table 4-4 Table for intensity ratio of the major and minor conformations of in the ^{15}N -HSQC of FliT. Trp11 and Trp30 represent tryptophan side-chains. A, B and C represents three unassigned cross peaks in ^{15}N -HSQC of FliT that show two populations.

Residue	Concentrations	Intensity of major conformer	Intensity of minor conformer	Intensity ratio of minor/major
A	0.75mM	9662203	4801745	0.49696172
	0.6mM	1869113	1202770	0.64349774
	0.2mM	16865148	8385260	0.49719457
B	0.75mM	18760290	5184560	0.2763582
	0.6mM	3302438	1368023	0.41424638
	0.2mM	27216142	8472793	0.31131499
C	0.75mM	26744726	9029491	0.33761763
	0.6mM	5564220	2839651	0.51034125
	0.2mM	39023588	15450502	0.39592725
W11	0.75mM	46654096	6417328	0.13755122
	0.6mM	5496212	1313709	0.2390208
	0.2mM	63008244	12739231	0.20218356
W30	0.75mM	38201580	6589301	0.17248766
	0.6mM	6372390	885664	0.13898459
	0.2mM	28101732	4421172	0.15732738

the poor 3D spectra. As FliT forms a weak dimer in solution with K_D of ~ 300 - $600 \mu\text{M}$, the minor conformations of FliT might be due to dimeric populations. To understand the origin of minor conformations of FliT, ^{15}N -HSQC and ^{13}C -HMQC of spectra of FliT were recorded at different concentrations (Figure 4-7, A and B) and the relative intensity between major and minor conformations were calculated. The minor/major cross-peak intensity ratio ranges approximately 15-

40% (Table 4-3 and Table 4-4). No clear pattern was observed to indicate that weakly populated was originated from the dimeric species. Even ^{15}N -HSQC of FliT at 100 μM concentration showed two populations. Considering 300-600 μM dimer-monomer K_D of FliT, it is unlikely that monomeric and dimeric forms of FliT represents major and minor conformations. Many of the point mutations of FliT (G94P, S96P, G94PS96P, G94A, Q95K, Q95R, G94AQ95K and G94AQ95R) were designed to reduce the dynamic motion of $\alpha 4$ helix of FliT (Table 4-1). The

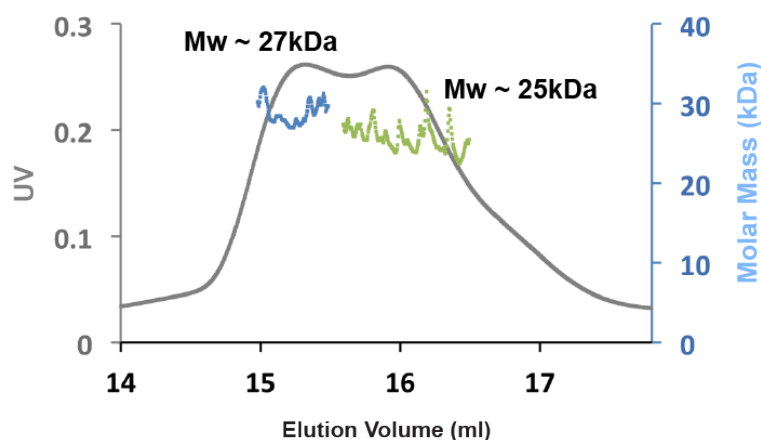


Figure 4-8 Native mass determination of GB1FliT using MALS. A chromatographic trace of the UN detector (grey) is shown with mass measurement of consecutive fractions of the chromatographic peak superimposed. Blue and green illustrates molar mass of two closely populated peaks of GB1FliT.

^{15}N -HSQC spectra of all the point mutants indicate reduced heterogeneity in a varying degree. Thus, the dynamic nature of the $\alpha 4$ helix of FliT might be the

origin of two conformers of FliT. The SEC-MALS of GB1-FliT showed two populations of monomeric GB1-FliT with molar mass of 25 kDa and 27 kDa, respectively (Figure 4-8). Therefore, it is possible that the $\alpha 4$ helix of FliT binds to its own hydrophobic cleft although it requires partial unfolding of the C-terminal end of $\alpha 3$ helix. In that case, the bound and the unbound form of the $\alpha 4$ helix with its own hydrophobic cleft leads to two conformations of FliT.

Chapter 5 : Interaction study between flagellar ATPase FliI and export chaperone FliT

5.1 Introduction

The interaction of the flagellar export chaperone and chaperone-export complex with the FliI ATPase complex is a crucial step in the targeting of the chaperone-substrate complex to the export gate¹²⁹. Although all flagellar chaperone-substrate complexes interact with FliI, only FliT is reported to interact with the

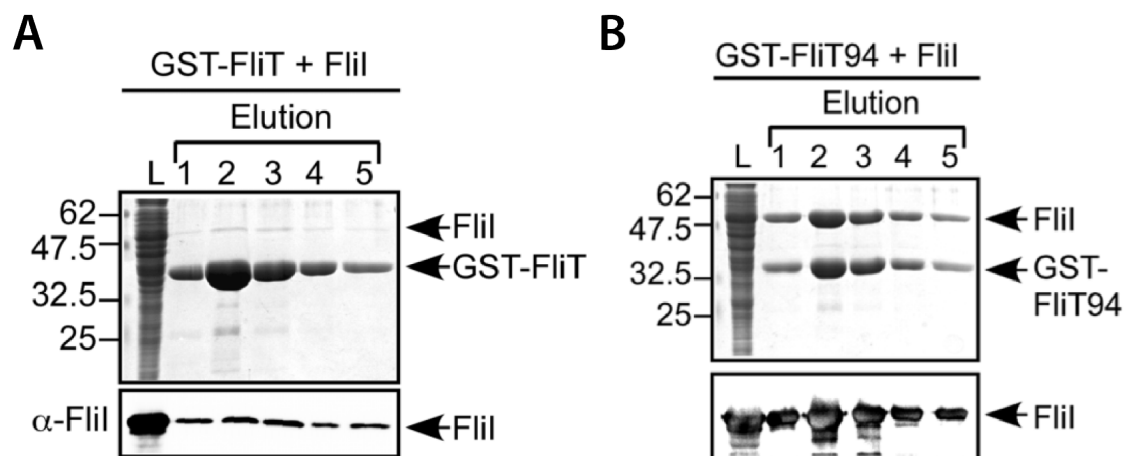


Figure 5-1 Interaction between FliI and FliT using pull down assay. A. Interaction between FliI and FliT. B. Interaction between FliI and FliT94¹²⁷.

ATPase FliI in its substrate-free state^{112,127}. Similar chaperone-ATPase interactions are known for homologous T3SS chaperones between CesT and EscN in EPEC, SicP and InvC, SrcA and SsaN in pathogenic *Salmonella*, and CdsN and Cpn0706, in *Chlamydomonas reinhardtii*^{236,130,237,238}. The interaction between CesT and EscN is proposed to facilitate the interaction between Tir, one

of the substrates of CesT, with EscN and its subsequent secretion²³⁶. There is limited understanding of the biological significance of such chaperone-ATPase interaction in the targeting of chaperone-substrate complex. The interactions between FliI and FliT, and the FliT-FliD complex have been studied using pull-down assays (Figure 5-1)¹²⁷. These studies show that FliI has two distinct FliT-binding sites¹²⁷. GST-FliT(1-94), lacking the C-terminal $\alpha 4$ helix, has higher binding affinity for FliI than GST-FliT (Figure 5-1). The $\alpha 4$ helix of FliT appears to control its interaction with FliI^{112,127}. GST-FliT(1-94) interacts with the extreme N-terminal residues of FliI (FliI_{EN}) with high affinity and with the C-terminal ATPase domain (FliI_{CAT}) with low affinity¹²⁷. The hydrophobic cleft in the FliT is proposed to interact with FliI^{112,127}. Although the interactions between FliI and FliT have been studied using pull-down assays, there is no biophysical characterization. We have characterized the interaction between FliI and FliT primarily using solution NMR along with other biophysical techniques to understand the role of FliI-FliT interaction in the flagellar type III export pathway.

5.2 Results

5.2.1 The extreme N-terminal residues of FliI interact with FliT.

Extensive NMR titrations were performed to characterize the interaction between FliI and FliT. NMR titration of U-[²H,¹³C,¹⁵N], Ala(β)-, Met(ϵ)-, Val($\gamma 1, \gamma 2$)-, Leu($\delta 1, \delta 2$)-, Ile($\delta 1$)-[¹³CH₃] FliT with natural abundance FliI showed interaction between FliT and FliI (Figure 5-2, B). The cross-peaks of ¹⁵N-TROSY and ¹³C-

HMQC of FliT disappear upon FliI binding indicating that the binding kinetics falls into the intermediate exchange regime. On the other hand, the quality of ^{15}N -

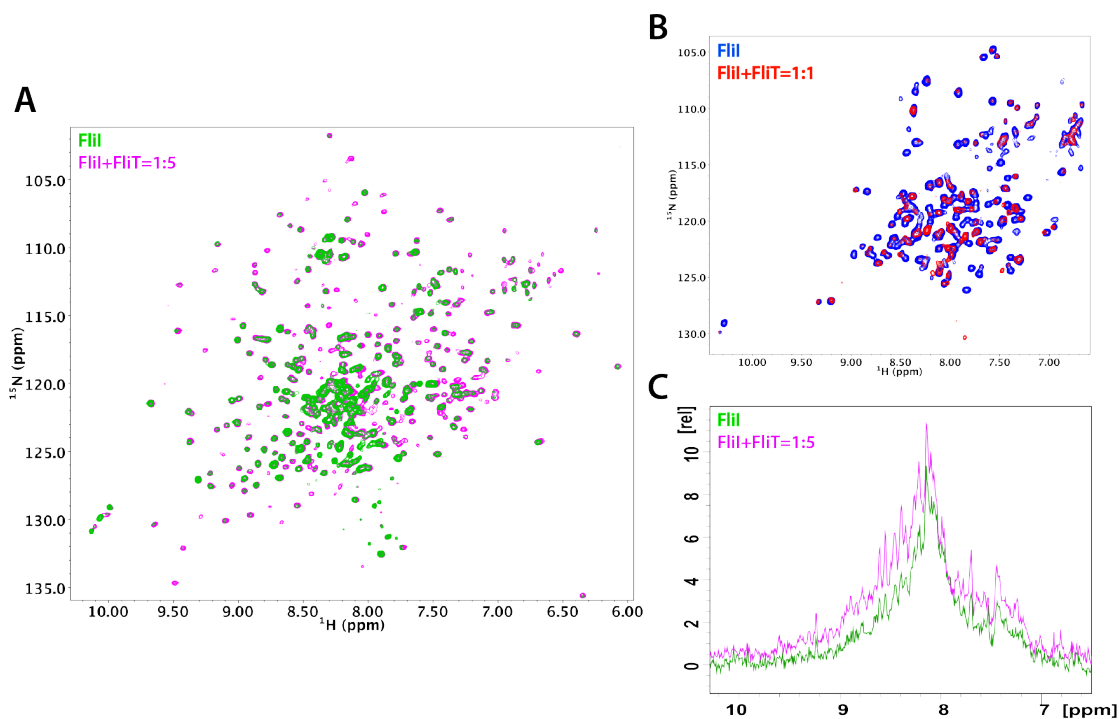


Figure 5-2 Interaction between FliI and FliT. A. ^{15}N -HSQC titration of U- $[\text{}^2\text{H}, \text{}^{12}\text{C}, \text{}^{15}\text{N}]$ Ala(β)-, Met(ϵ)-, Val(γ 1, γ 2)-, Leu(δ 1, δ 2)-, Ile(δ 1)- $[\text{}^{13}\text{CH}_3]$ FliI with natural abundance FliT. Color code: ^{15}N -TROSY of FliI, green; ^{15}N -TROSY of FliI+FliT=1:5, magenta; B. ^{15}N -HSQC titration between U- $[\text{}^2\text{H}, \text{}^{12}\text{C}, \text{}^{15}\text{N}]$ Ala(β)-, Met(ϵ)-, Val(γ 1, γ 2)-, Leu(δ 1, δ 2)-, Ile(δ 1)- $[\text{}^{13}\text{CH}_3]$ FliT and natural abundance FliI. Color code: ^{15}N -TROSY of FliI, blue; ^{15}N -TROSY of FliI+FliT=1:1, red; C. Overlay of first scan for the ^{15}N -HSQC titration of U- $[\text{}^2\text{H}, \text{}^{12}\text{C}, \text{}^{15}\text{N}]$ Ala(β)-, Met(ϵ)-, Val(γ 1, γ 2)-, Leu(δ 1, δ 2)-, Ile(δ 1)- $[\text{}^{13}\text{CH}_3]$ FliI with natural abundance FliT.

TROSY and ^{13}C -HMQC spectra of FliI improves when natural abundance FliT was titrated into U- $[\text{}^2\text{H}, \text{}^{12}\text{C}, \text{}^{15}\text{N}]$, Met(ϵ)-, Val(γ 1, γ 2)-, Leu(δ 1, δ 2)-, Ile(δ 1)- $[\text{}^{13}\text{CH}_3]$ FliI (Figure 5-2, A). However, no significant chemical shift perturbation was observed for both FliI and FliT. FliI is composed of three domains, N-terminal β -barrel domain, ATPase domain and C-terminal domain. There are \sim 25 flexible residues at the extreme N-terminal end of FliI. NMR titrations were performed with several constructs of FliI to identify its interacting domain. The ^{15}N -TROSY

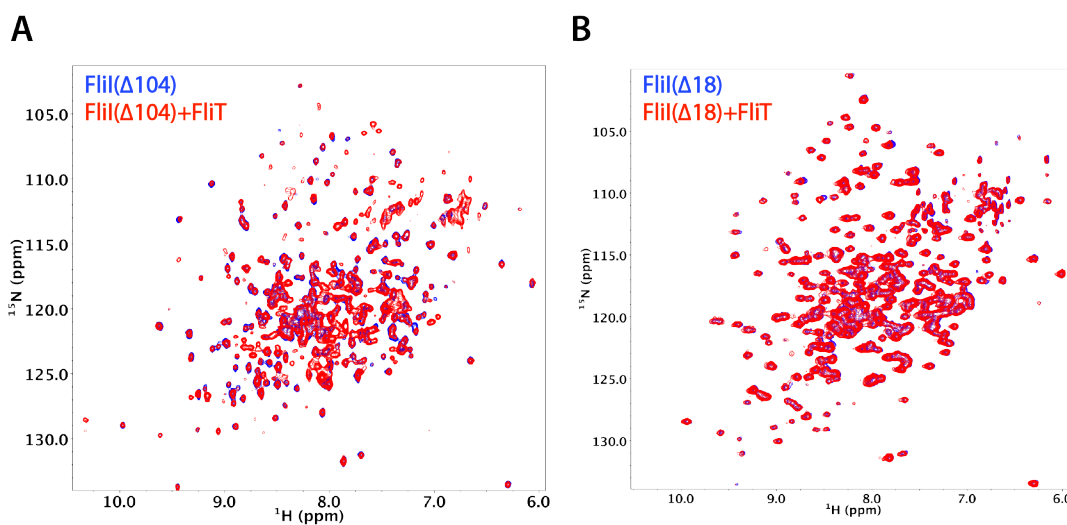


Figure 5-3 Interaction of N-terminal truncation construct of FliI with FliT. A. Overlay of ^{15}N -TROSY of U- ^{15}N FliI(Δ 104) with FliI(Δ 104) + FliT=1:1. Color code: ^{15}N -TROSY of U- ^{15}N FliI(Δ 104) in blue, ^{15}N -TROSY of U- ^{15}N FliI(Δ 104)+FliT=1:1 in red. B. Overlay of ^{15}N -TROSY of U- ^{15}N FliI(Δ 18) with FliI(Δ 18) + FliT=1:1. Color code: ^{15}N -TROSY of U- ^{15}N FliI(Δ 18) in blue, ^{15}N -TROSY of U- ^{15}N FliI(Δ 18)+FliT=1:1 in red.

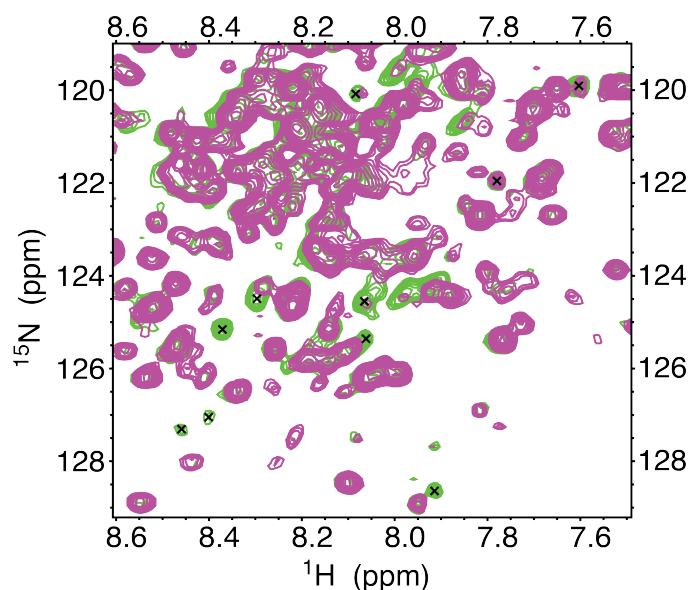


Figure 5-4 Overlay of ^{15}N -HSQC spectra of FliI (green) with FliI+FliT=1:5 (magenta). The cross-peaks of extreme N-terminal residue of FliI, which undergo line broadening upon FliT binding, are indicated by (x).

titration showed that two deletion constructs of FliI, FliI(18-456) (where the N-terminal 18 residues were deleted) and FliI(105-456) (where the entire β -barrel domain was deleted), did not interact with FliT (Figure 5-3). Therefore the N-terminal residues of FliI might play crucial role in the interaction with FliT. The cross-peaks of FliI corresponding to the extreme N-terminal of FliI were identified by overlaying the ^{15}N -TROSY spectrum of FliI with that of FliI(Δ 1-18). In Figure 5-4, all the cross-peaks corresponding to extreme N-terminals of FliI is marked by (x). All the cross-peaks corresponding to the extreme N-terminal residues of FliI were either disappeared or broadened upon FliT binding. Thus the extreme N-terminal residues of FliI interacted with FliT. However, the first 33 residues or 100

residues of FliI peptides were unstable in solution and it was not possible to any perform NMR titration between the first 33 residues or 100 residues of FliI peptides with FliT. In order to stabilize the N-terminal FliI peptides, first 33 residues of FliI peptide was fused with GB1 solubility tag. ^{15}N -HSQC of GB1FliI(1-33) showed weak, heterogeneous cross-peaks corresponding to FliI peptides (Figure 5-5, A). The NMR titration between U- ^{15}N GB1FliI(1-33) and

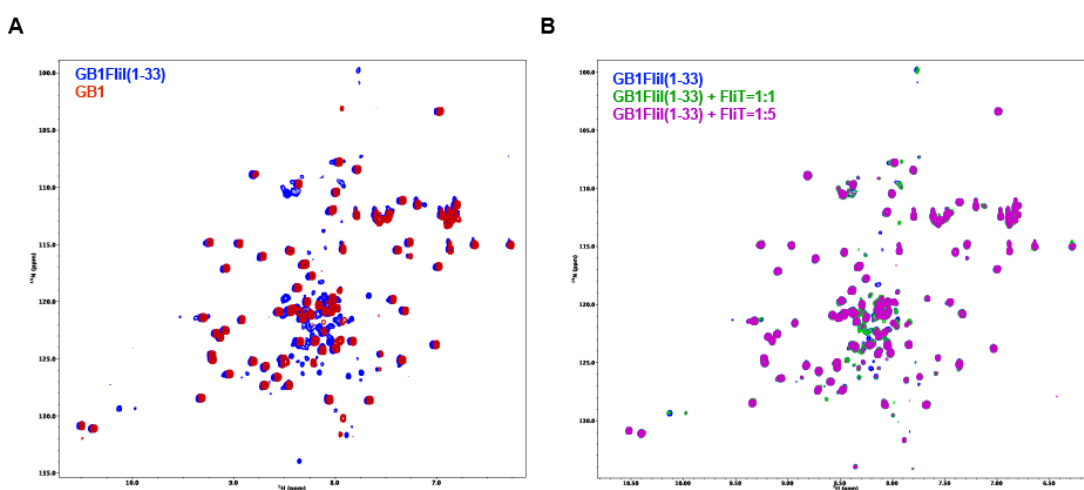


Figure 5-5 ^{15}N -HSQC titration of U- ^{15}N GB1FliI(1-33) with natural abundance FliT. A. Overlay of ^{15}N -HSQC of GB1FliI(1-33) with GB1. Color code: GB1FliI(1-33), blue ;GB1, red; B. ^{15}N -HSQC titration of U- ^{15}N GB1FliI(1-33) with natural abundance FliT. Color code: GB1FliI(1-33), blue ; GB1FliI(1-33) with FliT at molar ratio of 1:1, green ; GB1FliI(1-33) with FliT at molar ratio of 1:5, magenta.

natural abundance FliT showed interaction between GB1FliI(1-33) and FliT (Figure 5-5, B). However, due to weak and inhomogeneous cross-peaks of the

N-terminal FliI peptides, it was not possible to obtain any residues specific information. The $\alpha 4$ helix of FliT was proposed to regulate its interaction with binding partners^{112,127}. Attempts were made to study the interaction between FliT(1-95) with FliI using ¹⁵N-HSQC titration. Due to poor quality of ¹⁵N-HSQC of FliT(1-95), we were unable to study the interaction between FliT(1-95) with FliI.

The binding affinity and the stoichiometry of the interaction between FliI and FliT were determined using light scattering. A K_D value of 1-3 μM was obtained from CG-MALS studies. Furthermore, the CG-MALS studies showed that FliI interacts with FliT to form FliI-FliT complex with 1:1 stoichiometry. Besides, small amounts of higher order oligomeric complex of FliI and FliT (~1% mol/mol) were also

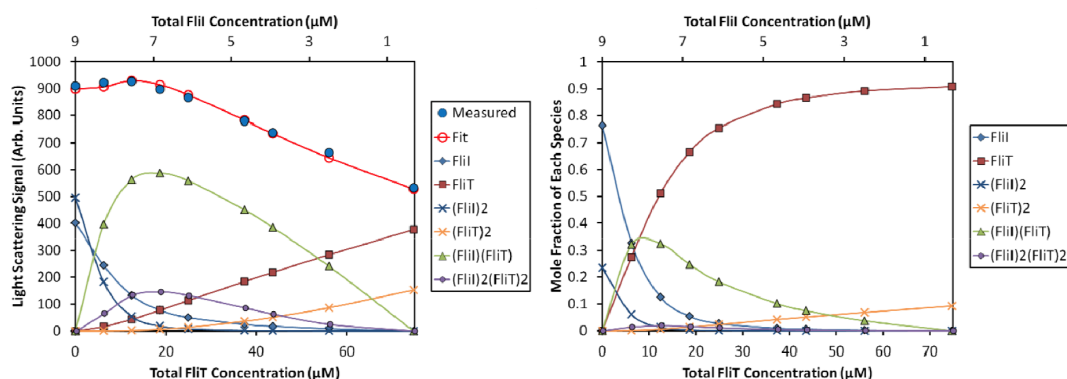


Figure 5-6 Interaction study between FliI and FliT using composition gradient multi-angle light scattering (CG-MALS). The left and the right diagrams show the total light scattering signal and the mole-fraction of each species for the FliI-FliT mixture at different concentrations. Majority of the interaction has 1:1 stoichiometry of FliI and FliT with $K_D \sim 1\text{-}3 \mu\text{M}$. Small amount of different higher order oligomer (~1% mol/mol) are also present. The higher order oligomers are

shown in the diagram as $(\text{Flil})_2(\text{FliT})_2$, but it may be combination of $(\text{Flil})(\text{FliT})_2$, $(\text{Flil})_2(\text{FliT})$ and $(\text{Flil})_2(\text{FliT})_2$.

identified (Figure 5-6). The dissociation constant obtained from our preliminary ITC data were consistent with K_D from light scattering studies. However, low heat of enthalpy along with precipitation during calorimetry reaction made it difficult for ITC studies. Optimization of conditions of ITC was required for further ITC studies. The formation of (1:1) Flil-FliT complex explained the improved spectral quality of Flil upon FliT binding. Considering $\sim 17 \mu\text{M}$ dissociation constant of Flil, it will remain dimer ($\sim 100 \text{ kDa}$) in solution in the concentration range used for solution NMR studies. Thus, monomerization of Flil on addition of FliT explains the enhanced spectral quality of Flil. On the other hand, addition of Flil to FliT results in larger protein complex leading to weakening and spectral broadening of cross-peaks. However, disappearance of interacting cross-peaks in both FliT and the extreme N-terminal residues of Flil indicate that Flil-FliT interaction falls into intermediate exchange regime.

5.2.2 FliT inhibits ATPase activity of Flil.

Oligomerization of Flil is coupled to its ATPase activity⁸⁴. The extreme N-terminal residues of Flil control its oligomerization⁸⁷. Flil($\Delta 1-7$) forms a monomer in solution even at higher concentration⁸⁷. Consequently Flil($\Delta 1-7$) shows diminished ATPase activity⁸⁷. As FliT interacts with the extreme N-terminal of Flil and keeps Flil in the monomeric form (Figure 5-4, Figure 5-6), FliT is expected to

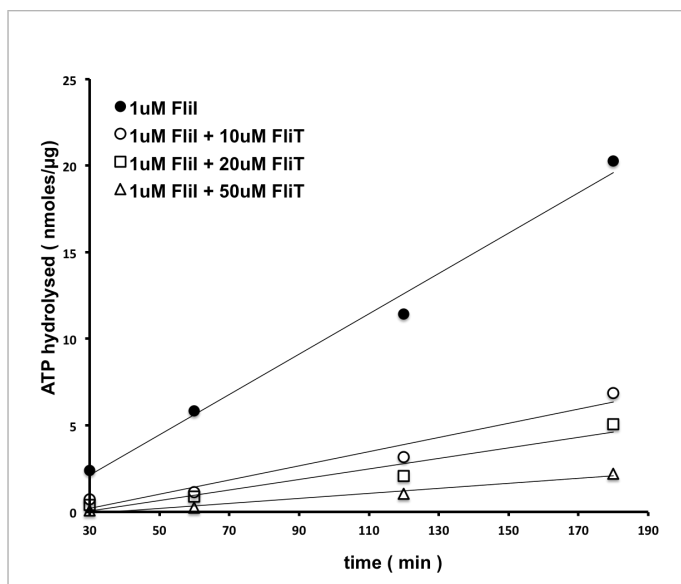


Figure 5-7 A. Inhibition of ATPase activity of FliI by FliIT. Measurement was carried out on FliI or mixture of FliI and FliIT at molar ratios of 1:10, 1:20, and 1:50.

inhibit the ATPase activity of FliI. It was reported in literature that GST-FliIT(1-94), which binds FliI with stronger affinity than FliIT, inhibits the ATPase activity of FliI¹²⁷. FliI has highest ATPase activity at pH=8.0⁸⁰. Thus all the ATPase activity measurements were performed at pH=8.0. Figure 5-7 shows the ATPase activity of FliI in the presence of different molar ratios of FliIT. As expected, the ATPase activity of FliI decreases gradually with increasing molar ratios of FliIT. Thus FliIT inhibits the ATPase activity of FliI. GST-FliIT was reported not to affect the ATPase activity of FliI¹²⁷. This could be due to the use of comparatively low concentrations of GST-FliIT.

5.3 Discussion

The interaction between FliI and FliT was characterized using solution NMR and light scattering. FliT interacts with the extreme N-terminal residues of FliI to form FliI-FliT complex with 1:1 stoichiometry. The extreme N-terminal residues of FliI are responsible for its oligomerization⁸⁷. The dimer to monomer dissociation constant of FliI (~17 μ M) suggests dimer population of FliI at the range of NMR concentrations used in solution NMR studies. Thus, FliT disrupts FliI dimer in solution by forming 1:1 FliI-FliT complex. Consistently, FliT inhibits the ATPase activity of FliI as the dimeric form of FliI is the minimal active unit. So far, FliH is known to inhibit the ATPase activity of FliI⁸⁸. FliH inhibits ATPase activity of FliI by keeping FliI in monomeric form⁸⁸. FliT is the only export chaperone known, in the flagellar export apparatus or the type III secretion system in general, which inhibits ATPase activity of FliI. However, the biological implication of such inhibition was not known. Based on our biophysical studies between FliI and FliT, we propose a model (Figure 5-9) for the interaction between FliI and FliT. FliI exhibits concentration dependent oligomerization in solution. It forms dimer or higher order oligomers by the interaction of the extreme N-terminal residues of FliI. FliT stays as weak dimer in solution. FliT disrupts the FliI dimer or higher order oligomers to form FliI-FliT complex. The structural characterization of FliI-FliT complex remains a challenge. The NMR titration between FliI and FliT does not exhibit sufficient chemical shift to map their binding interface. Moreover, the interaction between FliI and FliT fall into intermediate exchange regime. Thus the cross-peaks for the interacting residues are either disappears or weakens upon

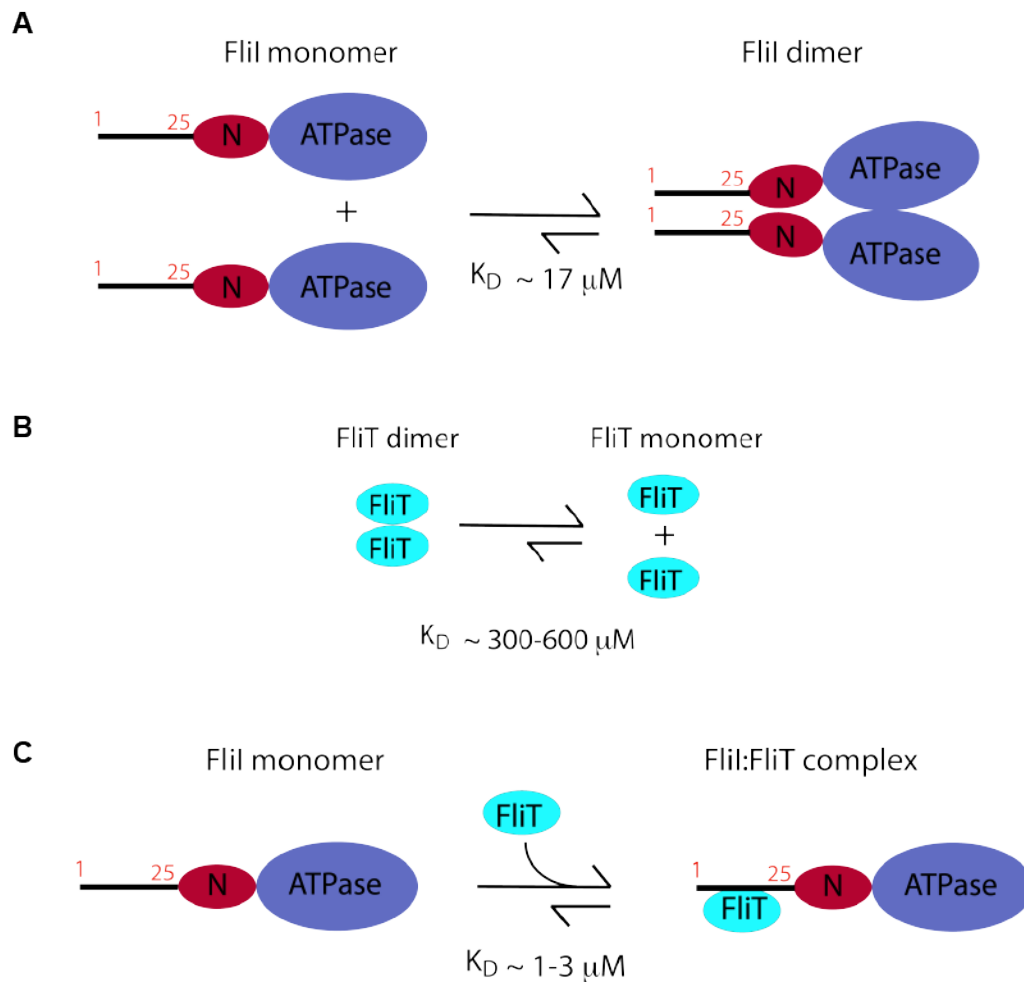


Figure 5-8 Schematic model for interaction between FliI and FliT. A. Monomer-dimer equilibrium of FliI B. Monomer-dimer equilibrium of FliT. C. Interaction between FliI and FliT. Color code: FliT dimer or monomer are shown in cyan; The extreme N-terminal of FliI is shown in black line, N-terminal β -barrel domain of FliI in red and the ATPase domain FliI in blue.

binding. Therefore, it was difficult to structurally characterize using conventional solution NMR methods. Attempts were made to titrate first 33 residues and 100

residues of FliI peptides to FliT. However, both first 33 residues and 100 residues of FliI peptides were unstable in solution. But due to weak and heterogeneous cross-peaks of the extreme N-terminal residues of FliI, residue specific information was not possible from the NMR titration between U-¹⁵N GB1FliI(1-33) and FliT.

Chapter 6 : Structural characterization of FliI-FliT complex

6.1 Introduction

There are several reports for the interaction between T3SS ATPases and chaperones, but there is no structure of chaperone-ATPase complex reported so far^{130,236,237,238}. The mode of interaction between FliI and FliT from *Salmonella* is different from chaperone-ATPase interactions in the homologous T3SS. FliT interacts strongly with the extreme N-terminal region of FliI and interacts weakly with the C-terminal ATPase domain. As both GST-FliT(1-94) and FliH bind to FliI_{EN}, the mode of binding of FliI_{EN} to FliH and GST-FliT(1-94) should be similar. Bioinformatic and biochemical study shows that FliI_{EN} has a tendency to form amphipathic α -helix upon interaction with FliH⁹⁰. Moreover, the interaction between FliH and FliI has similarities to the interaction between the δ -subunit of F₁-ATPase and the N-terminal α -helix of α -subunit of F₁-ATPase⁹⁰. Therefore FliI_{EN} is more likely to form α -helix when it binds to the hydrophobic cleft of FliT. We have structurally characterized the FliI-FliT complex structure using solution NMR techniques.

6.2 Results

6.2.1 Design and optimization of fusion construct

The NMR titrations between FliI and FliT as well as light scattering studies show that the extreme N-terminal residues of FliI with FliT. Unfortunately, the interaction between FliI and FliT fall in the intermediate exchange regime. Therefore, most of the interacting residues of FliI and FliT were either

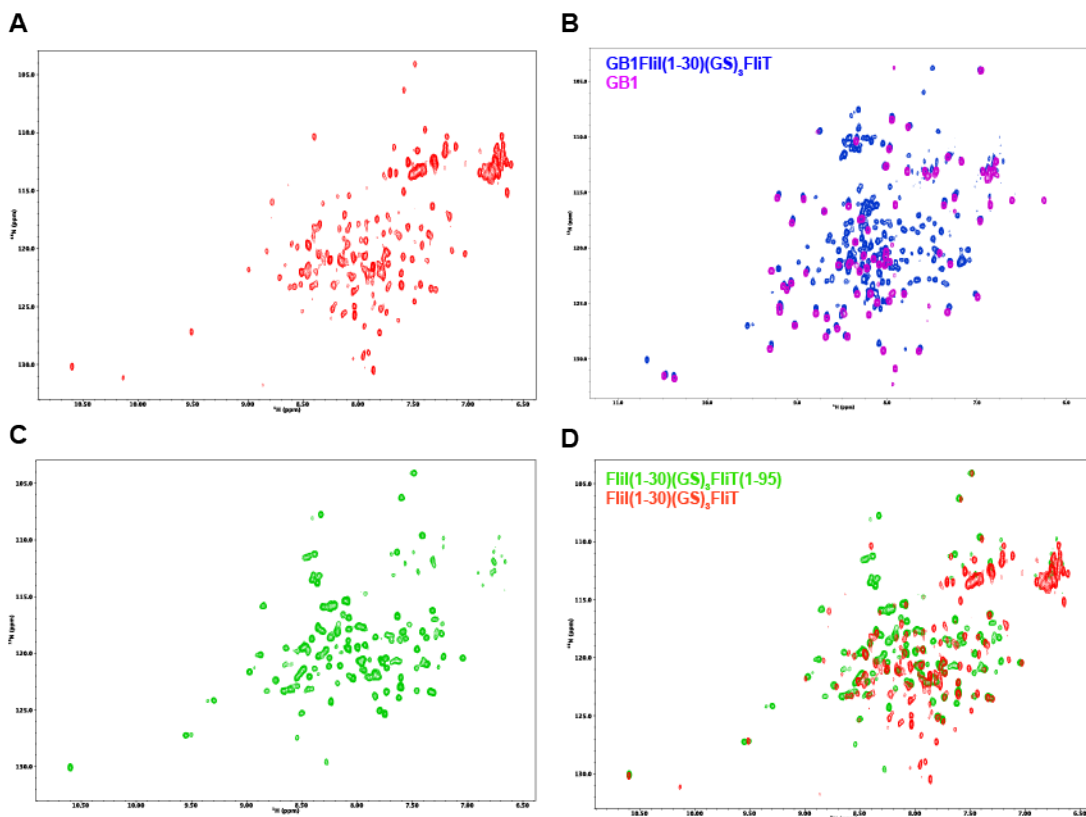


Figure 6-1 ^{15}N -HSQC of different fusion constructs of FliI and FliT. A. ^{15}N -HSQC of U- ^{15}N FliI(1-30)-(GS) $_3$ -FliT. B. ^{15}N -HSQC of U- ^{15}N GB1-FliI(1-30)-(GS) $_3$ -FliT (blue) overlaid with GB1 (magenta). C. ^{15}N -HSQC of U- ^{15}N FliI(1-25)-(GS) $_3$ -FliT(1-95). D. Overlay of ^{15}N -HSQC of FliI(1-25)-(GS) $_3$ -FliT(1-95) (green) with FliI(1-25)-(GS) $_3$ -FliT (red).

disappeared or broadened upon binding. Thus, it was not possible to obtain NOE between the interacting residues of FliI and FliT to characterize their binding interface. The fusion constructs of the extreme N-terminal residues of FliI (FliI_{EN}) with FliT were designed to increase the local concentration between FliI and FliT,

thereby facilitating their structural characterization. The N-terminal thirty residues of FliI were fused to the N-terminal of FliT along with a (GS)₃ linker between them. However, the fusion construct, FliI(1-30)-(GS)₃-FliT, was not suitable for NMR study due to its insolubility in solution and poor quality of ¹⁵N-HSQC spectra (Figure 6-1, A). Introducing GB1 solubility tag in the fusion construct significantly improves the

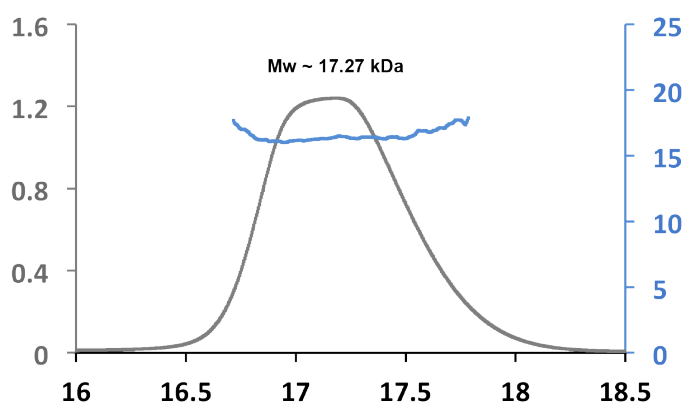


Figure 6-2 Native mass determination of FliT(1-95)-(pcold)-FliI(1-25). A chromatographic trace of the UN detector (grey) is shown with mass measurements of consecutive fractions of the chromatographic peak (blue dots) superimposed.

solubility of fusion construct and its spectral quality (Figure 6-1, B). The NMR structure determination of GB1-FliI(1-30)-(GS)₃-FliT was complicated by the cross-peaks of GB1 tag overlapping with our protein of interest. FliI was proposed to bind the hydrophobic cleft of FliT and binding of FliI to the hydrophobic cleft would release α 4 helix. Considering the fact that the free,

unbound $\alpha 4$ helix in the FliT monomeric state might be the reason for its poor solubility and poor quality spectra, fusion constructs were made with FliT(1-95) where the free α -helix was deleted. Two fusion constructs were designed by attaching the N-terminal twenty five residues of FliI to the N- and C-terminal of FliT(1-95). Both the constructs showed dramatic improvement in solubility and spectral quality (Figure 6-1, C). The ^{15}N -TROSY and ^{13}C -HMQC spectra of both

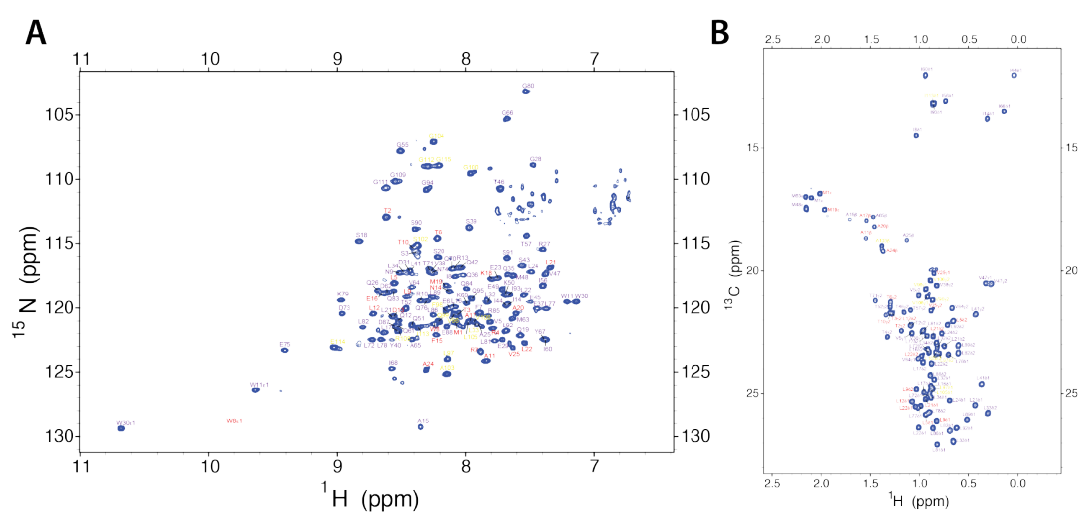


Figure 6-3 ^{15}N -TROSY B. ^{13}C -HMQC of U- $[\text{}^2\text{H}, \text{}^{12}\text{C}, \text{}^{15}\text{N}]$, Ala(β)-, Met(ϵ)-, Val(γ 1, γ 2)-, Leu(δ 1, δ 2)-, Ile(δ 1)-, Thr(γ 2)- $[\text{}^{13}\text{CH}_3]$, Phe-, Tyr- $[\text{}^1\text{H}, \text{}^{13}\text{C}]$, Trp- $[\text{}^1\text{H}]$ FliT(1-95)-pcold-FliI(1-25) showing backbone and side-chain resonance assignment.

the N-terminal and C-terminal fusion constructs showed excellent map in the peak positions. This indicates fusion of the first 25 residues of FliI to either the N-terminal or the C-terminal of FliT(1-95) doesn't impact the structure of fusion

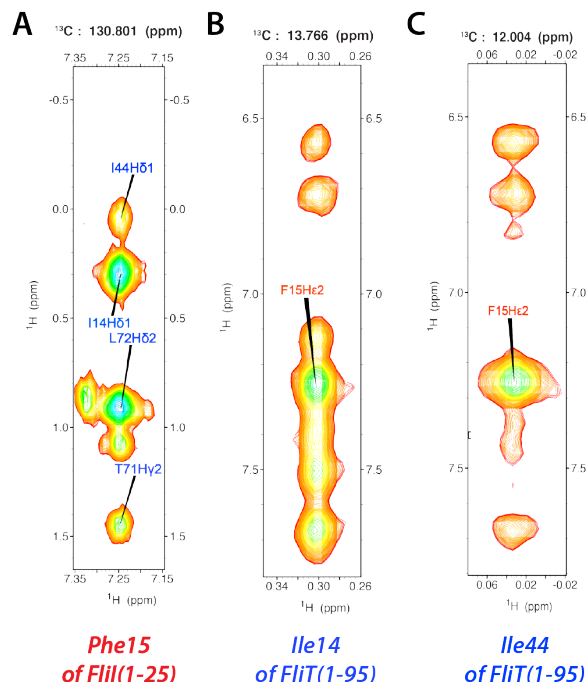


Figure 6-4 NOE between FliT(1-95) and FliI(1-25) in FliT(1-95)-pcold-FliI(1-25) showing FliI(1-25) binds to FliT(1-95) in FliT(1-95)-pcold-FliI(1-25). NOESY strip of ^{13}C NOESY HMQC of A. aromatic and B. and C. aliphatic side-chains. FliT(1-95)-pcold-FliI(1-25) showing NOE between Phe15 of FliI(1-25) and Ile14 and Ile44 of FliT(1-95).

construct. However, in the N-terminal fusion construct, several peaks appeared to be split into two indicating the presence of conformers in slow exchange. Conversely, only one set of peaks is present in the C-terminal fusion construct where the minor peak in N-terminal fusion became the only peak in C-terminal fusion. Perhaps the (GS)₃ linker in the N-term fusion was not sufficiently long to allow for the lowest energy conformation to be fully sampled. The minimal shift in

the peak positions indicates that the structure is a native one and is likely unaffected by the protein engineering strategies necessary to obtain a viable NMR sample. Due to better spectral quality and solubility, the construct, FliT(1-95)-pcold-FliI(1-25) was chosen for structure determination. FliT(1-95)-pcold-FliI(1-25) appeared as monomer in SEC-MALS (Figure 6-2).

6.2.2 Structure determination of fusion construct

We have used U-[^2H , ^{13}C , ^{15}N] sample of FliT(1-95)-(pcold)-(FliI1-25) to accomplish the sequential assignment of ^1HN , ^{15}N , $^{13}\text{C}'$, $^{13}\text{C}_\alpha$ and $^{13}\text{C}_\beta$

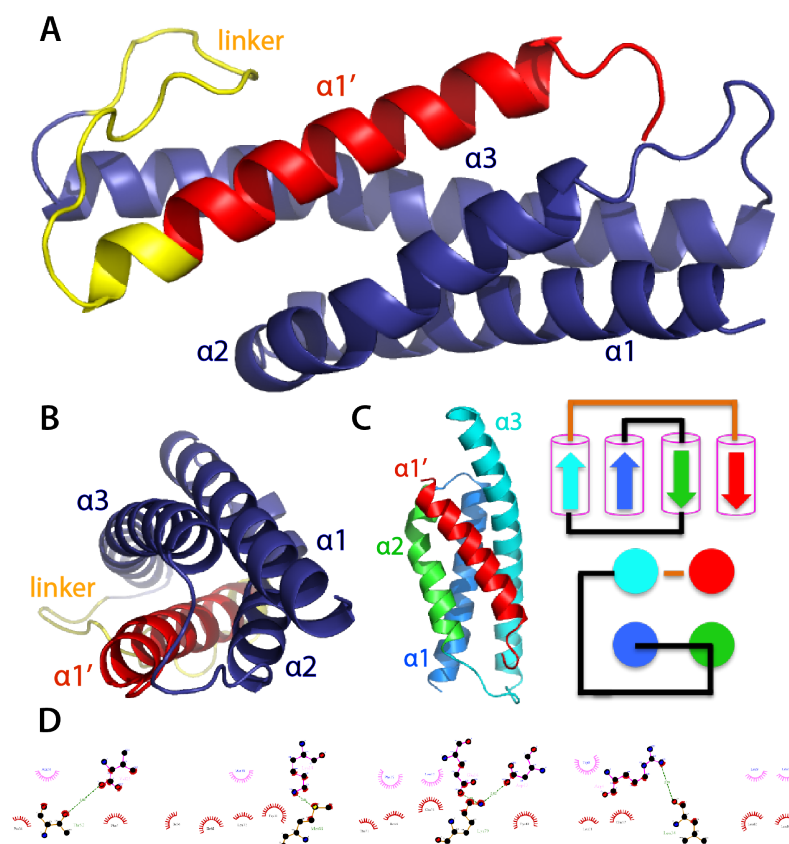


Figure 6-5 Solution structure of FliT(1-95)-pcold-FliI(1-25). A. Side-on view of FliT(1-95)-pcold-FliI(1-25). The $\alpha 1$, $\alpha 2$ and $\alpha 3$ helices of FliT(1-95) are shown in

blue. The $\alpha 1'$ helix of Flil(1-25) is shown in red. The linker region is colored in yellow. B. The end-on view of fusion structure. C. The topology of four helical bundle of FliT(1-95)-pcold-Flil(1-25). The $\alpha 1$, $\alpha 2$ and $\alpha 3$ helices of FliT(1-95) are shown in blue, green and cyan, respectively. The $\alpha 1'$ helix of Flil(1-25) is shown in red. The linker connecting α -helices of FliT(1-95) are shown in black. The linker connecting FliT(1-95) and Flil(1-25) are shown in orange. D. Ligplot image of interface of FliT(1-95) and Flil(1-25) in FliT(1-95)-pcold-Flil(1-25)

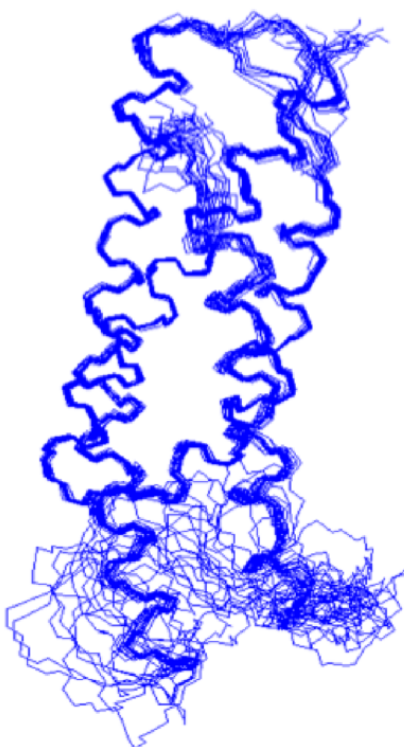


Figure 6-6 Solution NMR structure of fusion construct. Bundle backbone RMSD 0.5Å from **Table 6-1**.

Table 6-1 Summary of NMR structural statistics of FliT(1-95)-FliI(1-25)

Completeness of resonance assignments ^b	FliT(1-95):FliI(1-25)
Backbone (%)	92
Side chain (%)	77
Aromatic (%)	48
Conformationally-restricting restraints ^b	
NOE restraints	
Total	1114
Intra-residue ($i = j$)	103
Sequential ($ i - j = 1$)	270
Medium range ($1 < i - j < 5$)	327
Long range ($ i - j \geq 5$)	414
NOE restraints / residue	10.6
<u>Interchain protein/protein NOEs</u>	115
Hydrogen bond restraints	78/91
Total	180
Dihedral-angle restraints	214
Number of restraints / residue (total / per restrained residue)	1508/14.4
Residual constraint violations ^c	
Average distance violations / structure	
0.1 - 0.2 Å	12.5
0.2 - 0.5 Å	1.5
> 0.5 Å	0.0
Average RMS of distance violation / restraint (Å)	0.02
Maximum distance violation (Å)	0.34
Average dihedral violations / structure	
1 - 10 °	6.5
> 10 °	0.0
Average RMS of distance violation / restraint (°)	0.65
Maximum distance violation (°)	8.60
Model Quality	
RMSD from average coordinates (Å)	
All Backbone atoms (ordered/all)	0.5/1.2
All Heavy atoms (ordered/all)	0.9/1.6
RMSD Bond lengths (Å)	0.019
RMSD Bond angles (°)	1.1
Molprobtity Ramachandran plot ^d	
Most favored regions (%)	97.5
Additionally allowed regions (%)	2.5
Disallowed regions (%)	0.0
Global quality scores (Raw / Z-score)	
Verify3D	0.33/-2.09
ProsaII	0.77/0.50
Procheck G-factor (ϕ, ψ) ^d	0.42/1.97
Procheck G-factor (all dihedrals) ^d	0.21/1.24
MolProbtity clashscore	16.1/-1.24

^a Structural statistics were computed for the ensemble of 20 deposited structures calculated using PSVS 1.5 program.¹⁸

^b Computed for residues 1-115 FliT(1-95), pCold vector (96-115) sequence (chain A) and 1-25 FliI (chain B) excluding exchangeable protons, termini and Pro N backbone. Secondary structure elements (FliT): 2-27 ($\alpha 1$), 31-48 ($\alpha 2$), 58-93 ($\alpha 3$). Secondary structure elements (FliI): 1-25 ($\alpha 1$).

^c Average distance constraints were calculated using the sum of r^{-6} .

^d Ordered residue ranges [$S(\phi) + S(\psi) > 1.8$] : 2-93 (FliT), 1-25 (FliI).

resonances by means of through-bond heteronuclear scalar correlations along the backbone using standard 3D TROSY-based ^2H decoupled triple resonance sequences, HNCO, HNCA, HN(CA)CO, HN(CO)CA, HNCACB and NOESY-TROSY. All the 3D NOESY based pulse sequences, ^{13}C -NOESY-HMQC, ^{13}C -HMQC-NOESY-HMQC, ^{15}N -NOESY-TROSY, were recorded on U- $[^2\text{H}, ^{12}\text{C}, ^{15}\text{N}]$, Ala(β)-, Met(ϵ)-, Val(γ_1, γ_2)-, Leu(δ_1, δ_2)-, Ile(δ_1)-, Thr(γ_2)- $[^{13}\text{C}\text{H}_3]$, Phe-, Tyr- $[^1\text{H}, ^{13}\text{C}]$, Trp- $[^1\text{H}]$ sample for both side-chain assignment and NOE for structure calculations. A 350 ms mixing time was used for all the NOESY experiments.

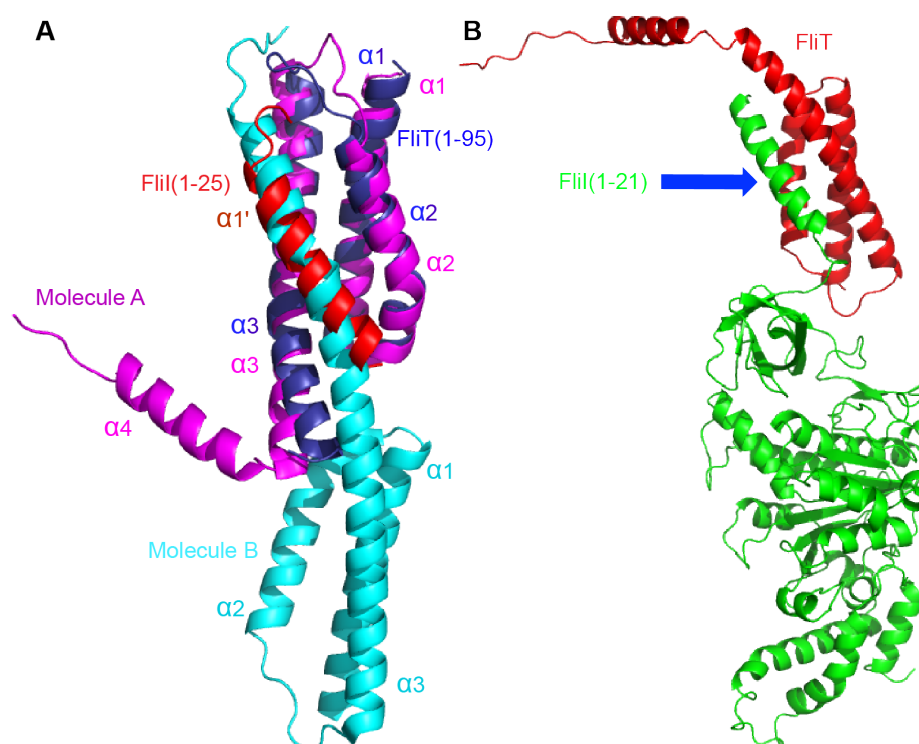


Figure 6-7 Structural comparison of fusion structure with crystal structure of FlIT. A. Structural comparison of fusion structure with crystal structure of FlIT from *S. enterica* (pdb code 3A7M). The α_1 , α_2 and α_3 of FlIT(1-95) in the fusion structure is shown in blue. The α -helix corresponding to FliI(1-25) in red. Each monomer of

FliT dimer is shown in magenta and cyan. FliT(1-95) is structurally aligned with the core structure of molecule A, composed of $\alpha 1$, $\alpha 2$ and $\alpha 3$ helix. The α -helix of FliI(1-25), $\alpha 1'$ is aligned with $\alpha 4$ of molecule. B. Structural model for FliI-FliT complex structure. Color code: FliT in red; FliI in green; The extreme N-terminal α -helix of FliI is shown by blue arrow; All the structural alignments are performed in pymol.

Resonance assignment was ~96% complete for backbone residues and 100% complete for methyl and aromatic side-chains (Figure 6-3). TALOS dihedral angles from backbone chemical shifts indicate that the FliI_{EN} was folded in a helical conformation and unambiguous NOEs were readily identified for the FliI_{EN} and the three helices of the FliT(1-95) segment (Figure 6-4). The structure was calculated using NOE as distance restraints. A total of 1508 restraints that included NOEs, dihedral angle and H- bonds were used for structure calculation. The structural statistics were summarized in (Table 6-1). The calculated solution NMR structure of FliT(1-95)-(pcold)-(FliI1-25) was represented by the 20 lowest energy conformers (Figure 6-6).

6.2.3 Extreme N-terminal residues of FliI form α -helix upon FliT binding

The solution NMR structure of FliT(1-95)-(pcold)-(FliI1-25) represents four helical bundle (Figure 6-5). The structure corresponding to FliT(1-95) forms $\alpha 1$, $\alpha 2$ and $\alpha 3$ helices. The FliI_{EN} binds to the hydrophobic cleft formed by $\alpha 2$ and $\alpha 3$ helix of FliT(1-95) and forms the amphipathic $\alpha 1'$ -helix. The linker at the C-terminal of

FliT(1-95) connects the α -helix of FliI_{EN}. The structural arrangement of fusion structure is similar to the crystal structure of FliT and can be superimposed onto the crystal structure of FliT with root-mean-square (rms) deviation of 1.37 Å (Figure 6-7, A). Our structure shows first structural evidence that FliI_{EN} forms α -helix upon binding to its substrate. There was extensive hydrophobic interaction between hydrophobic residues of hydrophobic cleft of FliT(1-95) and α -helix of

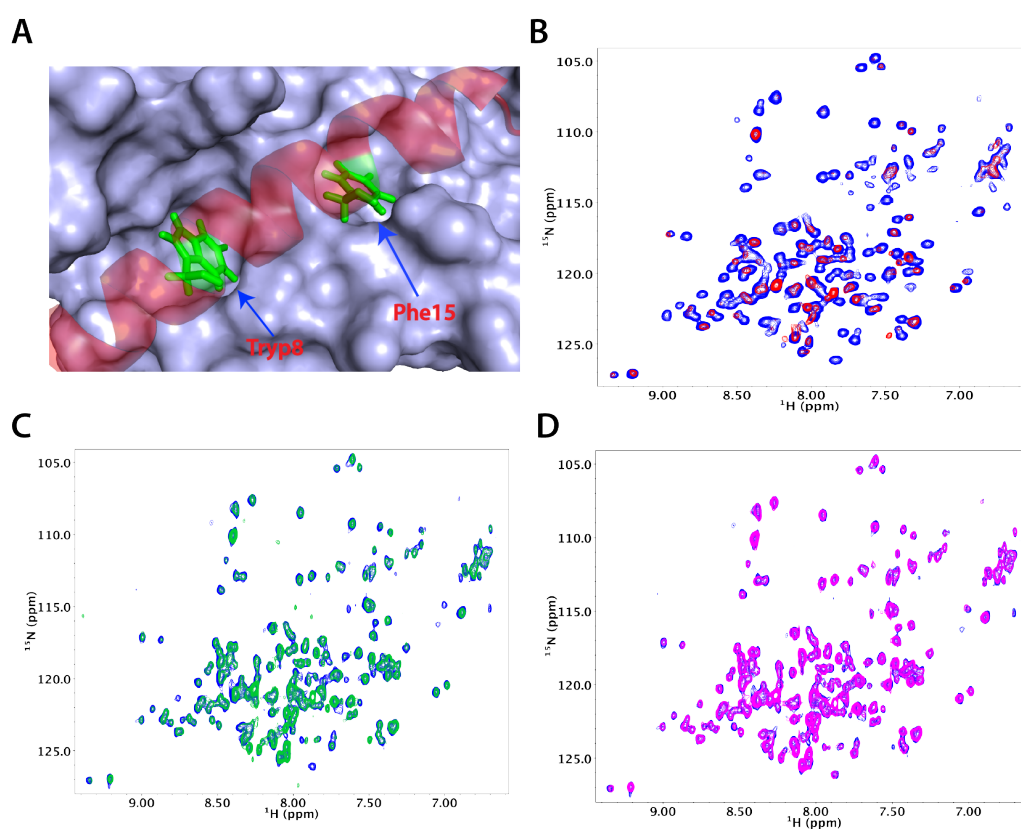


Figure 6-8 ^{15}N -HSQC titration of U- ^{2}H , ^{15}N] FliT with natural abundance FliI mutants. ^{15}N -HSQC of FliT is shown in blue in all superposition spectra. A. The position of Trp8 and Phe15 sidechain in FliT(1-95)-pcold-FliI(1-25) are shown in green stick. The α 1' helix of FliI(1-25) are shown in transparent red cartoon. The FliT(1-95) is shown blue surface. B. The ^{15}N -HSQC of titration FliT with natural

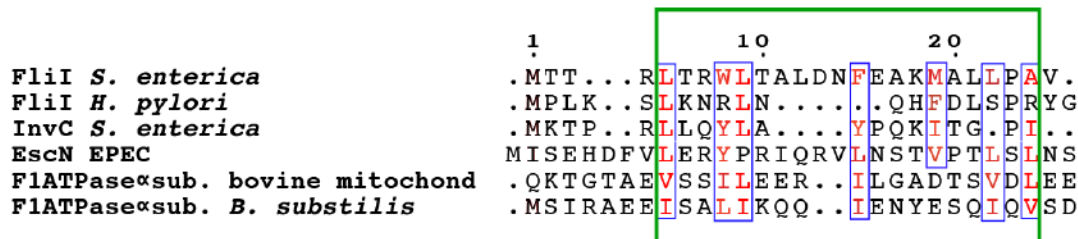
abundance FliI. FliT spectrum with FliI is shown in red. C. The ^{15}N -HSQC of titration FliT with natural abundance FliIW8AF15A. A FliT spectrum with FliI is shown in green. D. The ^{15}N -HSQC of titration FliT with natural abundance FliIW8E. A FliT spectrum with FliI is shown in magenta. In all titrations, FliI or FliI mutants are added in 1:1 ratio.

FliI_{EN} as represented in Figure 6-5 (D). The aromatic side-chains of Phe7, Trp11 and Tyr40 of FliT(1-95) and Trp8 and Phe15 of FliI_{EN} plays crucial role in the hydrophobic interaction between FliT(1-95) and FliI_{EN}. To verify whether fusion structure correctly represents the FliI-FliT interaction, NMR titrations were performed between U- ^{15}N FliIW8AF15A, FliIW8E and FliIF15E and natural abundance FliT. FliIW8AF15A and FliIF15E showed weaker interaction with FliT compared to WT FliI. W8E mutant completely disrupts the interaction between FliI and FliT (Figure 6-8). The structure model of full FliI-FliT complex was calculated by using structure restraint between FliI_{EN} and FliT(1-95) in the FliT(1-95)-(pcold)-(FliI1-25) (Figure 6-7, B).

6.3 Discussion

We have determined the first solution structure of any chaperone-ATPase complex in the flagellar export process or the type III secretion system in general. The complex structure of FliI-FliT shows that first structural evidence that FliI_{EN} binds to the hydrophobic cleft of FliT and forms an amphipathic α -helix. As all the ATPases of the T3SS have structural and functional similarity, it is more likely

A



B

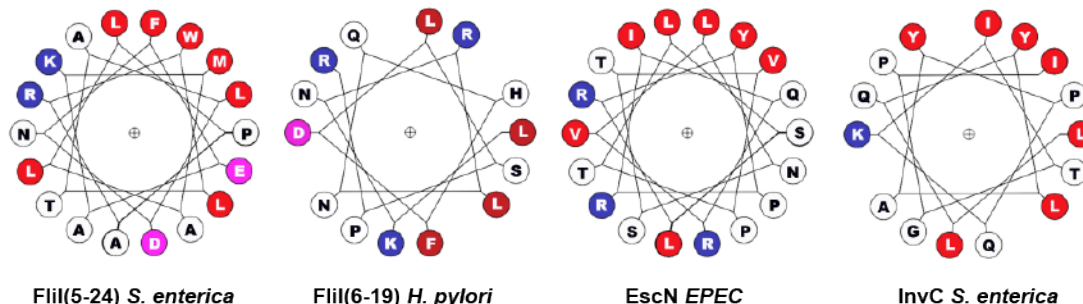


Figure 6-9 A. Sequence alignment extreme N-terminal residues of FliI from *S. enterica*, FliI from *H. pylori*, InvC from *S. enterica*, EscN from EPEC, F₁-ATPase α -subunit from bovine mitochondria and F₁-ATPase α -subunit from *B. subtilis*. B. Helical wheel plot of extreme N-terminal residues of FliI from *S. enterica*, *H. pylori*, EscN from EPEC and InvC from *S. enterica*. Esprint was used to make sequence alignment diagram²³⁹.

that all the homologous T3SS ATPases also have similar tendency to that of FliI. We perform the sequence alignment of the extreme N-terminals of FliI, with the homologue of FliI from *Helicobacter pylori*, InvC from pathogenic *Salmonella enterica*, EscN from EPEC and α -subunit of F₁-ATPase from bovine mitochondria and *Basillus subtilis*. There are conserved hydrophobic residues in

the extreme N-terminals of flagellar export ATPase, T3SS ATPases and α -subunit of F1-ATPases (Figure 6-9, A). The helical wheel plot (Figure 6-9, B) of the extreme N-terminal residues shows that the extreme N-terminals of all the T3SS ATPases will form the amphipathic α -helix if they form α -helix upon binding to its substrate (Figure 6-9, B).

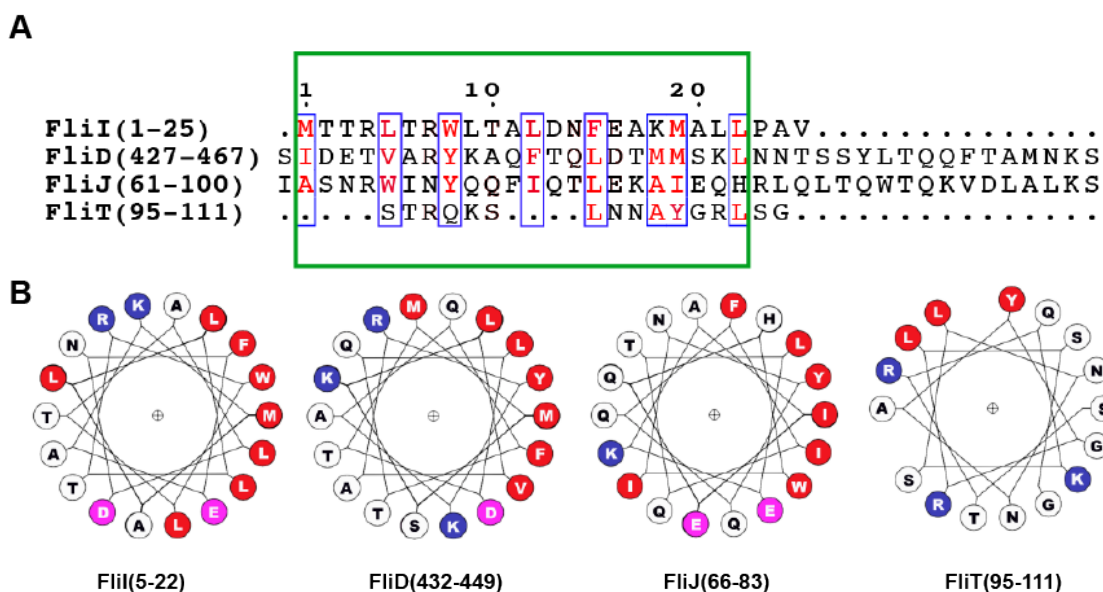


Figure 6-10 A. Sequence alignment of FliT-binding domain of FliI, FliD, FliJ and FliT(95-111). B. Helical wheel plot of FliI(5-22), FliD(432-449), FliJ(66-83) and FliT(95-111). Esprint was used to make sequence alignment diagram²³⁹.

FliJ, FliD and FliH₂C₂ complex are proposed to share same binding site on FliT similar to FliI_{EN}. Sequence alignment between α 4 helix of FliT, FliI_{EN}, and FliT binding domain of FliD and FliJ, show that they have conserved hydrophobic residues in their FliT binding domain (Figure 6-10, A). Helical wheel plot (Figure

6-10, B) of the FliT-binding domain of FliI_{EN}, FliD and FliJ indicate that they would like to form amphipathic α -helices. Thus FliT might share common binding site for FliI_{EN}, FliD and FliJ. Therefore solution structure of FliI-FliT complex will provide structural insight of common binding site of FliT to its binding partners.

The extreme N-terminal residues of FliI control its self-oligomerization⁸⁷. FliI(Δ 1-7) was reported to form monomer in solution⁸⁷. However, there is no structural information available so far regarding the role of FliI_{EN} in its oligomerization. We have found that extreme N-terminals of FliI binds to FliT and forms α -helix upon FliT binding. Moreover, FliT forms FliI-FliT complex by disrupting FliI dimer. Therefore, the formation of extreme N-terminal α -helix might be important for the oligomerization of FliI. Further investigation is necessary to identify the role of extreme N-terminal of FliI in its oligomerization.

Chapter 7 : Materials and Methods

7.1 Expression and Preparation of Proteins

The *FliT* genes encoding FliT from *Salmonella typhimurium*, strain LT2 were synthesized from Genewiz and cloned to Pet16b containing GB1 solubility tag. The *FliI* gene was obtained from Prof. Anastassios Economou lab. *FliI* gene was cloned into pMALS vector with maltose-binding protein (MBP) solubility tag. The plasmids containing *FliI* and *FliT* genes were transformed in BL21 (DE3) cells and plated in the LB plate. In the next day morning, one colony from the plate was transferred into 5 mL of LB media (for the preparation of deuterated samples, LB media was in 75 % D₂O). After ~ 8 hours growing, The cells were centrifuged and transferred in 50 mL of LB media or the minimal media (M9) containing 1 g/L of ¹⁵NH₄Cl and 4 g/L glucose. The cells were centrifuged and washed with LB or M9 media. After overnight growth, the cells were transferred into 1L of LB media or minimal media. The cells were grown at 37 °C in the presence of 100 µg/ml ampicillin all the way. The protein synthesis was induced by the addition of 0.1 mM of IPTG at A₆₀₀ ~ 0.4 and were grown at 18 °C overnight. Afterwards, the cells were harvested at A₆₀₀ ~1.5 for LB media and A₆₀₀ ~1.0 for M9 media and centrifuged at 6000´ g in a 6-liter JLA-8.100 rotor (Beckman). The cells were re-suspended in 50 mM Tris-HCl (pH 8.0), 500 mM NaCl, 5 mM imidazole, 5 mM β-mercaptoethanol buffer. Most of the protein constructs and mutants of FliI and FliT were overexpressed using the protocols described above. FliI has low solubility in minimal media. For over-expression of FliI in protonated or deuterated minimal media, cells were induced with 50 µM IPTG. GB1-FliI(1-30)-

(GS)₃-FlIT has low solubility when over-expressed in either LB or minimal media. GB1-Flil(1-30)-(GS)₃-FlIT were induced with 50 μ M IPTG during their over-expression.

The isotopically labeled samples for NMR studies were prepared by growing the cells in M9 media. U-[¹³C,¹⁵N]- or U-[²H,¹³C,¹⁵N]-labeled samples were prepared by supplementing the growing medium with 1 g/L of ¹⁵NH₄Cl and 2 g/L of [¹³C₆]- or [²H₇,¹³C₆]-glucose in H₂O or 99.9%-²H₂O (CIL). The methyl-protonated samples were prepared as described²⁴⁰. 50 mg/L of alpha-ketobutyric acid (methyl-¹³CH₃) and 85 mg/L of alpha-ketoisovaleric acid (dimethyl-¹³CH₃) were added to the culture 45 minutes prior to addition of IPTG. Met-[¹³CH₃] and Ala-[¹³CH₃] labeled samples were prepared by supplementing the medium with 50 mg/L of [¹³CH₃]-Met and 50 mg/L [²H₂,¹³CH₃]-Ala. All precursors and amino acids (except alanine) were added to the culture 45 minutes prior to the addition of IPTG and alanine was added to the culture 30 minutes prior to the induction. For selective labeling of U-[¹³C,¹⁵N]-Phe, U-[¹³C,¹⁵N]-Tyr in the methyl labeled sample, 50mg/L of U-[¹³C,¹⁵N]-Phe and U-[¹³C,¹⁵N]-Tyr are added to the cell culture 30 minutes prior to induction. For methyl labeling of threonine residues, 50 mg/L labeled U-²H, Thr- γ 2[¹³CH₃], along with 100mg/L d₅-glycine were added to the cell cultures 30 minutes prior to induction.

All protein samples were prepared as His-tagged derivatives with either maltose binding protein (MBP) or GB1 solubility tags and were purified over a nickel-chelating Sepharose column (GE Healthcare). The cells were lysed and centrifuged at 50,000 \times g using a JA-25.50 rotor (Beckman). The supernatant

was loaded on a Ni-column pre-equilibrated with 50 mM Tris-HCl (pH 8.0), 500 mM NaCl, 5 mM imidazole, 5 mM β -mercaptoethanol (β ME) buffer, and then washed with 50 mM Tris-HCl (pH 8.0), 500 mM NaCl, 50 mM imidazole, 1 mM β ME buffer. The protein was eluted with buffer containing 50 mM Tris-HCl (pH 8.0), 100 mM NaCl, 400 mM imidazole, 5 mM β ME. Then the protein was exchanged into buffer 50mM Tris, 50mM NaCl, 5mM β ME, pH=8.0 and kept overnight at 4°C after addition of TEV. 1 OD280 of TEV protease per 50 OD280 of substrate was used for overnight digest. The protein sample was loaded again Ni-column pre-equilibrated with 50 mM Tris-HCl (pH 8.0), 50 mM NaCl, 10 mM imidazole, 5 mM β ME buffer. The protein of interest comes out in the flow through and his-tagged derivatives with solubility tags and TEV protease elute with 50 mM Tris-HCl (pH 8.0), 50 mM NaCl, 400 mM imidazole, 5 mM β ME buffer. The protein was exchanged into 50mM Tris, 50 mM NaCl, pH=8.0 buffer and loaded into Hitrap FF 16/10 Q column pre-equilibrated with 50mM Tris, 50 mM NaCl, pH=8.0 buffer. Gradient was run with 50mM Tris, 1M NaCl, pH=8.0 buffer and protein comes out between 150 mM to 250 mM NaCl concentration. Later on, the protein samples were concentrated and injected into a Superdex-75/200 size exclusion column (GE Healthcare) depending on the protein size. The protein concentration was determined spectrophotometrically at 280 nm and the protein purity was confirmed by SDS-PAGE. For the expression and purification of the different protein constructs and mutants of FliT and FliI, same purification procedure was used as for the wild type proteins.

7.2 Polymerase Chain Reaction (PCR)

All mutations were introduced by site-directed mutagenesis (Quick-Change, Stratagene) using PfuUltra™ High Fidelity DNA polymerase. The following steps were used for PCR site directed mutagenesis:

- 1) Wild-type plasmid was isolated using Qiagen kit.
- 2) Plasmid template DNA (approximately 0.5 pmoles) and 12-20 pmoles of forward and reverse primers were then added to a PCR mix (from Stratagene site directed mutagenesis kit) containing mutagenesis buffer (20 mM Tris-HCl, pH 7.5, 8 mM MgCl₂, 40 µg/mL BSA), dNTP and Pfu DNA polymerase.
- 3) PCR was performed using the following cycle:

Initiation	Denaturation	Annealing	Elongation	Final Elongation	Final Hold
95 °C	95 °C	55 °C	68 °C	68 °C	4 °C
2 min	30 sec	1 min	8 min	7 min	

- 4) DpnI digestion was performed to remove parental (wild type) methylated DNA. The reaction mixture was incubated at 37 °C for 3 h.
- 5) The plasmid containing the point mutation was transformed into DH5_α competent cells and plated. Colonies were screened. The plasmids were isolated from positive colonies and sequenced.

To make all deletion/insertion construct, the above procedures were same but different PCR cycles have been used.

7.3 MALS Experiments

Multi-angle light scattering was measured using DAWN HELEOS-II (Wyatt Technology Corporation) downstream of a Shimadzu liquid chromatography system connected to a Superdex 200 10/300 GL (GE Healthcare) gel filtration column. The running buffer was 20mMKPi (pH 7.0), 100 mM KCl, 5 mM β ME and 0.05% NaN_3 . Two hundred microliters of the sample was injected for each run. The data were analyzed with ASTRA version 6.0.5 (Wyatt Technology Corporation).

Composition-gradient multi-angle light scattering (CG-MALS) experiments were performed with a Calypso II composition gradient system (Wyatt Technology Corporation) plumbed to a HELEOS II multi-angle light scattering (MALS) detector (Wyatt) and inline UV/Vis concentration detector (Waters Corporation). CG-MALS data collection and analysis were performed with the CALYPSO software (Wyatt). All experiments were performed in phosphate buffered saline (PBS; 20 mM potassium phosphate, 100 mM KCl, 0.5 mM EDTA, 1 mM DTT, pH 7.0), filtered to 0.1 μm . FliI and FliT were diluted to concentrations of 0.4 mg/mL and 1 mg/mL, respectively, in PBS and filtered to 0.1 μm using a syringe-tip filter (Anotop, Whatman) prior to loading on the Calypso hardware. A three-part CG-MALS method was run consisting of concentration gradients in each protein to assess the monomer molecular weight and any self-association behavior and a single “crossover” hetero-association gradient to quantify the interaction between the two proteins. For each self-association gradient, the Calypso combined an aliquot of FliI or FliT and buffer, injected the mixture into the MALS detector, and

stopped the flow for 60 s to allow the reaction to come to equilibrium in the MALS flow cell. For the hetero-association gradient, the Calypso prepared eleven different combinations of FliI and FliT, injected them into the detector, and stopped the flow for 300 s to allow the reaction to come to equilibrium. Light scattering data as a function of composition were fit to a model that included the equilibrium homodimerization of FliI and FliT and the interactions between each species. Dynamic light scattering (DLS) data were also collected to assess the size of FliI and FliT associations in addition to molar mass. DLS data were collected during simultaneously with CG-MALS data in the same measurement volume using the Wyatt QELS module installed in the HELEOS. DLS data were analyzed using ASTRA software (Wyatt). To confirm the weak self-association of FliT into equilibrium dimers, additional static light scattering (SLS) and DLS data were collected in batch using the DynaPro NanoStar (Wyatt) and analyzed with DYNAMICS software (Wyatt). FliT was prepared at 2 mg/mL and 1.6 mg/mL in PBS and filtered to 0.1 μm . Solutions were measured in a calibrated quartz cuvette, and the resulting weight average molar mass (M_w) from SLS and hydrodynamic radius (R_h) from DLS were concatenated with the CG-MALS data to quantify the equilibrium dimerization of FliT.

7.4 ITC Experiments

Calorimetric titrations were carried out on an iTC200 microcalorimeter (GE Healthcare) at temperature 15 $^{\circ}\text{C}$. All protein samples were extensively dialyzed against ITC buffer containing 20 mM potassium phosphate (pH 7.0), 100 mM KCl, and 1 mM tris(2-carboxyethyl)phosphine. All solutions were filtered using

membrane filters (pore size, 0.45 μm) and thoroughly degassed for 20 minutes before the titrations. For the experiments performed on iTC200, the sample cell (200 μl) was filled with $\sim 50\text{-}100$ μM protein (FliI), and the 40- μl injection syringe was filled with 250 to 400 μM solution of protein (FliT). The titrations were carried out with a preliminary 0.2 μl injection, followed by 12 injections of 3 μl each with time intervals of 3 minutes. The solution was stirred at 1000 rpm. Data for the preliminary injection, which are affected by diffusion of the solution from and into the injection syringe during the initial equilibration period, were discarded. Binding isotherms were generated by plotting heats of reaction normalized by the moles of injectant versus the ratio of total injectant to total protein per injection. The data were fitted with Origin 7.0 (OriginLab Corporation).

7.5 ATPase Assays.

ATPase activity of FliI was measured using ADP-Glo™ Kinase Assay kit (Promega, V9101). The luminescence was measured in Tecan Infinite M200 pro plate reader using 96-well plate. The luminescence was correlated using ADP-to-ATP conversion curve. The reaction buffer for all ATPase reaction consists of 20mM HEPES, 100mM NaCl, 0.5mM EDTA, 1mM DTT, 5mM MgCl_2 , 0.1 mg/ml BSA, pH=8.0. 25 μL of reaction volume was used for all ATPase reactions. All the reactions were performed with 1mM ATP concentration at 25 °C. ATPase activity was carried for 1 μM FliI and mixtures of FliI and FliT, 1 μM FliI + 10 μM FliT, 1 μM FliI + 20 μM FliT, 1 μM FliI + 50 μM FliT. The reaction was stopped at various time-points 30, 60, 120 and 180 minutes by adding 25 μL of ADP-glo reagent. After incubating the reaction mixtures at room temperature for 40

minutes, Kinase Detection Reagent was added. Luminescence was recorded after 60 minutes of adding Kinase Detection Reagent.

To make the conversion curve, various ratios of ATP to ADP was adjusted from 100% ATP to 100% ADP using a 8-point dilution curve in a 25 μ L of reaction

Percent conversion of ATP to ADP represented by the Standard Curve

% ADP	100	75	50	25	3	2	1	0
% ATP	0	25	50	75	97	98	99	100

volume. The sum of concentrations of ATP and ADP was kept 1 mM for all the points. All the reactions for ATP-to-ADP conversion curve were performed in the ATPase reaction buffer. 25 μ L of ADP-glo reagent was added to the reaction mixture, mixed well and kept at room temperature for 40 minutes. Then 50 μ L of Kinase Detection reagent was added and the reading was taken after 60 minutes.

7.6 NMR Spectroscopy.

All NMR data were collected at 25 °C on Bruker 600 MHz, Varian 600 MHz, Bruker 700 MHz and Varian 800 MHz spectrometers. All recorded spectra were processed with NMRPipe²⁴¹ and analyzed with SPARKY²⁴², NMRVIEW²⁴³. All the NMR samples were prepared in 20mM KPi, 100mM KCl, 0.05% NaN₃, 5mM BME, pH=7.0 buffer. For Flii(18-100), 200mM KCl salt concentration was used. All the spectra were recorded at 25°C unless mentioned otherwise. All the NMR titrations were performed at 25°C. Backbone resonance was assigned using with

either U-[^{13}C , ^{15}N] or U-[^2H , ^{13}C , ^{15}N] sample and standard 3D triple resonance experiments. Backbone chemical shift referencing was adjusted for ^2H shift and dihedral angles extracted using TALOS ²⁴⁴. 3D HMQC-based NOESY experiments (350 ms mixing time) were used to obtain straightforward methyl and aromatic sidechain assignments by leveraging the methyl trossy effect. Assignment for methyl group of Ile, Val, Leu, Ala, Thr, Met, and aromatic Phe, Tyr was obtained with a {U-[^2H , ^{12}C , ^{15}N]; Ile δ 1-[$^{13}\text{CH}_3$]; Ala, Leu, Met, Thr, Val-[$^{13}\text{CH}_3$]; Phe, Tyr, U-[^1H , ^{13}C , ^{15}N], Trp} sample. Additional key Trp aromatic ^{13}C chemical shift were obtained from a [U- ^{13}C , ^{15}N] FliT: FliI sample that otherwise gave data of insufficient quality for assignment and structure determination.

7.7 Structure Calculations.

Structure calculations were carried out with CYANA 3.0²⁴⁵ and 3D-NOESY peaklists, chemical shift-derived dihedral angles (TALOSN) and ($i-i+4$) hydrogen bonds to further restrain helical geometry the resulting 20 lowest target function ensemble of structures was energy refined in explicit water using the established CNS protocol. The structure statistics are reported in Table 6-1.

References

- ¹ Macnab, R. M. How bacteria assemble flagella. *Annu Rev Microbiol.* **57**, 77-100 (2003).
- ² Murphy, G. E., Leadbetter, J. R. & Jensen, G. J. In situ structure of the complete *Treponema primitia* flagellar motor. *Nature* **442**, 1062-1064 (2006).
- ³ Samatey, F. A., Matsunami, H., Imada, K., Nagashima, S., Shaikh, T. R., Thomas, D. R., Chen, J. Z., Derosier, D. J., Kitao, A. & Namba, K. Structure of the bacterial flagellar hook and implication for the molecular universal joint mechanism. *Nature* **431**, 1062-1068 (2004).
- ⁴ Minamino, T. Protein export through the bacterial flagellar type III export pathway. *Biochimica et biophysica acta* **1843**, 1642–8 (2014).
- ⁵ Suzuki, H., Yonekura, K. & Namba, K. Structure of the rotor of the bacterial flagellar motor revealed by electron cryomicroscopy and single-particle image analysis. *Journal of molecular biology* **337**, 105–13 (2004).
- ⁶ Morimoto, Y. V. *et al.* Assembly and stoichiometry of FliF and FliA in *Salmonella* flagellar basal body. *Molecular microbiology* **91**, 1214–26 (2014).
- ⁷ Thomas, D. R., Francis, N. R., Xu, C. & DeRosier, D. J. The Three-Dimensional structure of the flagellar rotor from a clockwise-locked mutant of *Salmonella enterica* Serovar Typhimurium. *Journal of Bacteriology* **188**, 7039-7048 (2006).
- ⁸ Marykwas, D. L., Schmidt, S. A. & Berg, H. C. Interacting components of the flagellar motor of *Escherichia coli* revealed by the two-hybrid system in yeast. *Journal of molecular biology* **256**, 564–76 (1996).
- ⁹ Tang, H., Braun, T. F. & Blair, D. F. Motility Protein Complexes in the Bacterial Flagellar Motor. *Journal of Molecular Biology* **261**, 209-221 (1996).
- ¹⁰ Kubori, T., Yamaguchi, S. & Aizawa, S. Assembly of the switch complex onto the MS ring complex of *Salmonella typhimurium* does not require any other flagellar proteins. *Journal of Bacteriology* **179**, 813-817 (1997).
- ¹¹ Francis, N.R., Irikura, V.M. & Yamaguchi, S. Localization of the *Salmonella typhimurium* flagellar switch protein FliG to the cytoplasmic M-ring face of the basal body. (1992).
- ¹² Brown, P. N., Mathews, M. A. A., Joss, L. A., Hill, C. P., David, F. & Blair, D. F. Crystal Structure of the Flagellar Rotor Protein FliN from *Thermotoga maritima*. *Journal of Bacteriology* **187**, 2890-2902 (2005).
- ¹³ Sang-Youn Park, S. Y., Lowder, B., Bilwes, A. M., Blair, D. F. & Crane, B. R. Structure of FliM provides insight into assembly of the switch complex in the bacterial flagella motor. *Proceedings of National Academy of Sciences* **103**, 11886-11891 (2006).
- ¹⁴ Francis, N. R., Sosinsky, G. E., Thomas, D. & DeRosier, D. J. Isolation, characterization and structure of bacterial flagellar motors containing the switch complex. *Journal of molecular biology* **235**, 1261–70 (1994).
- ¹⁵ Brown, P.N., Terrazas, M., Paul, K. & Blair, D.F. Mutational analysis of the flagellar protein FliG: sites of interaction with FliM and implications for organization of the switch complex. *Journal of Bacteriology* **189**, 305-312 (2007).

-
- ¹⁶ Thomas, D., Francis, N., Xu, C. & DeRosier, D. The Three-Dimensional Structure of the Flagellar Rotor from a Clockwise-Locked Mutant of *Salmonella enterica* Serovar Typhimurium. *Journal of Bacteriology* **188**, 7039–7048 (2006).
- ¹⁷ Jones, C. J., Homma, M. & Macnab, R. M. L-, P-, and M-ring proteins of the flagellar basal body of *Salmonella typhimurium*: gene sequences and deduced protein sequences. *Journal of bacteriology* **171**, 3890–900 (1989).
- ¹⁸ Hizukuri, Y., Yakushi, T., Kawagishi, I. & Homma, M. Role of the intramolecular disulfide bond in FlgI, the flagellar P-ring component of *Escherichia coli*. *Journal of bacteriology* **188**, 4190–7 (2006).
- ¹⁹ Schoenhals, G. J. & Macnab, R. M. Physiological and biochemical analyses of FlgH, a lipoprotein forming the outer membrane L ring of the flagellar basal body of *Salmonella typhimurium*. *Journal of bacteriology* **178**, 4200–7 (1996).
- ²⁰ Minamino, T., Imada, K. and Namba, K. Mechanisms of type III protein export for bacterial flagellar assembly. *Molecular bioSystems* **4**, 1105–15 (2008).
- ²¹ Minamino, T., Yamaguchi, S. & Macnab, R. M. Interaction between FliE and FlgB, a proximal rod component of the flagellar basal body of *Salmonella*. *Journal of bacteriology* **182**, 3029–36 (2000).
- ²² Saijo-Hamano, Y., Uchida, N., Namba, K. & Oosawa, K. In vitro characterization of FlgB, FlgC, FlgF, FlgG, and FliE, flagellar basal body proteins of *Salmonella*. *Journal of molecular biology* **339**, 423–35 (2004).
- ²³ Homma, M., Kutsukake, K., Hasebe, M., Iino, T. & Macnab, R. M. FlgB, FlgC, FlgF and FlgG. A family of structurally related proteins in the flagellar basal body of *Salmonella typhimurium*. *Journal of Molecular Biology* **211**, 465–77 (1990).
- ²⁴ Lloyd, S., Tang, H., Wang, X., Billings, S. & Blair, D. Torque generation in the flagellar motor of *Escherichia coli*: evidence of a direct role for FliG but not for FliM or FliN. *Journal of bacteriology* **178**, 223–31 (1996).
- ²⁵ Zhou, J. & Blair, D. F. Residues of the cytoplasmic domain of MotA essential for torque generation in the bacterial flagellar motor. *Journal of molecular biology* **273**, 428–39 (1997).
- ²⁶ Zhou, J., Lloyd, S. A. & Blair, D. F. Electrostatic interactions between rotor and stator in the bacterial flagellar motor. *Proceedings of the National Academy of Sciences of the United States of America* **95**, 6436–41 (1998).
- ²⁷ Chun, S. Y. & Parkinson, J. S. Bacterial motility: membrane topology of the *Escherichia coli* MotB protein. *Science (New York, N.Y.)* **239**, 276–8 (1988).
- ²⁸ Braun, T. F., Al-Mawsawi, L. Q., Kojima, S. & Blair, D. F. Arrangement of core membrane segments in the MotA/MotB proton-channel complex of *Escherichia coli*. *Biochemistry* **43**, 35–45 (2004).
- ²⁹ Braun, T. F. & Blair, D. F. Targeted disulfide cross-linking of the MotB protein of *Escherichia coli*: evidence for two H(+) channels in the stator Complex. *Biochemistry* **40**, 13051–9 (2001).
- ³⁰ Zhou, J. *et al.* Function of protonatable residues in the flagellar motor of *Escherichia coli*: a critical role for Asp 32 of MotB. *Journal of bacteriology* **180**, 2729–35 (1998).

-
- ³¹ Kojima, S. & Blair, D. F. Conformational change in the stator of the bacterial flagellar motor. *Biochemistry* **40**, 13041–50 (2001).
- ³² DePamphilis, M. L. & Adler, J. Purification of intact flagella from *Escherichia coli* and *Bacillus subtilis*. *Journal of bacteriology* **105**, 376–83 (1971).
- ³³ Wagenknecht, T., David, J., DeRosier, D. J., Aizawa, S., Robert M. & Macnab R. M. Flagellar hook structures of *Caulobacter* and *Salmonella* and their relationship to filament structure. *Journal of Molecular Biology* **162**, 69–87 (1982).
- ³⁴ Berg, H. C. & Anderson, R. A. Bacteria swim by rotating their flagellar filaments. *Nature* **245**, 380–382 (1973).
- ³⁵ Turner, L., Ryu, W. & Berg, H. Real-Time Imaging of Fluorescent Flagellar Filaments. *Journal of Bacteriology* **182**, (2000).
- ³⁶ Williams, A.W., Yamaguchi, S. & Togashi, F. Mutations in *fliK* and *flhB* affecting flagellar hook and filament assembly in *Salmonella typhimurium*. *Journal of Bacteriology* **178**, 2960–2970 (1996).
- ³⁷ Samatey, F. A. *et al.* Structure of the bacterial flagellar hook and implication for the molecular universal joint mechanism. *Nature* **431**, 1062–8 (2004).
- ³⁸ Homma, M., Kutsukake, K., Iino, T. & Yamaguchi, S. Hook-associated proteins essential for flagellar filament formation in *Salmonella typhimurium*. *Journal of bacteriology* **157**, 100–8 (1984).
- ³⁹ Ikeda, T., Homma, M., Iino, T., Asakura, S. & Kamiya, R. Localization and stoichiometry of hook-associated proteins within *Salmonella typhimurium* flagella. *Journal of bacteriology* **169**, 1168–73 (1987).
- ⁴⁰ O'Brien, E. J. & Bennett, P. M. Structure of straight flagella from a mutant *Salmonella*. *Journal of Molecular Biology*, **70**, 133–152 (1972).
- ⁴¹ Mimori, Y. *et al.* The Structure of the R-type Straight Flagellar Filament of *Salmonella* at 9 Å Resolution by Electron Cryomicroscopy. *Journal of Molecular Biology* **249**, 6987 (1995).
- ⁴² Calladine, C. R. Design requirements for the construction of bacterial flagella. *Journal of Theoretical Biology* **57**, 469–489 (1976).
- ⁴³ Calladine, C. R. Construction of bacterial flagella. *Nature* **255**, 121–124 (1975).
- ⁴⁴ Yonekura, K., Maki-Yonekura, S. & Namba, K. Complete atomic model of the bacterial flagellar filament by electron cryomicroscopy. *Nature* **424**, 643–50 (2003).
- ⁴⁵ Samatey, F. A. *et al.* Structure of the bacterial flagellar protofilament and implications for a switch for supercoiling. *Nature* **410**, 331–7 (2001).
- ⁴⁶ Larsen, S. H., Reader, R. W., Kort, E. N., Tso W. W. & Adler, J. Change in direction of flagellar rotation is the basis of the chemotactic response in *Escherichia coli*. *Nature* **249**, 74–77 (1974).
- ⁴⁷ Macnab, R. M. & Ornston, M. K. Normal-to-curly flagellar transitions and their role in bacterial tumbling. Stabilization of an alternative quaternary structure by mechanical force. *Journal of Molecular Biology*, **112**, 1–30 (1977).
- ⁴⁸ Turner, L., Ryu, W. & Berg, H. Real-Time Imaging of Fluorescent Flagellar Filaments. *Journal of Bacteriology* **182**, (2000).

-
- ⁴⁹ Ikeda, T., Oosawa, K. & Hotani, H. Self-assembly of the filament capping protein, FliD, of bacterial flagella into an annular structure. *Journal of molecular biology* **259**, 679–86 (1996).
- ⁵⁰ Imada, K., Vonderviszt, F., Furukawa, Y., Oosawa, K. & Namba, K. Assembly characteristics of flagellar cap protein HAP2 of Salmonella: decamer and pentamer in the pH-sensitive equilibrium. *Journal of molecular biology* **277**, 883–91 (1998).
- ⁵¹ Yonekura, K. *et al.* The bacterial flagellar cap as the rotary promoter of flagellin self-assembly. *Science (New York, N.Y.)* **290**, 2148–52 (2000).
- ⁵² Economou, A. Following the leader: bacterial protein export through the Sec pathway. *Trends in microbiology* **7**, 315–20 (1999).
- ⁵³ Mori, H. & Ito, K. The Sec protein-translocation pathway. *Trends in microbiology* **9**, 494–500 (2001).
- ⁵⁴ Chevance, F. F. & Hughes, K. T. Coordinating assembly of a bacterial macromolecular machine. *Nature reviews microbiology* **6**, 455–65 (2008).
- ⁵⁵ Cornelis, G. R. The type III secretion injectisome. *Nature reviews microbiology* **4**, 811–25 (2006).
- ⁵⁶ Galán, J. E. & Collmer, A. Type III secretion machines: bacterial devices for protein delivery into host cells. *Science (New York, N.Y.)* **284**, 1322–8 (1999).
- ⁵⁷ Minamino, T. & MacNab, R. M. Interactions among components of the Salmonella flagellar export apparatus and its substrates. *Molecular microbiology* **35**, 1052–64 (2000).
- ⁵⁸ Minamino, T., Doi, H. & Kutsukake, K. Substrate specificity switching of the flagellum-specific export apparatus during flagellar morphogenesis in Salmonella typhimurium. *Bioscience biotechnology and biochemistry* **63**, 1301–3 (1999).
- ⁵⁹ Williams, A. W. *et al.* Mutations in fliK and flhB affecting flagellar hook and filament assembly in Salmonella typhimurium. *Journal of bacteriology*, **178**, 2960–70 (1996).
- ⁶⁰ Kutsukake, K., Minamino, T. & Yokoseki, T. Isolation and characterization of FliK-independent flagellation mutants from Salmonella typhimurium. *Journal of bacteriology* **176**, 7625–9 (1994).
- ⁶¹ Zhu, K., González-Pedrajo, B. & Macnab, R. M. Interactions among membrane and soluble components of the flagellar export apparatus of Salmonella. *Biochemistry* **41**, 9516–24 (2002).
- ⁶² Minamino, T. & Macnab, R. Interactions among components of the Salmonella flagellar export apparatus and its substrates. *Molecular Microbiology* **35**, 1052–1064 (2000).
- ⁶³ Minamino, T. & Macnab, R. M. Components of the Salmonella Flagellar Export Apparatus and Classification of Export Substrates. *Journal of Bacteriology* **181**, 1388–1394 (1999).
- ⁶⁴ Minamino, T., Iino, T. & Kutsukake, K. Molecular characterization of the Salmonella typhimurium flhB operon and its protein products. *Journal of bacteriology* **176**, 7630–7637 (1994).

-
- ⁶⁵ Ohnishi, K., Fan, F., Schoenhals, G. J., Kihara, M. & Macnab, R. M. The FliO, FliP, FliQ, and FliR proteins of *Salmonella typhimurium*: putative components for flagellar assembly. *Journal of bacteriology* **179**, 6092–9 (1997).
- ⁶⁶ Katayama, E., Shiraishi, T., Oosawa, K., Baba, N. & Aizawa, S. Geometry of the flagellar motor in the cytoplasmic membrane of *Salmonella typhimurium* as determined by stereo-photogrammetry of quick-freeze deep-etch replica images. *Journal of molecular biology* **255**, 458–75 (1996).
- ⁶⁷ Chen, S. *et al.* Structural diversity of bacterial flagellar motors. *The EMBO journal* **30**, 2972–81 (2011).
- ⁶⁸ Kihara, M., Minamino, T., Yamaguchi, S. & Macnab, R. M. Intergenic suppression between the flagellar MS ring protein FliF of *Salmonella* and FlhA, a membrane component of its export apparatus. *Journal of bacteriology* **183**, 1655–62 (2001).
- ⁶⁹ Hara, N., Namba, K. & Minamino, T. Genetic characterization of conserved charged residues in the bacterial flagellar type III export protein FlhA. *PloS one* **6**, e22417 (2011).
- ⁷⁰ Barkar, C. S. & Samatey, F. A. Cross-Complementation Study of the Flagellar Type III Export Apparatus Membrane Protein FlhB. *PloS One* **7**, 1-13 (2012).
- ⁷¹ McMurry, J. L., Van Arnem, J. S., Kihara, M. & Macnab, R. M. Analysis of the cytoplasmic domains of *Salmonella* FlhA and interactions with components of the flagellar export machinery. *Journal of bacteriology* **186**, 7586–92 (2004).
- ⁷² Van Arnem, J. S., McMurry, J. L. & Kihara, M. Analysis of an Engineered *Salmonella* Flagellar Fusion Protein, FliR-FlhB. *Journal of Bacteriology* **186**, 2495-2498 (2004).
- ⁷³ Barker, C. S., Meshcheryakeva, I. V., Kostyukova, A. S., Samatev, F. A. FliO regulation of FliP in the formation of the *Salmonella enterica* flagellum. *PloS Genetics* **6**, 1-10 (2010).
- ⁷⁴ Saijo-Hamano, Y. *et al.* Structure of the cytoplasmic domain of FlhA and implication for flagellar type III protein export. *Molecular microbiology* **76**, 260–8 (2010).
- ⁷⁵ Bange, G. *et al.* FlhA provides the adaptor for coordinated delivery of late flagella building blocks to the type III secretion system. *Proceedings of the National Academy of Sciences of the United States of America* **107**, 11295–300 (2010).
- ⁷⁶ Meshcheryakov, V. A., Kitao, A., Matsunami, H. & Samatey, F. A. Inhibition of a type III secretion system by the deletion of a short loop in one of its membrane proteins. *Acta crystallographica. Section D, Biological crystallography* **69**, 812–20 (2013).
- ⁷⁷ Vogler, A. P., Homma, M., Irikura, V. M. & Macnab, R. M. *Salmonella typhimurium* mutants defective in flagellar filament regrowth and sequence similarity of FliI to FOF1, vacuolar, and archaeobacterial ATPase subunits. *Journal of bacteriology* **173**, 3564–72 (1991).
- ⁷⁸ Dreyfus, G., Williams, A. W., Kawagishi, I. & Macnab, R. M. Genetic and biochemical analysis of *Salmonella typhimurium* FliI, a flagellar protein related to

the catalytic subunit of the F_0F_1 -ATPase and to virulence proteins of mammalian and plant pathogens. *Journal of bacteriology* **175**, 3131–8 (1993).

⁷⁹ Koonin, E. A common set of conserved motifs in a vast variety of putative nucleic acid-dependent ATPases including MCM proteins involved in the initiation of eukaryotic DNA replication. *Nucleic acids research* (1993).

⁸⁰ Fan, F. & Macnab, R. M. Enzymatic characterization of FliI. An ATPase involved in flagellar assembly in *Salmonella typhimurium*. *The Journal of biological chemistry* **271**, 31981–8 (1996).

⁸¹ Imada, K., Minamino, T., Tahara, A. & Namba, K. Structural similarity between the flagellar type III ATPase FliI and F_1 -ATPase subunits. *Proceedings of the National Academy of Sciences of the United States of America* **104**, 485–90 (2007).

⁸² Abrahams, J. P., Leslie, A. G., Lutter, R. & Walker, J. E. Structure at 2.8 Å resolution of F_1 -ATPase from bovine heart mitochondria. *Nature* **370**, 621–8 (1994).

⁸³ Miwa, K. & Yoshida, M. The alpha 3 beta 3 Complex, the Catalytic Core of F_1 -ATPase. *Proceedings of the National Academy of Sciences* **86**, 6484–6487 (1989).

⁸⁴ Claret, L., Calder, S. R., Higgins, M. & Hughes, C. Oligomerization and activation of the FliI ATPase central to bacterial flagellum assembly. *Molecular microbiology* **48**, 1349–55 (2003).

⁸⁵ Chen, S. *et al.* Structural diversity of bacterial flagellar motors. *The EMBO journal* **30**, 2972–81 (2011).

⁸⁶ Kazetani, K.-I., Minamino, T., Miyata, T., Kato, T. & Namba, K. ATP-induced FliI hexamerization facilitates bacterial flagellar protein export. *Biochemical and biophysical research communications* **388**, 323–7 (2009).

⁸⁷ Minamino, T. *et al.* Oligomerization of the bacterial flagellar ATPase FliI is controlled by its extreme N-terminal region. *Journal of molecular biology* **360**, 510–9 (2006).

⁸⁸ Minamino, T. & MacNab, R. M. FliH, a soluble component of the type III flagellar export apparatus of *Salmonella*, forms a complex with FliI and inhibits its ATPase activity. *Molecular microbiology* **37**, 1494–503 (2000).

⁸⁹ González-Pedrajo, B., Fraser, G. M., Minamino, T. & Macnab, R. M. Molecular dissection of *Salmonella* FliH, a regulator of the ATPase FliI and the type III flagellar protein export pathway. *Molecular microbiology* **45**, 967–82 (2002).

⁹⁰ Lane, M. C., O'Toole, P. W. & Moore, S. A. Molecular basis of the interaction between the flagellar export proteins FliI and FliH from *Helicobacter pylori*. *The Journal of biological chemistry* **281**, 508–17 (2006).

⁹¹ Mark J. P., Bailey C. M. & Beatson S. A. Evolutionary links between FliH/YscL like proteins from bacterial type III secretion systems and second-stalk components of the F_0F_1 and vacuolar ATPases. *Protein Science* **15**, 935–940 (2006)

⁹² Minamino, T., Chu, R., Yamaguchi, S. & Macnab, R. M. Role of FliJ in flagellar protein export in *Salmonella*. *Journal of bacteriology* **182**, 4207–15 (2000).

-
- ⁹³ Fraser, G. M., González-Pedrajo, B., Tame, J. R. & Macnab, R. M. Interactions of FliJ with the Salmonella type III flagellar export apparatus. *Journal of bacteriology* **185**, 5546–54 (2003).
- ⁹⁴ Ibuki, T. *et al.* Common architecture of the flagellar type III protein export apparatus and F- and V-type ATPases. *Nature structural and molecular biology* **18**, 277–82 (2011).
- ⁹⁵ Evans, L. D., Stafford, G. P., Ahmed, S., Fraser, G. M. & Hughes, C. An escort mechanism for cycling of export chaperones during flagellum assembly. *Proceedings of the National Academy of Sciences of the United States of America* **103**, 17474–9 (2006).
- ⁹⁶ Minamino, T., Morimoto, Y. V., Hara, N. & Namba, K. An energy transduction mechanism used in bacterial flagellar type III protein export. *Nature communications* **2**, 475 (2011).
- ⁹⁷ Minamino, T., González-Pedrajo, B., Kihara, M., Namba, K. & Macnab, R. M. The ATPase FliI can interact with the type III flagellar protein export apparatus in the absence of its regulator, FliH. *Journal of bacteriology* **185**, 3983–8 (2003).
- ⁹⁸ Hara, N., Morimoto, Y. V., Kawamoto, A., Namba, K. & Minamino, T. Interaction of the extreme N-terminal region of FliH with FliA is required for efficient bacterial flagellar protein export. *Journal of bacteriology* **194**, 5353–60 (2012).
- ⁹⁹ Hara, N., Morimoto, Y. V., Kawamoto, A., Namba, K. & Minamino, T. Interaction of the extreme N-terminal region of FliH with FliA is required for efficient bacterial flagellar protein export. *Journal of bacteriology* **194**, 5353–60 (2012).
- ¹⁰⁰ Minamino, T. *et al.* Roles of the extreme N-terminal region of FliH for efficient localization of the FliH-FliI complex to the bacterial flagellar type III export apparatus. *Molecular microbiology* **74**, 1471–83 (2009).
- ¹⁰¹ Kubori, T., Shimamoto, N., Yamaguchi, S., Namba, K. & Aizawa, S. Morphological pathway of flagellar assembly in Salmonella typhimurium. *Journal of Molecular Biology* **226**, 433–446 (1992).
- ¹⁰² González-Pedrajo, B., Minamino, T., Kihara, M. & Namba, K. Interactions between C ring proteins and export apparatus components: a possible mechanism for facilitating type III protein export. *Molecular microbiology* **60**, 984–98 (2006).
- ¹⁰³ Paul, K., Harmon, J. G. & Blair, D. F. Mutational analysis of the flagellar rotor protein FliN: identification of surfaces important for flagellar assembly and switching. *Journal of bacteriology* **188**, 5240–8 (2006).
- ¹⁰⁴ McMurry, J. L., Murphy, J. W. & González-Pedrajo, B. The FliN-FliH interaction mediates localization of flagellar export ATPase FliI to the C ring complex. *Biochemistry* **45**, 11790–8 (2006).
- ¹⁰⁵ Minamino, T. *et al.* Roles of the extreme N-terminal region of FliH for efficient localization of the FliH-FliI complex to the bacterial flagellar type III export apparatus. *Molecular microbiology* **74**, 1471–83 (2009).

-
- ¹⁰⁶ Bennett, J. C. & Hughes, C. From flagellum assembly to virulence: the extended family of type III export chaperones. *Trends in microbiology* **8**, 202–4 (2000).
- ¹⁰⁷ Parsot, C., Hamiaux, C. & Page, A.L.L. The various and varying roles of specific chaperones in type III secretion systems. *Current opinion in microbiology* **6**, 7–14 (2003).
- ¹⁰⁸ Feldman, M. F. & Cornelis, G. R. The multitasking type III chaperones: all you can do with 15 kDa. *FEMS microbiology letters* **219**, 151–8 (2003).
- ¹⁰⁹ Fraser, G. M., Bennett, J. C. & Hughes, C. Substrate-specific binding of hook-associated proteins by FlgN and FliT, putative chaperones for flagellum assembly. *Molecular microbiology* **32**, 569–80 (1999).
- ¹¹⁰ Auvray, F., Thomas, J., Fraser, G. M. & Hughes, C. Flagellin polymerisation control by a cytosolic export chaperone. *Journal of molecular biology* **308**, 221–9 (2001).
- ¹¹¹ Bennett, J. C., Thomas, J., Fraser, G. M. & Hughes, C. Substrate complexes and domain organization of the Salmonella flagellar export chaperones FlgN and FliT. *Molecular microbiology* **39**, 781–91 (2001).
- ¹¹² Imada, K., Minamino, T., Kinoshita, M., Furukawa, Y. & Namba, K. Structural insight into the regulatory mechanisms of interactions of the flagellar type III chaperone FliT with its binding partners. *Proceedings of the National Academy of Sciences of the United States of America* **107**, 8812–7 (2010).
- ¹¹³ Evdokimov, A. G. *et al.* Similar modes of polypeptide recognition by export chaperones in flagellar biosynthesis and type III secretion. *Nature structural biology* **10**, 789–93 (2003).
- ¹¹⁴ Luo, Y. *et al.* Structural and biochemical characterization of the type III secretion chaperones CesT and SigE. *Nature structural biology* **8**, 1031–6 (2001).
- ¹¹⁵ Birtalan, S. & Ghosh, P. Structure of the Yersinia type III secretory system chaperone SycE. *Nature structural biology* **8**, 974–8 (2001).
- ¹¹⁶ Büttner, C. R., Sorg, I., Cornelis, G. R., Heinz, D. W. & Niemann, H. H. Structure of the Yersinia enterocolitica type III secretion translocator chaperone SycD. *Journal of molecular biology* **375**, 997–1012 (2008).
- ¹¹⁷ Yip, C. K., Finlay, B. B. & Strynadka, N. C. Structural characterization of a type III secretion system filament protein in complex with its chaperone. *Nature structural and molecular biology* **12**, 75–81 (2005).
- ¹¹⁸ Quinaud, M. *et al.* Structure of the heterotrimeric complex that regulates type III secretion needle formation. *Proceedings of the National Academy of Sciences of the United States of America* **104**, 7803–8 (2007).
- ¹¹⁹ Sun, P., Tropea, J. E., Austin, B. P., Cherry, S. & Waugh, D. S. Structural characterization of the Yersinia pestis type III secretion system needle protein YscF in complex with its heterodimeric chaperone YscE/YscG. *Journal of molecular biology* **377**, 819–30 (2008).
- ¹²⁰ Karlinsey, J. E., Lonner, J., Brown, K. L. & Hughes, K. T. Translation/secretion coupling by type III secretion systems. *Cell* **102**, 487–97 (2000).

-
- ¹²¹ Ohnishi, K., Kutsukake, K., Suzuki, H. & Iino, T. Gene *fliA* encodes an alternative sigma factor specific for flagellar operons in *Salmonella typhimurium*. *Molecular and general genetics* **221**, 139-147 (1990).
- ¹²² Chilcott, G. & Hughes, K. Coupling of Flagellar Gene Expression to Flagellar Assembly in *Salmonella enterica* Serovar Typhimurium and *Escherichia coli*. *Microbiology and Molecular Biology Reviews* (2000).
- ¹²³ Yamamoto, S. & Kutsukake, K. FliT acts as an Anti-FliH/D2C2 Factor in the Transcriptional Control of the Flagellar Regulon in *Salmonella enterica* Serovar Typhimurium. *Journal of Bacteriology* (2006).
- ¹²⁴ Evdokimov, A. G. *et al.* Similar modes of polypeptide recognition by export chaperones in flagellar biosynthesis and type III secretion. *Nature structural biology* **10**, 789–93 (2003).
- ¹²⁵ Ozin, A. J., Claret, L., Auvray, F. & Hughes, C. The FliS chaperone selectively binds the disordered flagellin C-terminal D0 domain central to polymerisation. *FEMS microbiology letters* **219**, 219–24 (2003).
- ¹²⁶ Birtalan, S. C., Phillips, R. M. & Ghosh, P. Three-dimensional secretion signals in chaperone-effector complexes of bacterial pathogens. *Molecular cell* **9**, 971–80 (2002).
- ¹²⁷ Minamino, T., Kinoshita, M., Imada, K. & Namba, K. Interaction between FliI ATPase and a flagellar chaperone FliT during bacterial flagellar protein export. *Molecular microbiology* **83**, 168–78 (2012).
- ¹²⁸ Silva-Herzog, E. & Dreyfus, G. Interaction of FliI, a component of the flagellar export apparatus, with flagellin and hook protein. *Biochimica et biophysica acta* **1431**, 374–83 (1999).
- ¹²⁹ Thomas, J., Stafford, G. P. & Hughes, C. Docking of cytosolic chaperone-substrate complexes at the membrane ATPase during flagellar type III protein export. *Proceedings of the National Academy of Sciences of the United States of America* **101**, 3945–50 (2004).
- ¹³⁰ Akeda, Y. & Galán, J. E. Chaperone release and unfolding of substrates in type III secretion. *Nature* **437**, 911–5 (2005).
- ¹³¹ Minamino, T. *et al.* Interaction of a bacterial flagellar chaperone FlgN with FliH is required for efficient export of its cognate substrates. *Molecular microbiology* **83**, 775–88 (2012).
- ¹³² Bange, G., Kümmerer, N. & Engel, C. FliH provides the adaptor for coordinated delivery of late flagella building blocks to the type III secretion system. *Proceedings of the National Academy of Sciences of the United States of America* **107**, 11295-11300 (2010).
- ¹³³ Kinoshita, M., Hara, N., Imada, K., Namba, K. & Minamino, T. Interactions of bacterial flagellar chaperone-substrate complexes with FliH contribute to coordinating assembly of the flagellar filament. *Molecular microbiology* **90**, 1249–61 (2013).
- ¹³⁴ Aldridge, P. & Hughes, K. Regulation of flagellar assembly. *Current Opinion in Microbiology* **5**, 160-165 (2002).

-
- ¹³⁵ Chilcott, G. & Hughes, K. Coupling of Flagellar Gene Expression to Flagellar Assembly in *Salmonella enterica* Serovar Typhimurium and *Escherichia coli*. *Microbiology and Molecular Biology Reviews* (2000).
- ¹³⁶ Kutsukake, K & Iino, T. Role of the FliA-FlgM regulatory system on the transcriptional control of the flagellar regulon and flagellar formation in *Salmonella typhimurium*. (1994)
- ¹³⁷ Macnab, R. Type III flagellar protein export and flagellar assembly. *Biochimica et Biophysica Acta (BBA) - Molecular Cell Research* **1694**, 207-217 (2004).
- ¹³⁸ Hughes, K., Gillen, K., Semon, M. & Karlinsey, J. Sensing structural intermediates in bacterial flagellar assembly by export of a negative regulator. *Science* **262**, 1277-1280 (1993).
- ¹³⁹ Iyoda, S., Kamidoi, T., Hirose, K., Kutsukake, K. & Watanabe, H. A flagellar gene *fliZ* regulates the expression of invasion genes and virulence phenotype in *Salmonella enterica* serovar Typhimurium. *Microbial Pathogenesis* **30**, 8190 (2001).
- ¹⁴⁰ Yamaguchi, S, Oosawa, K & Aizawa, S. Roles of FliK and FlhB in determination of flagellar hook length in *Salmonella typhimurium*. (1994)
- ¹⁴¹ Kutsukake, K., Minamino, T. & Yokoseki, T. Isolation and characterization of FliK-independent flagellation mutants from *Salmonella typhimurium*. *Journal of bacteriology* **176**, 7625–9 (1994).
- ¹⁴² Williams, A.W., Yamaguchi, S. & Togashi, F. Mutations in *fliK* and *flhB* affecting flagellar hook and filament assembly in *Salmonella typhimurium*. (1996).
- ¹⁴³ Shibata, S. *et al.* FliK regulates flagellar hook length as an internal ruler. *Molecular microbiology* **64**, 1404–15 (2007).
- ¹⁴⁴ Erhardt, M, Singer, HM, Wee, DH & Keener, JP. An infrequent molecular ruler controls flagellar hook length in *Salmonella enterica*. (2011).
- ¹⁴⁵ Moriya, N., Minamino, T., Hughes, K. T., Macnab, R. M. & Namba, K. The type III flagellar export specificity switch is dependent on FliK ruler and a molecular clock. *Journal of molecular biology* **359**, 466–77 (2006).
- ¹⁴⁶ Hirano, T., Shibata, S., Ohnishi, K., Tani, T. & Aizawa, S.I. N-terminal signal region of FliK is dispensable for length control of the flagellar hook. *Molecular microbiology* **56**, 346–60 (2005).
- ¹⁴⁷ Minamino, T., Ferris, H. U., Moriya, N., Kihara, M. & Namba, K. Two parts of the T3S4 domain of the hook-length control protein FliK are essential for the substrate specificity switching of the flagellar type III export apparatus. *Journal of molecular biology* **362**, 1148–58 (2006).
- ¹⁴⁸ Hirano, T., Mizuno, S., Aizawa, S.I. & Hughes, K. T. Mutations in *flk*, *flgG*, *flhA*, and *flhE* that affect the flagellar type III secretion specificity switch in *Salmonella enterica*. *Journal of bacteriology* **191**, 3938–49 (2009).
- ¹⁴⁹ Paul, K., Erhardt, M., Hirano, T., Blair, D. F. & Hughes, K. T. Energy source of flagellar type III secretion. *Nature* **451**, 489–92 (2008).
- ¹⁵⁰ Minamino, T. & Namba, K. Distinct roles of the FliI ATPase and proton motive force in bacterial flagellar protein export. *Nature* **451**, 485–8 (2008).

-
- ¹⁵¹ Wickner, W. & Schekman, R. Protein translocation across biological membranes. *Science (New York, N.Y.)* **310**, 1452–6 (2005).
- ¹⁵² Wilharm, G. *et al.* Yersinia enterocolitica type III secretion depends on the proton motive force but not on the flagellar motor components MotA and MotB. *Infection and immunity* **72**, 4004–9 (2004).
- ¹⁵³ Galperin MYu, Dibrov, P. A. & Glagolev, A. N. delta mu H⁺ is required for flagellar growth in Escherichia coli. *FEBS letters* **143**, 319–22 (1982).
- ¹⁵⁴ Minamino, T., Morimoto, Y. V., Hara, N. & Namba, K. An energy transduction mechanism used in bacterial flagellar type III protein export. *Nature communications* **2**, 475 (2011).
- ¹⁵⁵ Ferentz, A. E. & Wagner, G. NMR spectroscopy: a multifaceted approach to macromolecular structure. *Quarterly reviews of biophysics* **33**, 29–65 (2000).
- ¹⁵⁶ Kay, L. E. NMR studies of protein structure and dynamics. *Journal of magnetic resonance (San Diego, Calif. : 1997)* **213**, 477–91 (2011).
- ¹⁵⁷ Yee, A.A. *et al.* NMR and X-ray crystallography, complementary tools in structural proteomics of small proteins. *J Am Chem Soc* **127**, 16512–16517 (2005).
- ¹⁵⁸ Montelione, G.T., Zheng, D., Huang, Y.J., Gunsalus, K.C. & Szyperski, T. Protein NMR spectroscopy in structural genomics. *Nature Structural Biology* **7**, 982–985 (2000).
- ¹⁵⁹ Sattler, M. Introduction to biomolecular NMR spectroscopy. EMBL Heidelberg (2004).
- ¹⁶⁰ Sekhar, A. & Kay, L. E. NMR paves the way for atomic level descriptions of sparsely populated, transiently formed biomolecular conformers. *Proceedings of the National Academy of Sciences of the United States of America* **110**, 12867–74 (2013).
- ¹⁶¹ Dyson, H. J. & Wright, P. E. Unfolded proteins and protein folding studied by NMR. *Chemical reviews* **104**, 3607–22 (2004).
- ¹⁶² Boehr, D. D., Dyson, H. J. & Wright, P. E. An NMR perspective on enzyme dynamics. *Chemical reviews* **106**, 3055–79 (2006).
- ¹⁶³ Takeuchi, K. & Wagner, G. NMR studies of protein interactions. *Current opinion in structural biology* **16**, 109–17 (2006).
- ¹⁶⁴ Cala, O, Guillière, F & Krimm, I. NMR-based analysis of protein–ligand interactions. (2014).
- ¹⁶⁵ Williamson, M. P. Using chemical shift perturbation to characterize ligand binding. *Progress in nuclear magnetic resonance spectroscopy* **73**, 1–16 (2013).
- ¹⁶⁶ Bax, A. Multidimensional nuclear magnetic resonance methods for protein studies. *Curr Opin Struct Biol.* **4**, 738–744 (1994).
- ¹⁶⁷ Gardner, K.H. & Kay, L.E. The use of ²H, ¹³C, ¹⁵N multidimensional NMR to study the structure and dynamics of proteins. *Annu Rev Biophys Biomol Struct.* **27**, 357–406 (1998).
- ¹⁶⁸ Pervushin, K. Impact of transverse relaxation optimized spectroscopy (TROSY) on NMR as a technique in structural biology. *Q Rev Biophys* **33**, 161–197 (2000).

-
- ¹⁶⁹ Ikura, M., Marion, D., Kay, L.E., Shih, H., Krinks, M., Klee, C.B., & Bax, A. Heteronuclear 3D NMR and isotopic labeling of calmodulin. Towards the complete assignment of the ¹H NMR spectrum. *Biochem Pharmacol.* **40**, 153-160 (1990).
- ¹⁷⁰ Fiaux, J., Bertelsen, E. B., Horwich, A. L. & Wüthrich, K. NMR analysis of a 900K GroEL GroES complex. *Nature* **418**, 207–11 (2002).
- ¹⁷¹ Horst, R. *et al.* Direct NMR observation of a substrate protein bound to the chaperonin GroEL. *Proceedings of the National Academy of Sciences of the United States of America* **102**, 12748–53 (2005).
- ¹⁷² Gordon, S. Rule, T.K.H. & Kaptein, R. Fundamentals of Protein NMR Spectroscopy. 1st ed, Vol. 5. 2006, Dordrecht: Springer. 530.
- ¹⁷³ Lin, Y. & Wagner, G. Efficient side-chain and backbone assignment in large proteins: application to tGCN5. *J Biomol NMR* **15**, 227-39 (1999).
- ¹⁷⁴ Wuthrich, K., NMR studies of structure and function of biological macromolecules (Nobel Lecture). *J Biomol NMR* **27**, 13-39 (2003).
- ¹⁷⁵ Andersson, P., Gsell, B., Wipf, B., Senn, H., & Otting, G. HMQC and HSQC experiments with water flip-back optimized for large proteins. *J Biomol NMR* **11**, 279-288 (1998).
- ¹⁷⁶ Ikura, M., Bax, A., Clore, G.M., & Gronenborn, A.M. Detection of nuclear Overhauser effects between degenerate amide proton resonances by heteronuclear three-dimensional NMR spectroscopy. *J Am Chem Soc* **112**, 9020-9022 (1990).
- ¹⁷⁷ Frenkiel, T., Bauer, C., Carr, M.D., Birdsall, B., & Feeney, J. HMQC-NOESY-HMQC, a three-dimensional NMR experiment which allows detection of nuclear Overhauser effects between protons with overlapping signals. *J Magn Reson.* **90**, 420-425 (1990).
- ¹⁷⁸ Cornilescu, G., Delaglio, F. & Bax, A. Protein backbone angle restraints from searching a database for chemical shift and sequence homology. *Journal of biomolecular NMR* **13**, 289–302 (1999).
- ¹⁷⁹ Shen, Y., Delaglio, F., Cornilescu, G. & Bax, A. TALOS+: a hybrid method for predicting protein backbone torsion angles from NMR chemical shifts. *Journal of biomolecular NMR* **44**, 213–23 (2009).
- ¹⁸⁰ Fernandez, C. & Wider, G. TROSY in NMR studies of the structure and function of large biological macromolecules. *Curr Opin Struct Biol.* **13**, 570-580 (2003).
- ¹⁸¹ Foster, M.P., McElroy, C.A. & Amero, C.D. Solution NMR of large molecules and assemblies. *Biochemistry* **46**, 331-340 (2007).
- ¹⁸² Sattler, M., Schleucher, J. & Griesinger, C. Heteronuclear multidimensional NMR experiments for the structure determination of proteins in solution employing pulsed field gradients. *Prog Nuc Magn Reson Spec.* **34**, 93-158 (1999).
- ¹⁸³ Sattler, M. & Fesik, S.W. Use of deuterium labeling in NMR: overcoming a sizeable problem. *Structure* **4**, 1245-1249 (1996).

-
- ¹⁸⁴ Pervushin, K., Riek, R., Wider, G. & Wuthrich, K. Attenuated T2 relaxation by mutual cancellation of dipole–dipole coupling and chemical shift anisotropy indicates an avenue to NMR structures of very large biological macromolecules in solution. *Proc Natl Acad Sci USA* **94**, 12366–12371 (1997).
- ¹⁸⁵ Riek, R., Fiaux, J., Bertelsen, E.B., Horwich, A.L. & Wuthrich, K. Solution NMR techniques for large molecular and supramolecular structures. *J Am Chem Soc.* **124**, 12144–12153 (2002).
- ¹⁸⁶ Tugarinov, V. & Kay, L. E. Methyl groups as probes of structure and dynamics in NMR studies of high-molecular-weight proteins. *Chembiochem: a European journal of chemical biology* **6**, 1567–77 (2005)
- ¹⁸⁷ Goto, N. & Kay, L. New developments in isotope labeling strategies for protein solution NMR spectroscopy. *Current Opinion in Structural Biology* (2000).
- ¹⁸⁸ Rosen, M. K. *et al.* Selective methyl group protonation of perdeuterated proteins. *Journal of molecular biology* **263**, 627–36 (1996).
- ¹⁸⁹ Sprangers, R., Velyvis, A. & Kay, L. E. Solution NMR of supramolecular complexes: providing new insights into function. *Nat Methods* **4**, 697–703 (2007).
- ¹⁹⁰ Gross, J., Gelev, V. & Wagner, G. A sensitive and robust method for obtaining intermolecular NOEs between side chains in large protein complexes. *Journal of biomolecular NMR* **25**, 235–42 (2003).
- ¹⁹¹ Goto, N.K., Gardner, K.H., Mueller G.A., Willis, R.C. & Kay, L.E. A robust and cost-effective method for the production of Val, Leu, Ile (δ 1) methyl-protonated ¹⁵N-, ¹³C-, ²H-labeled proteins. *J Biomol NMR* **13**, 369–374 (1999).
- ¹⁹² Popovych, N., Tzeng, S.-R. R., Tonelli, M., Ebright, R. H. & Kalodimos, C. G. Structural basis for cAMP-mediated allosteric control of the catabolite activator protein. *Proceedings of the National Academy of Sciences of the United States of America* **106**, 6927–32 (2009).
- ¹⁹³ Isaacson, R. L. *et al.* A new labeling method for methyl transverse relaxation-optimized spectroscopy NMR spectra of alanine residues. *Journal of the American Chemical Society* **129**, 15428–9 (2007).
- ¹⁹⁴ Ayala, I., Sounier, R., Usé, N., Gans, P. & Boisbouvier, J. An efficient protocol for the complete incorporation of methyl-protonated alanine in perdeuterated protein. *Journal of biomolecular NMR* **43**, 111–9 (2009).
- ¹⁹⁵ Gelis, I. *et al.* Structural basis for signal-sequence recognition by the translocase motor SecA as determined by NMR. *Cell* **131**, 756–69 (2007).
- ¹⁹⁶ Saio, T., Guan, X., Rossi, P., Economou, A. & Kalodimos, C. G. Structural basis for protein antiaggregation activity of the trigger factor chaperone. *Science (New York, N.Y.)* **344**, 1250494 (2014).
- ¹⁹⁷ Velyvis, A., Ruschak, A. M. & Kay, L. E. An economical method for production of (²H), (¹³CH₃)-threonine for solution NMR studies of large protein complexes: application to the 670 kDa proteasome. *PloS one* **7**, e43725 (2012).
- ¹⁹⁸ Linge, J.P., Habeck, M., Rieping, W. & Nilges, M. ARIA: automated NOE assignment and NMR structure calculation. *Bioinformatics* **19**, 315–316 (2003).
- ¹⁹⁹ Peter Güntert. Automated NMR structure calculation with CYANA. *Methods in molecular biology* (Clifton, N.J.) 2004

-
- ²⁰⁰ Schwieters, C. D., Kuszewski, J. J., Tjandra, N. & Clore, G. M. The Xplor-NIH NMR molecular structure determination package. *Journal of magnetic resonance (San Diego, Calif. : 1997)* **160**, 65–73 (2003).
- ²⁰¹ de Vries, S.J., van Dijk, M. & Bonvin, A.M.J.J. The HADDOCK web server for data-driven bimolecular docking. *Nat Protoc.* **5**, 883-897 (2010).
- ²⁰² Doreleijers, J. F., Sousa da Silva, A. W., Krieger, E., Nabuurs, S. B., Spronk, C., Stevens, T. J., Vranken, W. F., Vriend, G. & Vuister, G. W. CING: an integrated residue-based structure validation program suite. *Journal of Biomolecular NMR* **54**, 267-283 (2012).
- ²⁰³ Davis, I. W., Leaver-Fay, A., Chen, V. B., Block, J. N., Kapral, G. J., Wang, X., Murray, L. W., Arendall, W. B., Snoeyink, J., Richardson, J. S. & Richardson, D. C. MolProbity: all-atom contacts and structure validation for proteins and nucleic acids. *Nucl. Acids Res.* **35**, 375-383 (2007).
- ²⁰⁴ Laskowski, R. A., MacArthur, M. W., Moss, D. S. & Thornton, J. M. PROCHECK: a program to check the stereochemical quality of protein structures. *J. Appl. Cryst.* **26**, 283-291 (1993).
- ²⁰⁵ Berjanskii, M., Liang, Y., Zhou, J., Tang, P., Stothard, P., Zhou, Y., Cruz, J., MacDonell, C., Lin, G., Lu, P. & Wishart, D. S. PROSESS: a protein structure evaluation suite and server. *Nucl. Acids Res.* **38**, 633–40 (2010).
- ²⁰⁶ Huang, Y.J., Powers, R. & Montelione, G. T. Protein NMR recall, precision, and F-measure scores (RPF scores): structure quality assessment measures based on information retrieval statistics. *Journal of Biomolecular NMR* **127**, 1665–1674 (2005).
- ²⁰⁷ Pellecchia, M., Solution nuclear magnetic resonance spectroscopy techniques for probing intermolecular interactions. *Chem Biol* **12**, 961-71 (2005).
- ²⁰⁸ Marintchev, A., Frueh, D. & Wagner, G. NMR methods for studying protein-protein interactions involved in translation initiation. *Methods in enzymology* **430**, 283–331 (2007).
- ²⁰⁹ Nakanishi, T., et al. Determination of the interface of a large protein complex by transferred cross-saturation measurements. *J Mol Biol.* **318**, 245-9 (2002).
- ²¹⁰ Ikura, M., et al. Solution structure of calmodulin and its complex with a myosin light chain kinase fragment. *Cell Calcium.* **13**, 391-400 (1992).
- ²¹¹ Otting, G. & Wuthrich, K. Heteronuclear filters in two-dimensional [1H,1H]-NMR spectroscopy: combined use with isotope labelling for studies of macromolecular conformation and intermolecular interactions. *Q Rev Biophys* **23**, 39-96 (1990).
- ²¹² Clore, G.M. & Iwahara, J. Theory, practice and applications of paramagnetic relaxation enhancement for the characterization of transient low-population states of biological macromolecules and their complexes. *Chem Rev.* **109**, 4108-4139 (2009).
- ²¹³ Zuiderweg, E.R. Mapping protein-protein interactions in solution by NMR spectroscopy. *Biochemistry* **41**, 1-7 (2002).
- ²¹⁴ Williamson M. P. Using chemical shift perturbation to characterise ligand binding. *Progress in Nuclear Magnetic Resonance Spectroscopy* **73**, 1-16 (2013).

-
- ²¹⁵ Perozzo, R., Folkers, G. & Scapozza, L. Thermodynamics of protein-ligand interactions: history, presence, and future aspects. *Journal of receptor and signal transduction research* **24**, 1–52 (2004).
- ²¹⁶ Ladbury, J. E. Calorimetry as a tool for understanding bio-molecular interactions and an aid to drug design. *Biochemical Society transactions* **38**, 888–93 (2010).
- ²¹⁷ Baker, B.M. & Murphy, K.P. Prediction of binding energetics from structure using empirical parameterization. *Meth Enzymol.* **295**, 294–315 (1998).
- ²¹⁸ Fisher, H.F. & Singh N. Calorimetric methods for interpreting protein-ligand interactions. *Meth Enzymol.* **259**, 194–221 (1995).
- ²¹⁹ Jelesarov, I. & Bosshard, H.R. Isothermal titration calorimetry and differential scanning calorimetry as complementary tools to investigate the energetics of bio-molecular recognition. *J Mol Recogn.* **12**, 3–18 (1999).
- ²²⁰ Erinc, S. & Christopher, J. R. Size-exclusion chromatography with multi-angle light scattering for elucidating protein aggregation mechanisms. *Methods in molecular biology*, (Clifton, N.J.) 2012.
- ²²¹ Some, D. & Kenrick, S. Characterization of protein-protein interactions via static and dynamic light scattering. (2012).
- ²²² Some, D. Light-scattering-based analysis of biomolecular interactions. *Biophysical Reviews* **5**, 147–158 (2013).
- ²²³ Geladopoulos, .T P., Sotiroudis, T. G. & Evangelopoulos, A. E., A Malachite Green Calorimetric Assay for Protein Phosphatase Activity. *Analytical Biochemistry* **192**, 112–116 (1991).
- ²²⁴ Chan, K. M., Delfert, D., Junger, K. D. A direct colorimetric assay for Ca²⁺-stimulated ATPase activity. *Anal Biochem.* **157**, 375–80 (1986).
- ²²⁵ Palmgren, M. G. An H⁺-ATPase Assay: Proton Pumping and ATPase Activity Determined Simultaneously in the Same Sample. *Plant Physiol.* **94**, 882–886 (1990).
- ²²⁶ Zegzouti, H., Zdanovskaia, M., Hsiao., K. & Goueli, S. A. ADP-Glo: A Bioluminescent and homogeneous ADP monitoring assay for kinases, Assay and drug development technologies 2009.
- ²²⁷ Rao, S. T. & Rossmann, M. G. Comparison of super-secondary structures in proteins. *Journal of Molecular Biology* **76**, 241–256 (1973)
- ²²⁸ Akeda, Y. & Galán, J. E. Genetic analysis of the Salmonella enterica type III secretion-associated ATPase InvC defines discrete functional domains. *Journal of bacteriology* **186**, 2402–12 (2004)
- ²²⁹ Chen, L. *et al.* Substrate-activated conformational switch on chaperones encodes a targeting signal in type III secretion. *Cell reports* **3**, 709–15 (2013).
- ²³⁰ Pozidis, C. *et al.* Type III protein translocase: HrcN is a peripheral ATPase that is activated by oligomerization. *The Journal of biological chemistry* **278**, 25816–24 (2003).
- ²³¹ Bai, F. *et al.* Assembly dynamics and the roles of Flil ATPase of the bacterial flagellar export apparatus. *Scientific Reports* **4**, (2014).

-
- ²³² M Futai, T Noumi, and M Maeda. ATP Synthase (H⁺-ATPase): Results by Combined Biochemical and Molecular Biological Approaches. *Annual Review of Biochemistry* **58**, 111-136 (1989)
- ²³³ Nadanaciva, S., Weber, J., Wilke-Mounts, S. & Senior, A. E. Importance of F1-ATPase residue alpha-Arg-376 for catalytic transition state stabilization. *Biochemistry* **38**, 15493–9 (1999).
- ²³⁴ Auvray, F., Ozin, A. J., Claret, L. & Hughes, C. Intrinsic membrane targeting of the flagellar export ATPase FliI: interaction with acidic phospholipids and FliH. *Journal of molecular biology* **318**, 941–50 (2002).
- ²³⁵ Pace, C. N. & Scholtz, J. M. A helix propensity scale based on experimental studies of peptides and proteins. *Biophysical journal* **75**, 422–7 (1998).
- ²³⁶ Gauthier, A. & Finlay, B. Translocated Intimin Receptor and Its Chaperone Interact with ATPase of the Type III Secretion Apparatus of Enteropathogenic *Escherichia coli*. *Journal of Bacteriology* **185**, (2003).
- ²³⁷ Cooper, C. A. *et al.* Structural and biochemical characterization of SrcA, a multi-cargo type III secretion chaperone in *Salmonella* required for pathogenic association with a host. *PLoS pathogens* **6**, e1000751 (2010).
- ²³⁸ Stone, C. B., Johnson, D. L., Bulir, D. C., Gilchrist, J. D. & Mahony, J. B. Characterization of the putative type III secretion ATPase CdsN (Cpn0707) of *Chlamydomonas pneumoniae*. *Journal of bacteriology* **190**, 6580–6588 (2008).
- ²³⁹ Robert, X. & Gouet, P. Deciphering key features in protein structures with the new ENDscript server. *Nucl. Acids Res.* **42**, W320-W324 (2014).
- ²⁴⁰ Tugarinov, V., Kanelis, V. & Kay, L. E. Isotope labeling strategies for the study of high-molecular-weight proteins by solution NMR spectroscopy. *Nature protocols* **1**, 749–54 (2006).
- ²⁴¹ Delaglio, F. *et al.* NMRPipe: a multidimensional spectral processing system based on UNIX pipes. *Journal of bio-molecular NMR* **6**, 277–93 (1995).
- ²⁴² T. D. Goddard & D. G. Kneller. SPARKY 3, University of California, San Francisco.
- ²⁴³ Bruce A Johnson. Using NMRView to visualize and analyze the NMR spectra of macromolecules. *Methods in molecular biology* 313-353, 2004.
- ²⁴⁴ Shen, Y., Delaglio, F., Cornilescu, G. & Bax, A. TALOS+: a hybrid method for predicting protein backbone torsion angles from NMR chemical shifts. *Journal of bio-molecular NMR* **44**, 213–23 (2009).
- ²⁴⁵ Güntert, P. Automated NMR structure calculation with CYANA. *Methods in molecular biology (Clifton, N.J.)* **278**, 353–78 (2004).